

Enhanced Discrimination Techniques for Radar Based On-Metal Identification Tags

by

Jacquelyn A. Vitaz

A dissertation submitted in partial fulfillment
of the requirements for the degree of
Doctor of Philosophy
(Electrical Engineering)
in The University of Michigan
2011

Doctoral Committee:

Professor Kamal Sarabandi, Chair
Professor Mahta Moghaddam
Associate Professor Jerome P. Lynch
Assistant Professor Anthony Grbic
Christopher P. McCarroll, Raytheon Corporation

© Jacquelyn A. Vitaz 2011

All Rights Reserved

To mom and dad; the greatest parents in the universe.

ACKNOWLEDGEMENTS

Most importantly, I would like to thank my committee chair, Professor Kamal Sarabandi, for his kindness, motivation and support throughout this process. He is nothing short of inspiring and I am grateful for the opportunity to pursue my PhD under the supervision of a person that I so deeply respect and admire.

I would also like to thank Dr. Christopher McCarroll of Raytheon Corporation for his invaluable mentorship and guidance throughout this process both at Raytheon and at the University of Michigan. I am deeply grateful for his support along with that of Prof. Mahta Moghaddam, Prof. Anythony Grbic, and Prof. Jerome Lynch for their service on my dissertation committee and Raytheon IDS for their generous financial support of my post-graduate education. I would also like to acknowledge the financial support of Lawrence Livermore National Laboratory for the research presented in this thesis. This work is performed under the auspices of the U.S. Department of Energy funded by Lawrence Livermore National Laboratory under subcontracts B587549, B574750, B574751, B589790, B585877, B581315.

Experimental research can not be completed without the assistance of other colleagues. I would also like to thank Dr. Amelia Buerkle, Dr. Adib Nashashibi and Marc Sallin for their invaluable assistance and support throughout the course of this project. They made the many hours spent in the lab both productive and enjoyable.

I am truly blessed to be surrounded by so many wonderful people and they are all an imperative component to both my success and sanity. The encouragement, assistance, laughter, lunches and friendship of my colleagues at the University of Michigan

Radiation Laboratory has made these years enjoyable. Most notably, Mariko Burgin, Dr. Lin Van Nieuwstadt, Dr. Karl Brakora, Gurkan Gok, Luis Gomez, Dr. Leland Pierce, Karla Johnson, Mehrnoosh Vahidpour, Xueyang (Jessie) Duan, Fikadu Dagefu, Scott Rudolph, Amit Patel, Meysam Moallem, Mohammadreza Imani, Erin Thomas, Marc Shmerling, Etai Weininger, Carsten Barth, Dr. Wonbin Hong, Dr. Michael Thiel, Dr. Dahan Laio, Hatim Bukhari, Dr. Mauro Ettore, Christine Tannahill, Yuriy Goykhman, Dr. Alireza Tabatabaenejad, Morteza Nick, Dr. Farhad Bayatpur, Adel Elsherbini, Mark Haynes, Dr. Xinen Zhu, Abdulkadir Yucel, Waleed Alomar, Jungsuek Oh, Dr. Chih-Hao Kuo, Young Jun Song, Dr. Juseop Lee, Onur Bakir, Michael Benson and Dr. Shahrzad Naraghi. Additionally, I am forever thankful to be surrounded by a group of friends that I cannot imagine life without including Noah Williams, Alisha Scruggs, Sarah Litra-Haas, Tisha Ottem, Chris Yafrate, Joanna Aven and the entire Ann Arbor yoga community.

Finally, I would like to give the greatest gratitude to my mother and father. Their unending love and support have allowed me to live my life without the fear of failure, and for that I am eternally grateful.

Jackie Vitaz

December 10, 2010

TABLE OF CONTENTS

DEDICATION	ii
ACKNOWLEDGEMENTS	iii
LIST OF FIGURES	viii
LIST OF ABBREVIATIONS	xv
ABSTRACT	xvi
CHAPTER	
I. Introduction	1
1.1 Motivation	1
1.2 Retro-reflector Overview	3
1.3 Introduction to the Van Atta Concept	7
1.4 The Radar Cross-Section of a Retro-Reflector	9
1.5 Previous Work	12
1.6 Dissertation Overview	14
II. Applications	17
2.1 Collision Avoidance Systems	18
2.1.1 Inter-vehicle Communication	18
2.1.2 Autonomous Vehicle Operation	19
2.2 RCS Enhancement	20
2.3 Calibration Targets	21
2.4 RFID	22
2.5 Satellite Communication Systems	24
2.6 Friend or Foe Identification	25
III. Passive High-RCS Retro-reflector Architecture	26

3.1	Introduction	27
3.2	GCPW Feed Line Design	28
3.3	GCPW Linear Series-Feed Array	34
3.3.1	Linear Series-Feed Array Introduction	34
3.3.2	GCPW Patch Antenna Introduction	36
3.3.3	GCPW Linear Series Array Design	37
3.4	Passive Retro-Reflective Array Design	45
3.5	Passive Retro-Reflective Array Measurements	48
3.6	Conclusions	49
IV. Active High-RCS Retro-reflector Architecture		52
4.1	Introduction	52
4.2	Introduction to RCS Modulation	53
4.3	Design and Implementation of Active Modulation	54
4.4	Active Retro-Reflective Array Measurements	55
4.5	Active Retro-reflective Array Performance in a High Clutter Environment	57
4.6	Active Tag and Radar System Measurements	59
4.7	Pulse-to-Pulse Subtraction for Enhanced Target Distinction .	61
4.8	Conclusions	63
V. Techniques for Vertical Plane Beam Broadening		66
5.1	Introduction	66
5.2	Alternating-Feed Retro-reflective Array	68
5.2.1	Alternating-Feed Retro-reflective Array Introduction	68
5.2.2	Alternating-Feed Retro-reflective Array Simulation .	70
5.2.3	GCPW Linear Series Array Design and Measurements	73
5.2.4	Alternating-Feed Retro-reflective Array Design and Measurements	74
5.3	Closed-Loop Feed Retro-reflective Array	78
5.3.1	Closed-Loop Feed Retro-reflective Array Introduction	78
5.3.2	Dual-Fed GCPW Linear Series Array Design and Mea- surements	79
5.3.3	Closed-Loop Feed Retro-reflective Array Measurements	79
5.4	Conclusions	82
VI. Cross-polarized Retro-reflector Architecture		84
6.1	Introduction	85
6.2	Polarization Synthesis for Enhanced Target Detection	87
6.3	Passive Cross-Polarized Retro-reflective Array	92
6.3.1	Design Overview	92

6.3.2	Passive Cross-polarized Retro-reflective Array Design and Simulation	94
6.3.3	Passive Cross-polarized Retro-reflective Array Measurements	99
6.3.4	Passive Cross-polarized Retro-reflective Array Performance in High-Clutter Environment	100
6.4	Active Cross-polarized Retro-reflective Array	102
6.4.1	Modulation Overview	102
6.4.2	Active Cross-polarized Retro-reflector Design and Measurements	104
6.4.3	Active Tag and Radar System Measurements	106
6.4.4	Background Subtraction for Enhanced Target Distinction	110
6.5	Conclusions	113
VII. Conclusions and Future Work		114
7.1	Conclusions	114
7.2	Future Work	116
7.2.1	Meta-material Line Integration	116
7.2.2	Decrease Power Consumption	119
7.2.3	Alternate Retro-reflector Topologies	119
7.2.4	Alternative Substrate Materials	119
7.2.5	Advanced Applications	120
BIBLIOGRAPHY		121

LIST OF FIGURES

Figure

1.1	Diagram of a potential application scenario requiring the standoff identification and tracking of large metallic cylinders.	2
1.2	Common examples of optical retro-reflector structures.	3
1.3	The operation of glass bead and cube corner type optical retro-reflectors.	5
1.4	Sketch illustrating the operation of a dihedral corner reflector. . . .	6
1.5	The heterodyne technique for planar phase conjugation.	7
1.6	Phase relationships of the radiating elements for the Van Atta configuration for transmit and receive.	8
1.7	Interconnection schemes for the one-dimensional and two-dimensional Van Atta retro-reflector.	9
2.1	A hypothetical car-to-car communication scenario illustrating inter-vehicle communication.	18
2.2	Photograph of a driverless vehicle and the winner of the 2005 DARPA grand challenge.	20
2.3	Photograph of small remote controlled vehicle.	21
2.4	Photograph UAV.	22
2.5	Photograph of outer view of retro-directive PARC.	23
2.6	Potential application scenarios for long range RFID technologies. . .	24

2.7	A quasi-passive communication system utilizing a retro-directive array	25
3.1	Illustration of proposed high-RCS passive retro-reflective array.	27
3.2	Photograph of the microstrip implementation of the feed network for operation at 26GHz and its associated insertion loss.	30
3.3	Photograph of the GCPW implementation of the feed network for operation at 26GHz along with an exploded view of the corner geometry.	31
3.4	Measured phase of the fabricated GCPW feed network transmission lines.	32
3.5	Insertion loss of fabricated GCPW feed network transmission lines over the band of interest.	32
3.6	Sketch illustrating phase difference between longest and shortest feed network transmission lines for determination of maximum tolerable length variation.	33
3.7	Layout of GCPW patch antenna.	36
3.8	Layout of microstrip patch antenna for numerical model development.	38
3.9	Simulated input impedance for one-port and two-port GCPW patch antennas.	41
3.10	Photograph of 8X1 GCPW linear series array as designed and fabricated.	41
3.11	Return loss and input impedance for the 8X1 GCPW linear series array as designed and fabricated.	42
3.12	Simulated and measured normalized gain pattern for the 8X1 GCPW linear series array with associated transition.	43
3.13	Geometry of an eight element linear array of microstrip patch antennas used for the numerical gain pattern calculation.	44
3.14	Comparison of HFSS and MATLAB simulated gain patterns for an 8X1 linear series array at 26GHz.	44
3.15	Geometry for the calculation of RCS from a Van Atta Array.	45

3.16	MATLAB simulation of the normalized horizontal plane RCS pattern for 8X8 element passive retro-reflective array compared to the identical array without the feed network.	47
3.17	Photograph of the fabricated passive 8X8 retro-reflective array.	48
3.18	Horizontal plane RCS pattern measurement for the passive high-RCS retro-reflective array compared to that of a normalized identically sized flat plate.	50
4.1	Potential modulation schemes for the active high-RCS retro-reflective array.	53
4.2	Photograph of the PIN diode switch as integrated into a retro-reflective array feed network line and its associated bias circuitry.	54
4.3	Photograph of fabricated 8X8 active retro-reflective array.	55
4.4	RCS pattern of the active retro-reflective array with switches and battery pack.	56
4.5	Circuit diagram of the bias network implemented for stand alone operation of the active high-RCS retro-reflective array tag.	57
4.6	Photograph of the driver circuit board layout of Figure 4.5 as fabricated for portable operation.	58
4.7	Photograph of the high clutter measurement setup for the active retro-reflective tag.	58
4.8	Monostatic return signal of the active retro-reflective tag in the high clutter environment pictured in Figure 4.7. The on and off performance is compared.	59
4.9	Photograph of the 26-GHz Ultra-Wideband Rangefinder Radar.	60
4.10	Relevant parameters for McEwan 26GHz Rangefinder.	60
4.11	Dielectric lens and radar system used for the system validation measurements.	61
4.12	Photograph of the complete system test set-up.	62
4.13	The video output signal collected by the radar comparing the on and off states of the active retro-reflective tag.	62

4.14	Photograph of two active retro-reflective arrays in associated cases.	63
4.15	A detailed rear view of active retro-reflective array in associated case.	64
4.16	Performance of active retro-reflective tag before and after pulse-to-pulse subtraction.	65
5.1	Comparison of the vertical and horizontal plane RCS patterns of the passive retro-reflective array configuration presented in Chapter III.	67
5.2	Comparison of standard and alternating-feed interconnection schemes for linear series-feed radiating elements.	69
5.3	Comparison of vertical plane beams produced by the standard and alternating feed interconnection schemes for linear series-feed radiating elements.	69
5.4	Numerically simulated gain pattern for both upward and downward feed orientations of linear series arrays compared with the full wave simulation for an upward oriented linear series array.	71
5.5	Geometry for the numerical RCS calculation for an alternating-feed retro-reflective array.	72
5.6	MATLAB simulation comparing the horizontal plane RCS for 6X8 element alternating-feed retro-reflective array to that of a 9cm X 8cm flat plate.	72
5.7	MATLAB simulation comparing values for the vertical plane squint of the linear series array elements and their effect on the alternating-feed retro-reflective array performance.	73
5.8	Photograph of a fabricated 6X1 linear array element for the alternating-feed retro-reflective array.	74
5.9	Reflection coefficient and gain measurements for the 6X1 linear series array pictured in Figure 5.8.	75
5.10	Photograph of a fabricated 6X8 alternating-feed retro-reflective array.	76
5.11	Vertical plane RCS pattern measurement comparing the standard and alternating-feed passive retro-reflective array.	77

5.12	Horizontal plane RCS pattern measurement comparing standard and alternating-feed retro-reflective array.	77
5.13	Comparison of alternating and closed-loop feed network topologies for linear series-fed radiating elements.	78
5.14	Photograph of the dual-feed linear series array element for the closed-loop feed retro-reflective array.	80
5.15	Gain pattern measurement of the dual-feed linear series array pictured in Figure 5.14.	80
5.16	Photograph of the fabricated closed-loop feed retro-reflective array.	81
5.17	Normalized vertical plane RCS pattern measurement of the closed-loop feed retro-reflective array shown in Figure 5.16 compared to the standard and alternating feed configurations.	82
5.18	Normalized horizontal plane RCS pattern measurement of the closed-loop feed retro-reflective array shown in Figure 5.16 compared to the standard and alternating feed configurations.	83
6.1	Polarization synthesis for naturally occurring targets.	88
6.2	Polarization synthesis for proposed passive cross-polarized retro-reflective array.	89
6.3	Polarization synthesis for proposed cross-polarized active retro-reflective array.	90
6.4	Coordinate system denoting initial (unprimed) and rotated (primed) orientation of the retro-reflective array tag.	91
6.5	Dual-polarized radiating elements are integrated into the traditional Van Atta architecture of Figure 1.6 to yield a cross-polarized retro-reflective array.	93
6.6	Appropriate length feed lines are integrated with dual-polarized linear series array elements to increase the RCS of a cross-polarized retro-reflective array.	94
6.7	Field distributions for a dual-polarized GCPW patch antenna for two orthogonal polarizations.	95

6.8	Simulated transmission and reflection coefficients for a single GCPW dual-polarized patch antenna element	96
6.9	Simulated input impedance, transmission and reflection coefficients for the six element dual-polarized linear series array.	97
6.10	Simulated normalized gain pattern for the 6x1 dual-polarized linear series array.	97
6.11	Simulated monostatic RCS for the 4X6 element cross-polarized retro-reflective array pictured in Figure 6.6 compared to that of an identically sized flat plate.	98
6.12	Photograph of the fabricated six-element dual-polarized linear series array.	99
6.13	Measured S-parameters and gain for the six-element dual polarized linear series array.	100
6.14	Photograph of fabricated cross-polarized retro-reflective array.	101
6.15	Measured monostatic RCS pattern from cross-polarized retro-reflective array shown in Figure 6.14 compared to that of an identically sized flat plate.	101
6.16	Photograph of the passive cross-polarized retro-reflective array in a highly cluttered environment.	103
6.17	Comparison of the co-polarized and cross-polarized return signals from a highly cluttered environment pictured in Figure 6.16.	103
6.18	Sketch illustrating the integration of active components into the dual-polarized retro-reflective array. This will completely eliminate one polarization combination.	104
6.19	Photograph of feed network line with amplifier and requisite DC supply.	105
6.20	Photograph of active cross-polarized retro-reflective array with amplifiers and bias.	106
6.21	RCS pattern of the active cross-polarized retro-reflective array comparing on and off states and the passive cross-polarized retro-reflective array.	107

6.22	Photograph of the active cross-polarized retro-reflective array in a highly cluttered environment.	108
6.23	Cross-polarized return from the active retro-reflective array in both on and off states measured in the highly cluttered laboratory scene shown in Figure 6.22.	109
6.24	Co-polarized return from the active retro-reflective array in both on and off states measured in the highly cluttered laboratory scene shown in Figure 6.22.	110
6.25	Photograph of the radar and active cross-polarized tag in highly cluttered laboratory scene.	111
6.26	Scanned co-polarized and cross-polarized S21 measurements of the active retro-reflective array in a highly cluttered laboratory scene shown in Figure 6.25.	112
6.27	Scanned difference measurement for the co-polarized and cross-polarized arrangement of transmitting and receiving antennas of the active retro-reflective array in a highly cluttered laboratory scene shown in Figure 6.25.	112
7.1	Alternating the standard transmission line with its dual removes the frequency dependence of the propagation delay of the wave along the transmission line.	118
7.2	Alternating the standard transmission line with its dual removes the frequency dependence of the propagation delay of the wave along the transmission line.	118

LIST OF ABBREVIATIONS

- RCS** Radar Cross Section
- GCPW** grounded coplanar waveguide
- PN** pseudo-noise
- RFID** radio-frequency identification
- co-pol** co-polarized
- cross-pol** cross-polarized
- V-pol** vertical polarization
- H-pol** horizontal polarization

ABSTRACT

Enhanced Discrimination Techniques for Radar Based On-Metal Identification Tags

by

Jacquelyn A. Vitaz

Chair: Kamal Sarabandi

The standoff detection and tracking of metallic targets in highly cluttered environments often poses a difficult engineering challenge. This work introduces a new radar-based approach to overcome these limitations. Novel planar retro-reflective array architectures are presented that, in conjunction with a low-cost, pulsed, Ku-band radar used as the reader, will aid in the standoff detection and tracking of large metallic objects in a highly cluttered environment.

In general, traditional methods to improve performance of such retro-reflective structures involve an increase in gain of the array. In this work, a passive Van Atta array is first presented that achieves 0dBsm of RCS from a retro-reflective tag with 10cm X 15cm footprint that makes use of linear series patch antenna arrays implemented in grounded coplanar waveguide (GCPW) architecture. Modulation is introduced into this structure to provide unique identification and, in conjunction with background subtraction, additionally yields a significant increase in the detectability of the tag without requiring additional gain. This work continues by addressing the narrow field of view in elevation plane that is the consequence of RCS enhancement techniques by developing a new retro-reflective feed architecture. A 300% increase in

breadth of the vertical plane beam is demonstrated by feeding the linear series arrays from both terminal ends.

This work concludes with a novel cross-polarized retro-reflective array that utilizes polarization properties to further distinguish itself from surrounding clutter. This array achieves -15dBsm of cross-polarized RCS from an $8.5\text{cm} \times 5\text{cm}$ footprint. Detectability is enhanced considering the reduced clutter backscatter in cross-polarization configuration at the frequency of operation. This tag configuration also allows ease of integration of amplifiers into the feed network without requiring circulator pairs or lossy two-port 3-dB hybrid junctions. A salient feature of this improved tag is an entirely non-reciprocal target whose unique polarization properties further distinguish it from the surrounding, reciprocal clutter. System techniques are demonstrated that exploit this unique response.

These novel planar retro-reflective array structures are designed and implemented at 26GHz, allowing for a small retro-reflective array footprint. Design details and measurement results for the various improved detection topologies are presented and performance enhancements quantified.

CHAPTER I

Introduction

1.1 Motivation

This research topic is inspired by the need for a unique approach for the standoff identification and tracking of metallic objects in highly cluttered environments. A sketch of a potential application scenario is illustrated in Figure 1.1. This depicts a multitude of metallic cylinders housed in a large indoor structure, such as a warehouse. Knowledge of both the unique identity and precise location of each of these cylinders is desired.

Conventional methods of radio-frequency identification (RFID) are not amenable for the application of interest for three primary reasons. First, traditional RFID tags cannot be placed on metallic surfaces as their wire antennas will be shorted out. Second, these systems exhibit a very short range of operation, typically only a few meters, which is unsuitable for the proposed application. Finally, the tag readers used in conventional RFID are not directional, limiting the tracking capabilities of such systems.

This work introduces a new radar-based approach to overcome these shortcomings. For the proposed method, a radar is affixed to the ceiling of the warehouse that will be used to interrogate a tag that is attached to the side of each metallic cylinder. The simultaneous development of these two elements, the radar system and the tag, will

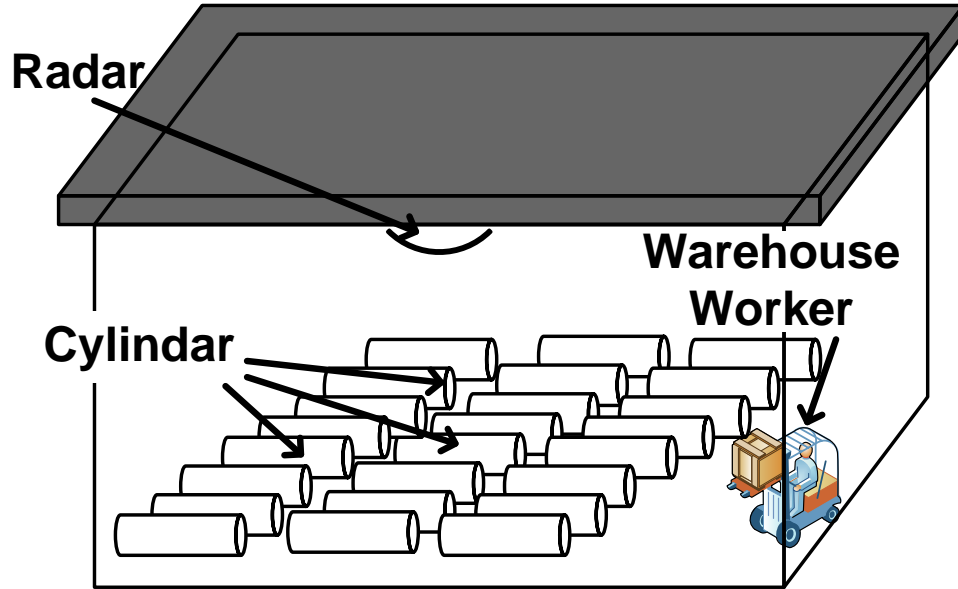


Figure 1.1: Diagram of a potential application scenario requiring the standoff identification and tracking of large metallic cylinders.

result in a novel means for the standoff identification and tracking of metallic objects.

This system is developed at Ku-band (26GHz) allowing for a small size for both the RFID tag and associated reading device, the radar. A consumer pulsed Ku-band radar is modified to act as the tag reader and will be discussed more thoroughly in later sections. This radar operates across the bandwidth of 25.5 to 26.5GHz and is suitable for the application at hand because of its low cost and availability.

A unique retro-reflective tag is proposed and developed to work in conjunction with this radar. This retro-reflective tag requires a both large and broad Radar Cross Section (RCS) response over the range of potential incidence angles. The large RCS is required such that the response of the tag is not buried in the noise of the returned signal and the breadth provides a large field of view that is directed toward the radar. This additionally eases restrictions on the physical placement of the tag on the metallic target of interest. Using the combination of these two elements, the radar and the tag, the unique identity of each cylinder can be obtained along with its precise location. It can also be distinguished from the surrounding clutter as will



Figure 1.2: Common examples of optical retro-reflector structures.

be illustrated in further sections of this thesis, most notably in Chapter IV.

1.2 Retro-reflector Overview

Retro-reflectors are devices or structures which are able to return an incident signal back in the same direction with a large RCS that is independent of angle of arrival for a wide range of incidence angles. These structures accomplish retro-reflectivity without prior knowledge of the source location. Examples of these retro-reflector structures are scattered throughout nature with most occurring in the optical realm. Some commonly observed retro-reflector examples are shown in Figure 1.2.

The glowing eyes of animals, or eyeshine, is a common example of a naturally occurring retro-reflective structure. This phenomena is only observed in animals whose eye structure includes a tapetum lucidum layer [1]. This is a layer of tissue located immediately behind the retina which facilitates night vision. The combination of the eye lens and aqueous humor form a refractive converging surface while the tapetum lucidum forms a spherical concave mirror. When focused on a distant object,

the focal surface of the eye approximately follows the reflective tapetum lucidum. This results in retro-reflection of any light incident on the eye structure.

The eyeshine phenomena is exploited for the development of man made retro-reflectors. The glass bead principle, illustrated in Figure 1.3(a), mimics the cat eye formation by combining spherical glass beads with a reflective backing. These structures, when combined with an adhesive material, such as paint, and applied to a surface in a thin layer, are responsible for the reflective properties of most road signs and license plates.

Alternatively, these retro-reflective surfaces can be formed using the cube corner principle as illustrated in Figure 1.3(b). In this arrangement, tiny cube-like structures are integrated onto the surface of an object. Light incident on the surface is reflected among the faces of the cube and, upon exit from the structure, is directed back toward the source [2]. The range of operation for the aforementioned examples of retro-reflection in the optical realm is limited by the size of the structure itself. That is, for proper operation the typical dimension of the retro-reflectors must be much larger than the wavelength. If the dimensions of the corner reflectors are limited to only few wavelengths, their field of view will be limited, i.e., their RCS pattern will be narrow.

With regard to the microwave realm, retro-reflection is generally achieved by the use of corner reflectors. These are reentrant structures consisting of two or three mutually orthogonal flat plates as illustrated in Figure 1.4. Waves impinging on the first plate are reflected onto the second and, in the case of a two dimensional system, finally exit the structure back in the direction identical to incidence. These corner reflectors work adequately well in low clutter environments, but their large, three-dimensional nature requires significant space, generally in excess of ten wavelengths per side. Consequently, these structures are not easily mounted. Additionally, for the application scenario described in Figure 1.1, the backscatter response of the clutter

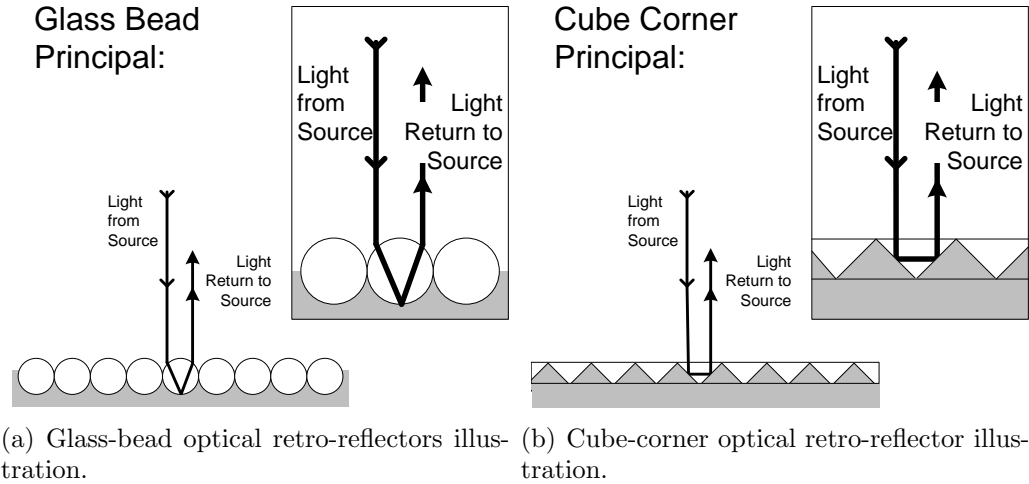


Figure 1.3: The operation of glass bead and cube corner type optical retro-reflectors. These structures are integrated onto clothing or road signs to create an optically retro-reflective surface.

will most certainly rival any reasonably sized corner reflector that can be affixed to the target of interest. As such, the detection and identification of purely passive targets, like the corner reflector, is impossible in situations where range gating alone does not prove sufficient. Instead, alternative modulation schemes require investigation for the identification of targets in these environments.

The proposed application scenario places unique constraints on the design of the tag. It must be planar, in order to be as unobtrusive as possible when affixed to the metallic cylinder. The tag must also be slightly flexible and conformal, such to adhere to the side of the slightly convex surface of the cylinder. Due to the composition of the cylinders themselves, the tag is required to operate on metallic surfaces and additionally provide a large RCS for ease of identification. Signal modulation capabilities are required to provide each tag with a unique identification. Additionally, a long range of operation is necessary due to the large size of the structure (i.e. warehouse) containing the targets of interest.

To achieve retro-reflection from a planar structure one solution is to use phase conjugation of the incident wave in a phased array antenna. This can be accomplished

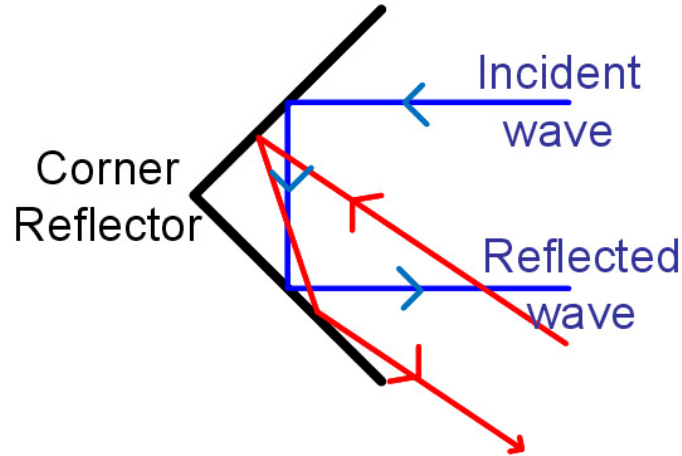


Figure 1.4: Sketch illustrating the operation of a dihedral corner reflector.

by a variety of methods. Using a brute force technique, the phase at each element of an antenna array can be sensed and used to control a programmable phase shifter at each element. This phase shifter then applies the appropriate shift to each element to achieve phase conjugation of the array [3]. This method requires a large number of active components and external power to achieve retro-reflection of the incident signal. Additionally, depending on the complexity of the algorithm involved to achieve beam positioning, there is a potential time delay. Another solution scenario can employ the heterodyne technique to provide phase conjugation and its operation is illustrated in Figure 1.5. In this method, the received signal is mixed with a local oscillator running at approximated twice the RF frequency [3]. The result of this mixing product includes a lower sideband whose frequency is approximately that of the original RF, but with a conjugated phase. This sideband can then be re-radiated and, due to its conjugated phase, the direction of radiation will be toward the source. The drawbacks of this heterodyne technique include a high conversion loss, unwanted additional mixing products and a lower retransmitted power [4]. The most attractive solution for the current application uses a the Van Atta technique which can achieve phase conjugation through the simple interconnection of the radiating elements. This will be described in more detail in the following sections.

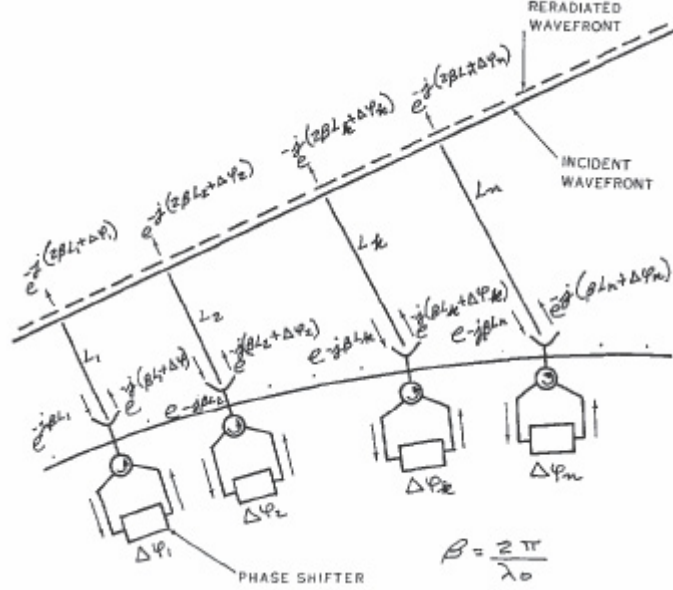


Figure 1.5: The heterodyne technique for planar phase conjugation [3].

1.3 Introduction to the Van Atta Concept

In a Van Atta antenna array configuration, individual linear elements are connected in pairs, depending on their relative distance from the array center as illustrated in Figure 1.6. The lines used to connect each element pair are of equivalent phase length such that the incident energy is reradiated back in the direction of incidence [5]. To understand its operation, consider a plane wave incident on the linear array in Figure 1.6. This incident wave induces currents on each element with a certain phase delay, $\Delta = kd\sin(\theta)$, where k is the wavenumber, θ is the angle of incidence, and d is the intra-element spacing. After the energy travels through the interconnecting lines of identical phase length, ℓ_1 and ℓ_2 , the phase relationship is reversed. Upon reradiation, the energy is directed back in the direction of the source due to the location of the elements with respect to the array center. This configuration operates over a wider range of incidence angles than a typical corner reflector, as it is only limited by the directivity of the individual radiating elements [6]. Additionally, this phase conjugation using the Van Atta technique can be accomplished with no

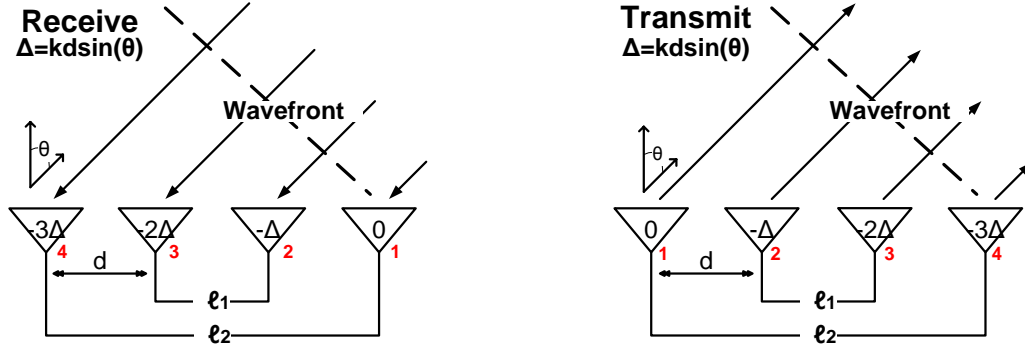


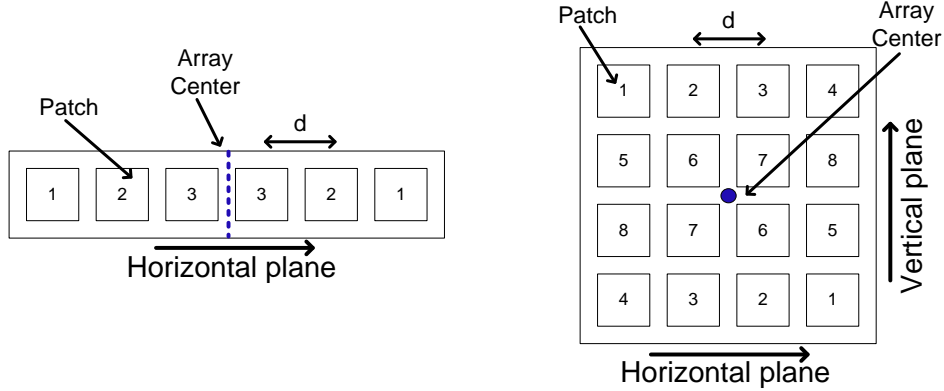
Figure 1.6: Phase relationships of the radiating elements for the Van Atta configuration for transmit and receive. Antenna elements are labeled 1-4 while the phase of each element is identified as multiples of Δ .

external power requirement for a passive array and it can be conformal for ease of manufacture and deployment.

For a one dimensional Van Atta array, the elements are connected as shown in Figure 1.7(a). Elements labeled with identical numbers are connected to one another with appropriate phase delay. The first and last element in the linear array of Figure 1.7(a) are equidistant from the linear array center and hence are connected together, as are the second and the third elements that surround the array center.

Additionally, Van Atta operation can be accomplished in two dimensions by connecting the elements as labeled in Figure 1.7(b) [7]. For this two-dimensional arrangement, elements equidistant from the planar array center are connected to one another with lines of appropriate length to incur identical phase delay within a multiple of a wavelength. This results in retro-reflectivity for both the horizontal and vertical planes of this structure. However, the planar implementation of this two-dimensional topology becomes nearly impossible for even a moderate number of elements due to the required routing of the feed network lines.

While the illustrations in Figure 1.7 only show the connection schemes for even numbers of radiating elements, odd numbers of elements can also be used to obtain retro-reflectivity in the Van Atta arrangement. For an odd number of elements,



(a) One-dimensional Van Atta retro-reflector. (b) Two-dimensional Van Atta retro-reflector.

Figure 1.7: Interconnection schemes for the one-dimensional and two-dimensional Van Atta retro-reflector. Identically numbered elements are connected together with lines of appropriate phase delay.

the center element is connected to a delay line and reflecting short so that phase is maintained on re-transmission when compared to the other element pairs of the retro-reflector.

The precise design of the associated feed network is imperative to the overall operation of the retro-reflective structure. The interconnecting lines are required to provide equivalent phase delay when compared to one another in order to maintain proper phase across the entire array structure and, likewise, achieve retro-reflection. The cyclic nature of phase relationships implies that the lines can vary in length but their differences must be integer multiples of a wavelength. Additionally, the absolute difference in total path lengths is restricted by the bandwidth of operation, as will be further detailed in Chapter VI. This effectively limits the overall size of the array and the routing options for the interconnecting feed lines.

1.4 The Radar Cross-Section of a Retro-Reflector

The RCS of an object is a means of quantifying the detectability of the object to a radar system. When exposed to an electromagnetic wave, an object disperses

the incident energy in all directions. The RCS is defined as a fictitious area that, upon interception of the incident electromagnetic power density, would reradiate the intercepted power isotropically into the surrounding space in such a way that the power density at the receiver is unchanged. This fictitious area would produce the same power density at the receiver as the original target [8]. The RCS is a function of both the direction and polarization of the incident wave as well as the location of the observation point. The mathematical definition for the RCS is as follows [8]:

$$\sigma(\theta, \phi) = \lim_{R \rightarrow \infty} 4\pi R^2 \frac{|E_s|^2}{|E_i|^2}. \quad (1.1)$$

where E_i is the electric field strength of the incident wave impinging on the target and E_s is the electric field strength of the scattered wave at the receiver. The derivation of this quantity assumes the target radiates the intercepted power uniformly in all directions. While this is generally not the physical case, it allows for ease of comparison between different targets noting that all radar parameters, such as power and distance, are factored out. The fictitious area of this point target is such that it would produce the same received power density as the object in question when exposed to identical incoming wave conditions.

Maximizing the RCS for a given footprint allows for greater ease in target distinction and identification. For this reason, maximizing RCS is the primary driving force for the majority of the design decisions for the retro-reflective array variations that follow in the development of this thesis.

In general, the primary figure of merit defining the performance of retro-reflective tags is the amount of energy that is returned to the source. This quantity that is scattered back in the identical direction of incidence is commonly referred to as backscatter. For the calculation of the backscattered RCS from retro-reflective array

itself, Equation 1.1 can also be written as [5]:

$$\sigma = 4\pi R^2 \frac{P_r^s}{P_i} \quad (1.2)$$

where:

σ is the scattering cross-section,

P_r^s is the reflected (scattered) power density at the receiver a distance R from the target

P_i is the power density of the plane wave that is incident upon the target.

The power received by the retro-reflective array is equal to the incident power density, P_i , multiplied by the effective area of the array, A_e . Assuming no dissipative losses in the array for this preliminary calculation, all of the incident power is reradiated, and the power density at the receiver a distance R from the array is:

$$P_r^s = \frac{A_e P_i G}{4\pi R^2} \quad (1.3)$$

where G is the gain of the array. This gain is related to the effective area of the array in the following manner:

$$G = \frac{4\pi A_e}{\lambda^2} \quad (1.4)$$

where λ is the wavelength in free space. Combining Equations 1.2-1.4 results in the scattering cross section, σ , for the Van Atta array:

$$\sigma = \frac{G^2 \lambda^2}{4\pi} \quad (1.5)$$

This RCS is a function of the gain and the wavelength of interest. As the frequency of operation is fixed, an increase in this RCS requires an increase in the gain of the

array structure. This can be achieved by increasing the number of elements such that:

$$G_{total} = \sum_{n=1}^N G_{individual}^n \quad (1.6)$$

Likewise, the RCS of the total array is increased by the square of the total number of elements, N^2 .

For the physical retro-reflective structure, losses will arise and must be accounted for in the overall RCS prediction. The nature of these associated losses will be discussed in greater detail in later sections of this thesis but will be included in the prediction of the backscattered RCS as a generic loss term in the following manner:

$$\sigma(dB) = 10 \log\left(\frac{n^2 G^2(\theta, \phi) \lambda^2}{4\pi}\right)(dB) - L_{losses}(dB) \quad (1.7)$$

where n is the number of elements in the retro-reflective array and $G(\theta, \phi)$ is the gain pattern of each retro-reflector element. L_{losses} accounts for the non-idealities that arise in the physical system such as the losses incurred in the transmission lines connecting the array elements, the antenna elements, and any active components that may be present. From analysis of Equation 1.7, the importance of the gain of the individual radiating elements as the primary role in array performance, is noted.

1.5 Previous Work

Since the inception of the Van Atta architecture for retro-reflective arrays in 1959 [9], the properties of these arrays have become very useful for a variety of applications. The early papers regarding this topic were mainly in the form of thought experiments and non-planar designs at low frequencies. The first implementations of these arrays were in the form of dipoles [10, 5] but it was soon extended to a variety of

radiator types including horn antennas [11, 12]. In all of these cases, these reflective elements are non-planar and interconnections are achieved via coaxial cables, yielding a cumbersome structure.

Planar antennas and printed transmission lines are used to implement a variety of Van Atta retro-reflectors mainly for wireless communications and vehicle tracking applications. In [13], a planar, aperture coupled microstrip Van Atta retro-reflective array at 10GHz is presented, but the feed network employed for the individual radiating elements prohibits operation on metallic surfaces.

Performance enhancements are gained in a variety of retro-reflective architectures by increasing the number of elements in the array. In [14], proximity-coupled dual-ring antennas are combined in sub-arrays to arrive at an 8X16 element retro-directive array at 35GHz. However, the feeding structure of this array makes the integration of active components difficult. In [15], a 2X8 active Van Atta microstrip array operating at 24GHz is discussed. Eight amplifiers are integrated into the microstrip feed lines thus yielding half the elements non-responsive. This result does not yield significant gain and the dominance of the passive flat plate backscatter makes it difficult to distinguish the Van Atta response.

Retro-directivity in two dimensions has also been explored as an alternative to increased gain to achieve enhanced performance by way of angular coverage. In [16, 17], the authors present a four element (2x2) Van Atta array designed to achieve two dimensional retro-directivity. The routing scheme for the interconnection of the radiating elements for these two dimensional arrays becomes problematic for arrays with greater than four total elements because it prohibits the simultaneous achievement of large RCS, modulation capabilities, and bandwidth.

1.6 Dissertation Overview

This dissertation explores a number of different performance enhancement techniques to aid in the detection and tracking of metallic objects in highly cluttered environments. In the sections that follow, design considerations are presented and novel architectures are developed and executed to address them. Each section is explained in further detail.

Chapter II: Applications

A variety of existing and potential applications for planar retro-reflective array structures are discussed including the novel retro-reflective array topologies that enable such technologies. Emphasis is placed on how the work presented in this thesis improves or further enables these existing technologies.

Chapter III: Passive High-RCS Retro-reflector Architecture

This chapter outlines the design approach for the first iteration of the retro-reflective tag in a fully passive configuration. In contrast to the existing RCS enhancement techniques, this novel architecture employs linear series arrays as the radiating elements to increase the gain of the structure while minimizing the complication of the feed network and maintaining bandwidth. This structure achieves operation on metallic surfaces by employing a grounded coplanar waveguide (GCPW) topology in its design. The design of the feed network, radiating elements and linear series arrays are detailed along with the development of models to predict retro-reflector behavior. These models are validated through comparison with a fabricated antenna. This passive high-RCS retro-reflector achieves an RCS of approximately 0dBm over a 60° range in the horizontal plane from a 15cm X 10cm footprint.

Chapter IV: Active High-RCS Retro-reflector Architecture

This chapter details the development of a new method for the detection and tracking of metallic targets at 26GHz that is cost effective and operates over a long range. Modulation is introduced into the passive high-RCS retro-reflective array presented in Chapter III to provide a unique identification. Additionally, this modulation capability is used in conjunction with pulse-to-pulse subtraction to further enhance the detection capabilities of the overall system by removing the response of any time-stationary clutter. The design and implementation of the active circuit are detailed. The operation of the active tag is validated and overall detection system, including background subtraction, confirmed via a mock application scenario constructed in the laboratory setting.

Chapter V: Techniques for Vertical Plane Beam Broadening

This chapter describes the development of novel retro-reflector architectures that utilize beam squint to broaden the elevation plane beam of the high-RCS retro-reflective array presented in Chapter III. The initial alternating-feed architecture attempts to accomplish this broadened beam while simultaneously reducing the size of the retro-reflective array structure. Operation of this structure along with vertical plane beam broadening is verified, but anomalies present in the horizontal-plane pattern are undesirable for the intended application. This leads to the development of a closed-loop feed architecture that, while no longer reducing the size of the structure, does enhance the performance of the overall array by broadening the vertical plane beam without affecting the horizontal plane. The theory of operation for both architectures is established and a model is developed to predict the behavior of the overall array. Measurements are collected for both architectures and compared with those obtained from the Passive High-RCS Van Atta array to quantify performance enhancements and an overall beam broadening of approximately 15° (300%) is observed.

Chapter VI: Cross-Polarized Retro-reflective Array Architecture

This chapter describes the development of a unique cross-polarized array which improves the performance of the retro-reflective array structure by utilizing polarization properties. This allows for maintained or even enhanced detectability from a reduced footprint. The theory of operation is presented along with the design of a novel dual-polarized linear series array and cross-pol feed architecture. This passive cross-polarized retro-reflector obtains approximately -18dB of cross-pol RCS. Additionally, active and non-reciprocal elements are introduced into this passive cross-polarized array. This not only provides a means for the unique identification of each tag, but it also creates a target that does not adhere to reciprocity. This property, in contrast to the passive targets and clutter, allows for even further detectability. This method is verified through implementation using a mock high-clutter scenario set-up in a laboratory setting.

This thesis concludes with a summary of its contributions and future directions of this research topic.

CHAPTER II

Applications

Extensive applications would benefit from enhanced detection techniques for retro-reflective array topologies. This list is not exhaustive but provides a summary of some novel and existing applications for such technologies. The manner in which the current research efforts could contribute to and further these applications is additionally noted.

Potential applications for retro-reflective arrays that will be discussed in this section include:

- Collision Avoidance Systems
- RCS Enhancement
- Calibration Targets
- RFID
- Satellite Communication Systems
- Friend or Foe Identification

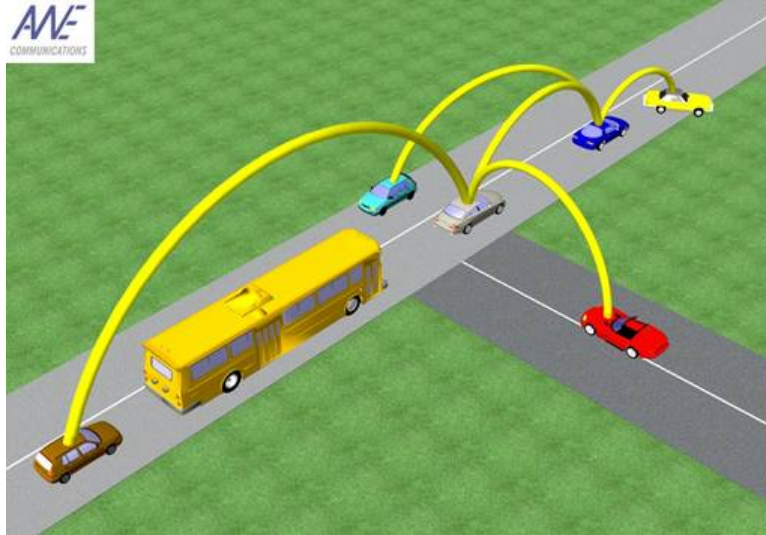


Figure 2.1: A hypothetical car-to-car communication scenario illustrating inter-vehicle communication [18].

2.1 Collision Avoidance Systems

2.1.1 Inter-vehicle Communication

A collision avoidance system consists of a multitude of sensors strategically placed within and on the body of an automobile. These sensors communicate to the vehicle operator and warn of any impending threats or dangers. The pertinent data that these sensors are able to retrieve include the proximity of the car to surrounding vehicles and other assorted obstacles, the reduction in speed required safe curve traversal and the position of the vehicle on the road in a safe and specified lane. An example scenario is depicted in Figure 2.1. This figure illustrates a multitude of cars on a highway along with hypothetical lines of communication between them. One automobile is off the road and blocking traffic and these lines of communication allow for a more advanced warning of this situation.

Traditional means to accomplish this task involve equipping the vehicle with a large number of sensors, such as a radar, to perceive the surrounding environment. The retro-reflective arrays presented in this thesis are well suited to work in con-

junction with these radar systems. Additionally, the modulation capabilities of retro-reflective tags presented in this thesis would allow additional information, such as the intention of the car that it is affixed to, to be relayed to other vehicles on the road. This would facilitate an even greater level of vehicle-to-vehicle communication. Using this technique, driver could become aware of the emergency breaking of the preceding vehicle instead of waiting for the deceleration to be sensed. This advance notice allows for more reaction time for accident avoidance [19].

The narrow beam nature of retro-reflective arrays presented in this thesis would also enhance the current state of the art by contributing to increased security and privacy of the automobile operator. Any communication between nearby vehicles is established and maintained in a monostatic or line of sight manner. This is in contrast to those technologies that involve the use of GPS and require full time surveillance of the vehicle.

2.1.2 Autonomous Vehicle Operation

Similar to the application in Section 2.1.1, autonomous vehicle operation refers to the ability of a car to navigate itself from one point to another either without or with limited assistance from a driver. It is basically an 'autopilot' system for an automobile. This technology has many potential benefits including the elimination of accidents including those resulting from DUIs and associated operator errors.

This class of vehicles range from fully autonomous, where the vehicle is equipped with all necessary sensors required to operate independently, to architectures that include pre-built roadways that would confine the range of operation for such vehicles. The applications and motivations for such technologies are vast and, as such, significant research and development funds have been directed toward achieving a practical autonomous system. A photograph of a fully autonomous driverless car is shown in Figure 2.2. The vehicle is the winner of the 2005 DARPA Grand Challenge;



Figure 2.2: Photograph of a driverless vehicle and the winner of the 2005 DARPA grand challenge [20].

a prize competition for driverless vehicles.

Both the inexpensive and planar nature of the retro-reflective arrays presented in this thesis would facilitate the advancement of autonomous vehicle operation. These arrays could be placed at obstacles, landmarks, and on the roadways. In the passive form, the retro-reflective arrays can increase the detectability of an object to a radar by increasing the RCS. Additionally, utilizing the modulation capabilities of the active arrays, these tags could also relay pertinent information, similar to road signs or mile markers, to the vehicle.

2.2 RCS Enhancement

The enhancement of the RCS of certain targets would prove beneficial in many applications. From a safety standpoint, it could be used to increase the detectability of small ships in the highly cluttered maritime environment. Additionally, increasing the RCS could aide in target tracking, including remotely piloted vehicles (RPVs) pictured in Figure 2.3. This could increase the range of operation and likewise improve performance [21].



Figure 2.3: Photograph of small remote controlled vehicle [22]. The use of RCS enhancement could increase its range of operation.

Additionally, for many applications the anticipated RCS of a target is used as means for its identification. While it is customary to try to reduce the RCS of large targets using a variety of methods, RCS enhancement techniques could alternatively be employed to control the RCS for non-cooperative identification. For such applications, the RCS could be tailored to a specific value to confuse the actual identification of the target. RCS enhancement techniques could additionally aide in the production of decoys allowing small unmanned aerial vehicles, like those in Figure 2.4 to be mistaken for larger targets.

2.3 Calibration Targets

Traditional radar calibration techniques include the measurement of a target with a known response. For most applications, a good calibration target is one whose RCS is large for a large range of incidence angles. The retro-reflective architectures presented in this thesis aide in radar calibration techniques by providing a means of achieving a large and broad RCS.

For low frequency and space-SAR applications, the sizes of traditional calibrators are quite large and become difficult to maneuver and direct [24]. In [12], the author developed a retro-directive PARC for L-band applications pictured in Figure 2.5. The



Figure 2.4: Photograph UAV [23]. The RCS of this UAV could be altered to act as a decoy target.

footprint of this structure is reduced by more than half to $1m^2$ by utilizing a 2-D Van Atta architecture.

The low cost and planar nature of the retro-reflective arrays can be tailored to any frequency and provide a broad and predictable RCS for a multitude of calibration applications. Additionally, the polarization properties of the retro-reflective arrays presented in the later chapter of this thesis could aid in the development of depolarizing calibration targets for fully polarimetric applications.

2.4 RFID

RFID is a technology that uses RF signals to automatically identify objects without required human intervention. It is based on a principle of modulated backscatter that was first published in 1948 [25]. RFID systems generally consist of a "reader" which transmits energy by means of an antenna and a "transponder" or "tag" which is affixed to the object of interest. This tag stores pertinent information regarding

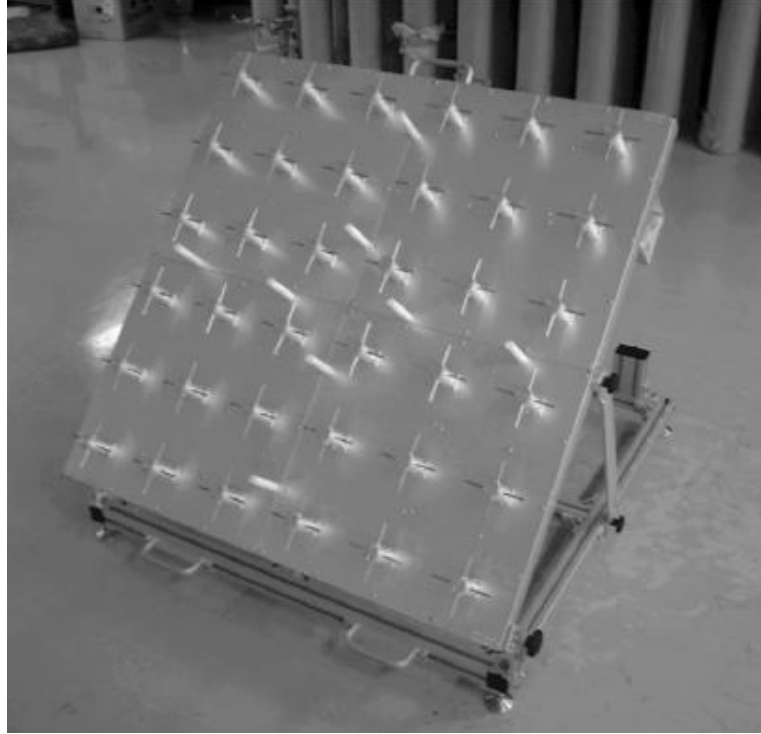


Figure 2.5: Photograph of outer view of retro-directive PARC [12].

its identification. The reader receives the returned signal and decodes it to reveal information relayed from the tag.

For traditional RFID applications, the tag antenna converts the carrier signal into DC which is used to power the array circuitry containing application pertinent information. This circuitry can then send back the information by varying the input impedance of the antenna, effectively modulating the backscattered signal from the antenna which is received and decoded by the reader [26]. As traditional RFID is limited by the power supplied by the interrogator signal, it generally only finds short range applications ranging from a few centimeters to a few meters.

The retro-reflective arrays presented in this thesis are well suited for RFID applications as they are capable of performing the identical task of relaying information to an interrogator. Typical RFID applications, such as freight management and toll management, would additionally benefit from the longer range of operation provided by the retro-reflective arrays presented herein compared with traditional architec-



(a) RFID tags affixed to the windshields of automobiles facilitate toll management. (b) RFID tags affixed to the cargo bays on trucks facilitate freight management.

Figure 2.6: Potential application scenarios for long range RFID technologies.

tures. Examples of these common long range RFID applications are pictured in Figure 2.6. Additionally, the performance of the retro-reflective arrays presented in this thesis are independent of the properties of the structure to which they are affixed. This facilitates the production of a more universal tag architecture for cargo tracking applications.

2.5 Satellite Communication Systems

Retro-directive arrays are well equipped for the relay of information via satellites as they require no on-board RF power. In [11], the authors present a communication system where messages are transmitted to a retro-reflective array that is in orbit as illustrated in Figure 2.7. Alternate earth stations within the field of view of the satellite can then receive these messages by irradiating the satellite antenna. This technology is facilitated by the high reliability of the retro-reflective array in its passive form along with its broad field of view

The retro-reflective array presented in [11] is large in size and the arrays presented in this thesis could additionally benefit such satellite communication systems. The use of planar retro-reflective arrays would reduce the weight of the structure, which is an ever important consideration for any space based system.

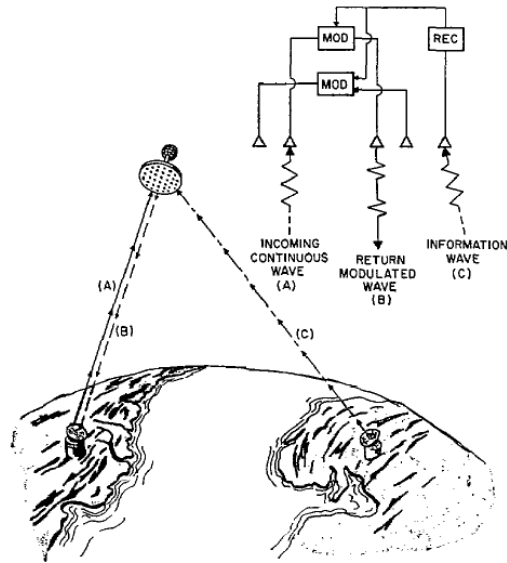


Figure 2.7: A quasi-passive communication system utilizing a retro-directive array [11].

2.6 Friend or Foe Identification

Identification, Friend or Foe (IFF) is a system that provides a means for the identification of friendly targets. A variety of methods exist to accomplish this, but it is generally accomplished using an interrogator, a transponder, and a pre-established code.

The retro-reflective array architectures presented in this thesis are well suited for these applications in both their active and passive forms. The applications for these identification systems range from border patrol to military and beyond.

CHAPTER III

Passive High-RCS Retro-reflector Architecture

The potential application scenario presented in Chapter I requires the development of a retro-reflective array with a high RCS from a small footprint that operates on metallic surfaces. Additionally, this structure must allow for both signal modulation and tracking capabilities. Current technology is not amenable to include these features and novel architectures are likewise explored and developed to provide the desired standoff detection and tracking of objects in highly cluttered environments. To accomplish this, a planar retro-reflective structure in the Van Atta configuration is proposed that incorporates linear series array elements in place of the individual radiating elements pictured in Figure 1.6. To achieve a small footprint, a frequency range of operation from 25.5-26.5 GHz is proposed. A sketch of the proposed high-RCS/small footprint structure is presented in Figure 3.1. The feed network lines in this structure are consistent with the standard Van Atta architecture.

Wider apertures lead to increased directivities in linear arrays. These wider apertures can be obtained either by increasing the number of array elements, the element spacing, or both. The antenna element spacing must remain less than a wavelength at the lowest frequency of operation to avoid grating lobe radiation. While closer element spacings can lead to the design of an array pattern with lower side lobe level, the lower bound on this array spacing is determined by the element size and near-field

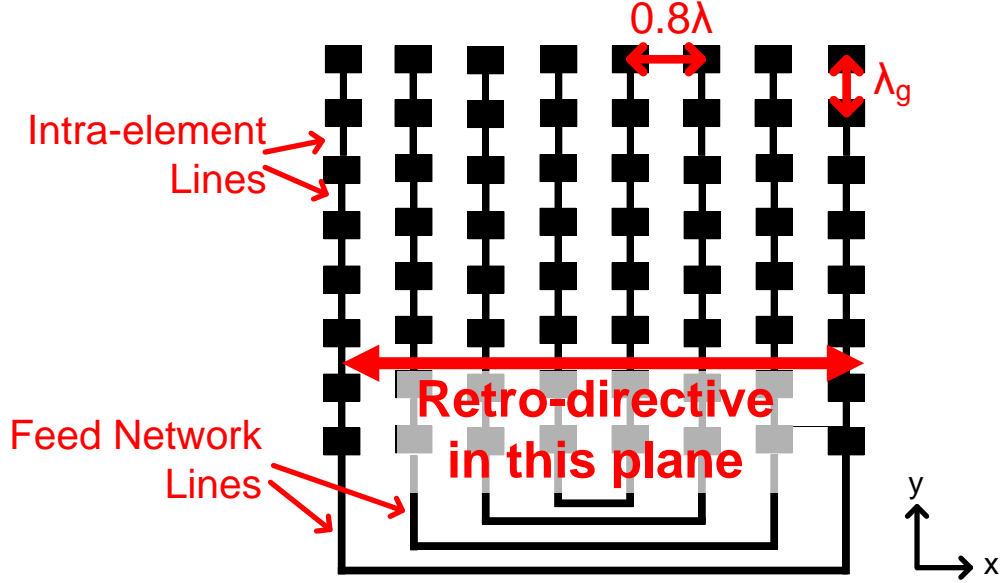


Figure 3.1: Illustration of proposed high-RCS passive retro-reflective array. Individual linear arrays are connected in a Van Atta configuration. The intra-element and intra-array spacings are identified along with the plane of retro-directivity for the structure.

interaction between adjacent elements. For the GCPW patch elements used in this design, 0.8λ element spacing provides acceptable compromise between these sidelobe levels and array aperture size.

3.1 Introduction

The incorporation of linear series-fed patch arrays into the standard Van Atta retro-reflector increases the RCS of the overall structure by a factor of n^2 without resulting in the additional loss and bandwidth limitations that would arise from the standard addition of elements. Using these constituent arrays also reduces the number of active components and feed lines required for the overall array structure and their associated losses. Likewise, a large backscattered RCS is achieved in the x-direction as indicated in Figure 3.1 along with a narrow, directive, beam in the y-direction.

The design of series-fed patch arrays uniquely incorporates a GCPW topology.

The GCPW patch elements, which will be discussed in greater detail in the following sections, provide a unique advantage in the suppression of substrate modes compared to other planar topologies. This allows for significant isolation among adjacent array elements. The unique orientation of the series-fed arrays additionally provides beam squinting in the y-direction. This allows for ease of target identification as the retro-reflective response of the array can be distinguished from the ground plane reflection. This beam squinting feature, which results from the traveling wave associated with the feed geometry, can be further utilized to achieve overall beam broadening, as will be demonstrated in Chapter V.

3.2 GCPW Feed Line Design

The planar nature of this design combined with a desire for operation on metallic surfaces subsequently limits the feasibility of potential feed topologies. To achieve a thin and lightweight array design, a coplanar feed structure located on the same plane as the radiating elements is optimal. For this configuration, the operation of the feed network would not be affected for an array affixed to a metallic surface. This feed structure also allows for the use of a single-layer board design, which additionally minimizes the thickness, weight, and cost of the overall retro-reflective array.

With feed network positioned on the same plane as the radiating elements, it subsequently becomes a prominent feature of the array structure. In consequence, any resistive losses and radiation contributed by the feed network lead to gain and radiation pattern anomalies in the overall array performance. Feeding effects are thereby an important factor in the design of such arrays and require thorough investigation [27].

The main sources of loss for the straight line segments of the the feed network are the result of conductor and dielectric loss [28]. The dielectric loss is a function of the loss tangent and thickness of the substrate material and can be limited by the proper

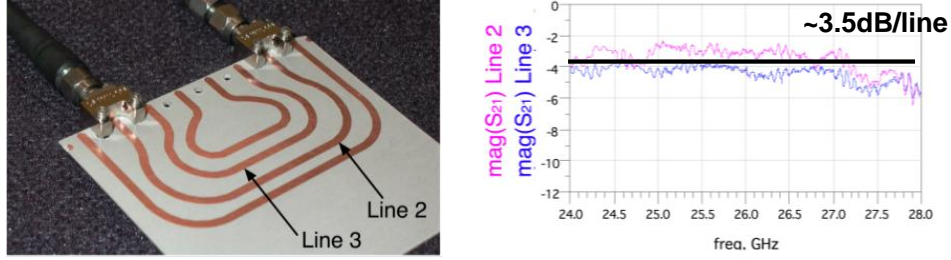
choice of dielectric substrate. Rogers RT/duroid 6002 [29] is utilized as the substrate for this application due to its excellent high frequency performance and mechanical properties. It has a low dielectric loss tangent at 26GHz and has a slightly malleable mechanical structure making it ideal for applications where conformity is required.

The conductor loss is a function of the surface resistivity and impedance of the conductive material [30]. While it is generally not feasible to incorporate materials other than copper for the conductive layer, this loss contribution can be limited by minimizing the overall length and quantity of the feed network lines.

The addition of bends and other associated discontinuities to the feed line geometry results in additional losses contributed by the feed network. These associated losses are in the form of radiation and surface waves. Radiation losses appear as spherical waves that propagate upward from the substrate into free space, while surface waves are cylindrical waves that propagate along the plane of the substrate [31]. Both of these loss modes degrade the overall performance and efficiency of the retro-reflective array.

Initial designs of the corporate feed for the passive Van Atta structure employed a microstrip topology. The feed network using these microstrip lines was carefully laid out, as shown in Figure 3.2(a), to minimize the severity of the bends and discontinuities in the transmission line. S-parameter measurements of this fabricated structure, Figure 3.2(b), reveal significant loss at the frequency of interest despite the careful design and routing. As a result, the microstrip architecture is abandoned for the feed network design and alternative transmission line topologies are explored for the final implementation.

To minimize insertion loss and to allow for maximum energy transfer at this high frequency of operation, GCPW architecture is considered for the next design iteration of the retro-reflector feed structure. GCPW transmission lines consist of a center strip conductor surrounded by two semi-infinite ground plates which support



(a) Photograph of microstrip feed network implementation for operation at 26GHz. (b) Measured insertion loss of the microstrip feed architecture of Figure 3.2(a), as designed and fabricated.

Figure 3.2: Photograph of the microstrip implementation of the feed network for operation at 26GHz and its associated insertion loss.

quasi-TEM propagation. These GCPW lines have the additional benefits of ease of fabrication with both shunt and surface mount devices, reduced radiation loss and reduced cross talk effects between adjacent lines [32]. Figure 3.3 shows a photograph of the fabricated feed network lines and an exploded view of the GCPW corner geometry, identifying the important design parameters. The semi-infinite ground planes are implemented in the structure using a double row of vias to connect this surface to the bottom ground plane of the substrate. This facilitates a stronger ground connection.

In order to achieve the retro-reflectivity discussed in Chapter I, the lines must be of such lengths to provide identical phase delay relative to one another. The bend geometry remains consistent in each line to eliminate this variable from the design process. The straight segments of transmission line are altered to achieve identical phase delay within a multiple of a wavelength along the entire feed network. It should be noted that, at the frequency of operation, a 0.2mm variation in length corresponds to approximately 10° of phase variation. Likewise, small discontinuities, even those on the order of fabrication tolerances, impact the performance of the feed network and, subsequently, the overall retro-reflective array.

The phase response of S11 is collected to verify proper phase characteristics of the feed network. For this measurement, the feed line is terminated with an open circuit and the phase collected over the frequency band of interest. Figure 3.4 presents

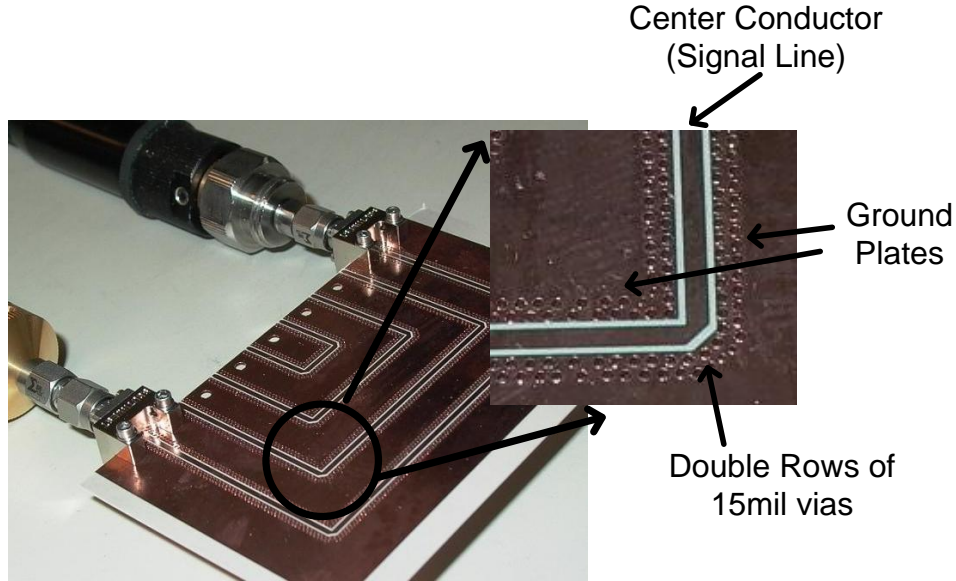


Figure 3.3: Photograph of the GCPW implementation of the feed network for operation at 26GHz along with an exploded view of the corner geometry. The relevant design parameters labeled accordingly.

the measured phase of S_{11} . Identical phase is observed at 26.2GHz among the four transmission lines that comprise the feed network. Additionally, the insertion loss of the GCPW feed network is collected and displayed in Figure 3.5. The loss of this GCPW structure is approximately 1-2.5dB, which is significantly less than a comparable microstrip design ($\sim 3.5\text{dB}/\text{line}$). This is despite the more severe bend geometry of the GCPW structure when compared to the microstrip topology as observed by comparison of Figure 3.3 and Figure 3.2(a).

In addition to this contribution to performance efficiency, the feed lines also play an important role in the overall bandwidth of operation for the retro-reflective array if not designed properly. The difference between the shortest and longest line connecting the series arrays is not to exceed an ultimate value as determined by the intended bandwidth. Figure 3.6 illustrates the phase propagation behavior of two varying lengths of transmission line with respect to frequency. It is observed that increasing the length of transmission line in the feed network also increases the slope of the

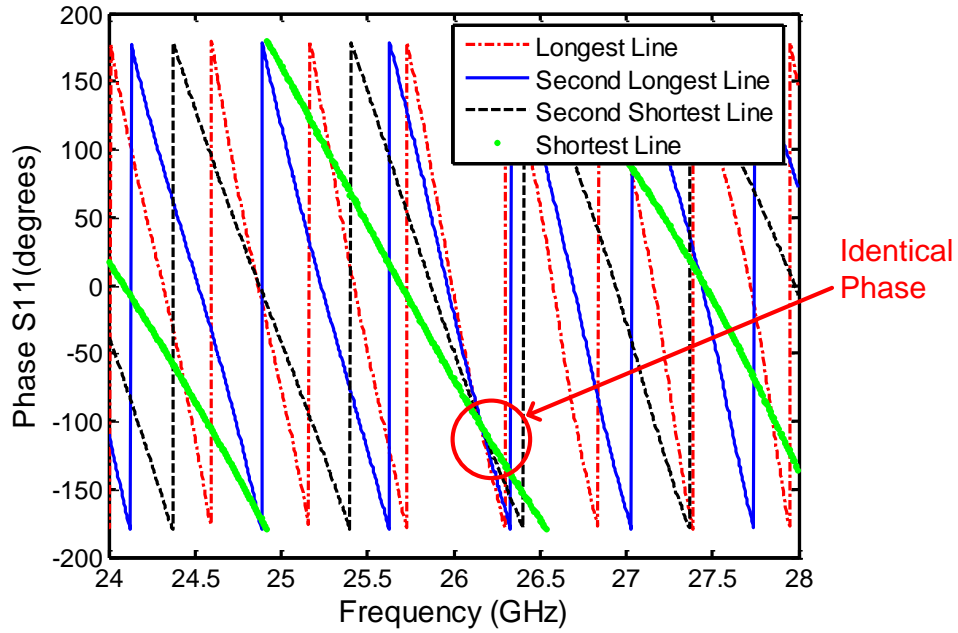


Figure 3.4: Measured phase of the fabricated GCPW feed network transmission lines. Note identical phase at 26.2GHz. Results acquired using one port S11 measurements.

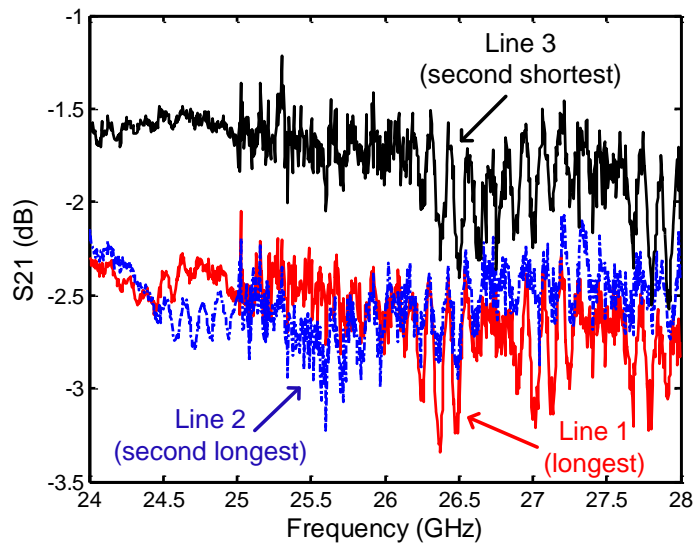


Figure 3.5: Insertion loss of fabricated GCPW feed network transmission lines over the band of interest.

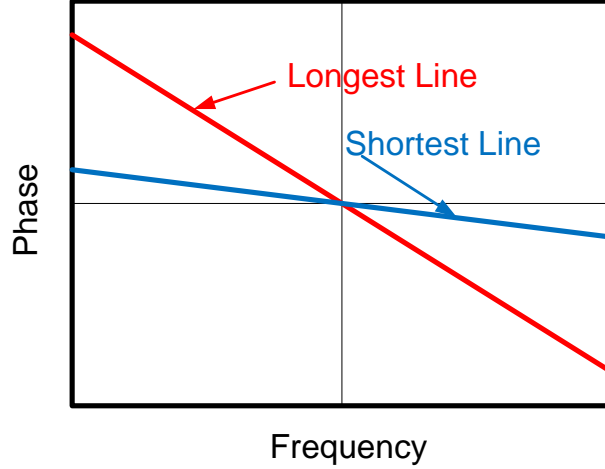


Figure 3.6: Sketch illustrating phase difference between longest and shortest feed network transmission lines for determination of maximum tolerable length variation.

phase response. Moving away from the center frequency, where the phase response of the two transmission lines intersect, the growing error between the shortest (least sloped) and longest (most highly sloped) lines is noted. The frequency range over which an acceptable phase error between these two transmission lines is maintained ultimately determines the operational bandwidth for structures with significant feed networks.

For the current application, the maximum tolerable phase variation is chosen to be 90° . If the phase lengths of the associated feed lines differ by more than this value, the structure is no longer performing as a retro-reflective Van Atta and operation suffers. The maximum tolerable phase variation can then be used to determine the maximum length difference between the longest and shortest feed network lines in the following manner. The signal phase along the longest and shortest transmission lines of the overall feed network can be defined as:

$$\text{Phase of Longest Line} = (k + \Delta k)\ell_l = 2\pi m + \Delta\phi_L = 2\pi m + \frac{\Delta k}{k_o}k_o\ell_l \quad (3.1)$$

$$\text{Phase of Shortest Line} = (k + \Delta k)\ell_s = 2\pi n + \Delta\phi_S = 2\pi n + \frac{\Delta k}{k_o}k_o\ell_s \quad (3.2)$$

where ℓ_l and ℓ_s are the lengths of the longest and shortest transmission lines, respectively, $\Delta\phi_L$ and $\Delta\phi_S$ are the incremental phase delays associated with the longest and shortest transmission lines, k is the wavenumber or frequency, and Δk represents the shift in frequency. The phase difference between the longest and shortest transmission lines with respect to frequency variation is given by:

$$\Delta\phi_N = \Delta\phi_L - \Delta\phi_S = \frac{\Delta k}{k_o}k_o(\ell_l - \ell_s) \leq \frac{\pi}{2} \quad (3.3)$$

For the desired 4% (1GHz) bandwidth at the frequency of interest, the maximum tolerable length difference, ($\Delta\ell$), is:

$$4\% \frac{2\pi}{\lambda} \Delta\ell \leq \frac{\pi}{2} \quad (3.4)$$

$$\Delta\ell \leq \frac{\lambda}{0.04 * 4} = 6.25\lambda \quad (3.5)$$

Hence, the length difference comparing the longest line to that of the shortest line cannot exceed 6.25λ at the frequency of interest for the intended 4% bandwidth. This effectively limits the overall maximum dimension and line routing options for the feed network structure.

3.3 GCPW Linear Series-Feed Array

3.3.1 Linear Series-Feed Array Introduction

Due to the prominence of the element gain in the overall backscattered RCS, as noted in Equation 1.7, the use of high gain array elements is desired. To accomplish

this, the proposed structure incorporates a linear series of elements in place of the individual radiating elements used in the traditional Van Atta architecture. The increased gain contributed by the linear series array increases the RCS of the overall retro-reflective array structure.

The series-fed array configuration offers unique advantages over other antenna array configurations [33]. The feed line lengths are inherently minimized, reducing losses through radiation and dissipation. Using these constituent arrays also uses the minimum number of active components for modulation or amplification, if required. This additionally contributes to RCS enhancement of the overall structure by reducing the number of switches and other associated circuitry required for the active design, and likewise, any additional loss they contribute. This linear series feed arrangement requires significant design considerations at the frequency of interest. While theoretical models for the design of these linear series arrays have been developed, the inherent discontinuities in the structure gives rise to anomalies in the measured patterns.

The series array, from an equivalent circuit perspective, is the combination of parallel resonant circuits, each of which represent a single patch element. As the elements are spaced a wavelength apart at resonance, each individual element theoretically contributes no reactive component and only the parallel combination of input resistances remain. Hence, the impedance observed at the input of the linear series array is the parallel combination of the impedances of the individual elements that constitute the array. In order to achieve a 50Ω input impedance to the 8X1 linear series array, the input impedance of each resonator is set to $Z=400+j0\Omega$ at 26GHz. Likewise, the parallel combination of the eight elements provides the desired 50Ω input impedance.

The effect of these individual resonators separated by wavelength lines can then be studied. The bandwidth of the series feed configuration varies as the inverse of the

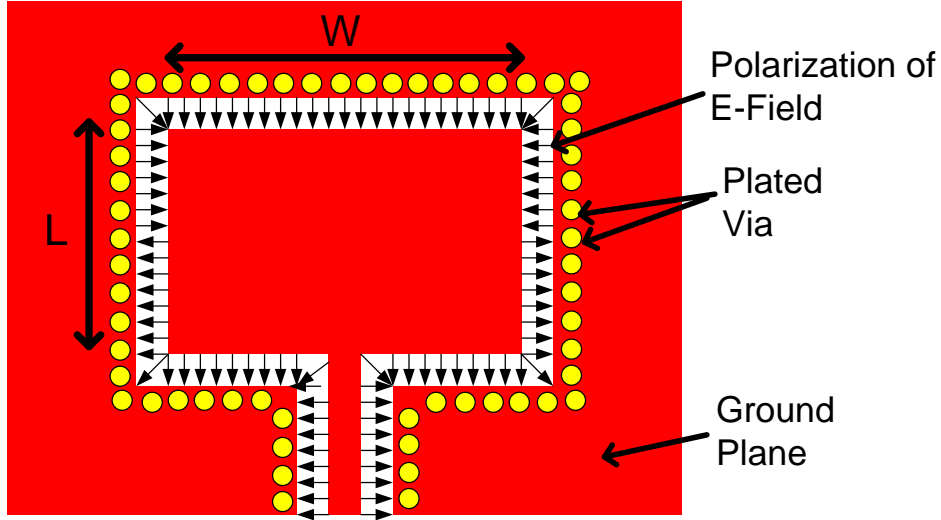


Figure 3.7: Layout of GCPW patch antenna. Relevant design parameters and the direction of E-field are labeled accordingly.

length of the array [27]. Likewise, a severe reduction of the bandwidth of the single resonant element results with the addition of each element. Additionally, matching is highly susceptible to small variations in the lengths of the lines that separate the radiating elements. For example, a 4° change in phase between the radiating elements, corresponding to only $90\mu\text{m}$ of line length, is observed to have impact on the resonant frequency (approximately 100MHz shift).

3.3.2 GCPW Patch Antenna Introduction

The individual patch elements are designed using a coplanar topology for the same reasons as cited in Section 3.2. An individual coplanar patch element consists of a patch antenna closely surrounded by a ground plane and fed with a GCPW line, as depicted in Figure 3.7 [34]. This arrangement reduces radiation into the substrate and cross coupling among adjacent array elements. This additionally allows for the requisite bandwidth to be achieved without resorting to the thicker substrate as would be required if using a microstrip topology. The use of a thinner substrate additionally reduces the overall weight and presence of the array structure.

While this GCPW antenna element is very similar in geometric configuration to a loop slot antenna, it behaves almost entirely like a microstrip patch antenna [34]. In particular, the resonant frequency acts as a function of the patch length (L) rather than the total loop size, as would be the case for the loop slot antenna, and the input impedance is a function of the width (W) of the element.

3.3.3 GCPW Linear Series Array Design

For the development of the linear series array, a single patch is first designed using design principles, modeled numerically in MATLAB, and then verified with full wave electromagnetic field simulation tools (HFSS). The substrate employed for this design is 20mil thick Rogers Corporation RT/duroid 6002.

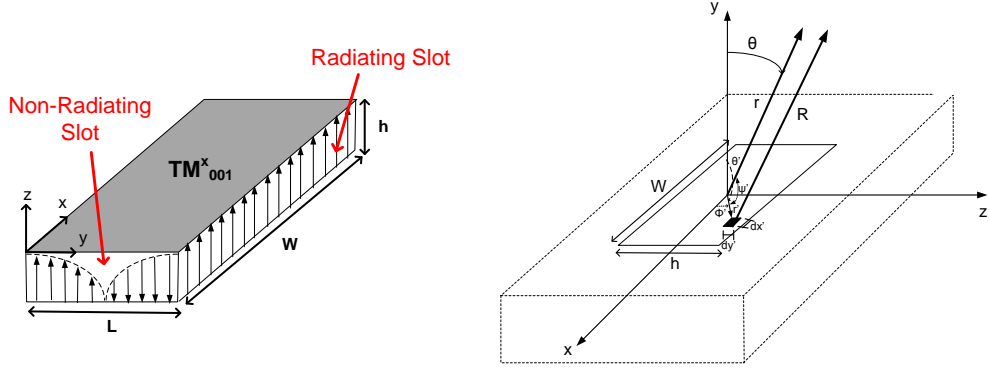
For the development of the numerical simulation, the single element GCPW patch antenna is modeled in an identical manner to that of a microstrip patch antenna, as two radiating slots separated by a distance, L , the length of the patch. This is then confirmed by comparison with an equivalent full wave model. The numerical simulation is ultimately used to predict the overall performance of the entire retro-reflective array structure which is too large for a complete full wave analysis.

For a single element oriented in the x-y plane, as illustrated in Figure 3.8(a), two radiating slots are formed in the x-z plane. One of these radiating slots is expanded in greater detail in Figure 3.8(b). To obtain an overall model for the single element first requires the determination of the field from a single rectangular aperture mounted on an infinite ground plane with a constant field distribution given by:

$$E_a = \hat{a}_z E_o; \quad \frac{-h}{2} \leq z' \leq \frac{h}{2}, \quad \frac{-W}{2} \leq x' \leq \frac{W}{2} \quad (3.6)$$

with E_o defined as a constant E-field amplitude.

Invoking the field equivalence principle, the radiating aperture can be transformed



(a) Layout of microstrip patch antenna operating in lowest order mode. (b) Set-up for the numerical solution of the radiating fields from the slots of the microstrip patch antenna.

Figure 3.8: Layout of microstrip patch antenna for numerical model development [35].

into an equivalent magnetic current source which yields the same fields outside of an imaginary surface, S , enclosing the aperture. Then, using image theory, this radiating aperture can be solved in the far field. The radiating aperture is transformed into an equivalent magnetic current source in an unbounded medium whose value is given by:

$$M_s = -2\hat{n} \times E_a \quad (3.7)$$

The far-field radiation patterns can then be determined using vector potential methods as described in [35]:

$$F = \frac{\epsilon}{4\pi} \iint_S M \frac{e^{-jkR}}{R} ds' \cong \frac{\epsilon e^{-jkr}}{4\pi r} \Lambda \quad (3.8)$$

which is a solution to the inhomogeneous vector wave equation in the far-field where:

$$\Lambda = \iint_S M_s e^{-jk r' \cos \psi} ds' \quad (3.9)$$

While the radial components are not necessarily zero, they are negligible in the far

field computation. Substituting Equation 3.6 and Equation 3.7 into Equation 3.9 results in:

$$\Lambda_\theta = -2 E_o w h \cos \theta \cos \phi \frac{\sin(X)}{X} \frac{\sin(Y)}{Y} \quad (3.10)$$

and

$$\Lambda_\phi = 2 E_o w h \sin \phi \frac{\sin(X)}{X} \frac{\sin(Y)}{Y} \quad (3.11)$$

where

$$X = \frac{k w}{2} \sin \theta \sin \phi \quad (3.12)$$

and

$$Y = \frac{k h}{2} \cos \theta \quad (3.13)$$

The fields then re-radiated from the single aperture can be determined as:

$$E_\theta \cong -j \omega \eta F_\phi = \frac{j k e^{-j k r}}{4 \pi r} \Lambda_\phi \quad (3.14)$$

$$E_\phi \cong +j \omega \eta F_\theta = \frac{j k e^{-j k r}}{4 \pi r} \Lambda_\theta \quad (3.15)$$

To account for the presence of two distinct sources separated by the length of the patch, it is then necessary to multiply this quantity by a factor:

$$A F_y = 2 \cos\left(\frac{k L}{2} \sin \theta \sin \phi\right) \quad (3.16)$$

Combining equations Equation 3.10 - 3.11 with Equation 3.14 - 3.16 yields the total field for each individual radiating patch.

$$E_{\phi}(\theta, \phi) = -\frac{j E_o w h k e^{-jkr}}{\pi r} \cos \theta \cos \phi \frac{\sin(X)}{X} \frac{\sin(Y)}{Y} \cos\left(\frac{kL}{2} \sin \theta \sin \phi\right) \quad (3.17)$$

$$E_{\theta}(\theta, \phi) = \frac{j E_o w h k e^{-jkr}}{\pi r} \sin \phi \frac{\sin(X)}{X} \frac{\sin(Y)}{Y} \cos\left(\frac{kL}{2} \sin \theta \sin \phi\right) \quad (3.18)$$

The equivalent current densities for a single, non-radiating slot is shown in Figure 3.8(a). This slot has the equivalent length, L , and height, h . For these non-radiating slots, the current densities on each wall are identical in magnitude but in opposite direction and, likewise, their associated radiated fields cancel in both the E-plane and H-plane.

For the full wave (HFSS) model, the individual elements are modeled as GCPW patch antennas connected by high impedance GCPW transmission lines, in a manner similar to actual implementation. Perfectly conducting walls are substituted for the vias in this simulation to simplify the required computational complexity. For the full wave implementation of the linear series array, two separate patch antenna designs are required due to varying load conditions. The internal patch elements are modeled as two port (terminal) devices with associated transmission lines, and the final element in the series is modeled as a single port device. The simulated input impedance of the single-port and dual-port coplanar patch antenna elements is shown in Figure 3.9. The real component of the impedance is close to the desired value of 400Ω while the imaginary component is close to 0 at the design frequency for both patch designs.

These individual patch elements are then arranged in an 8X1 linear array configuration. A photograph of the fabricated array is shown in Figure 3.10. A transition from the GCPW line to the array input is implemented to minimize reflections. These reflections are the result of the mismatch between the high impedance lines that are

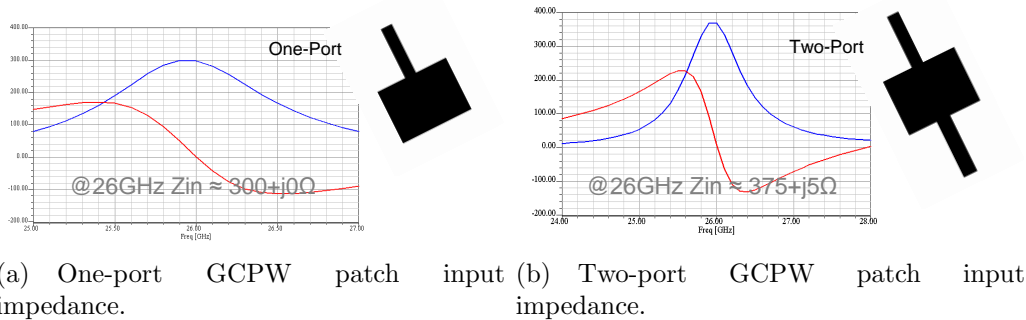


Figure 3.9: Simulated input impedance for one-port and two-port GCPW patch antennas.

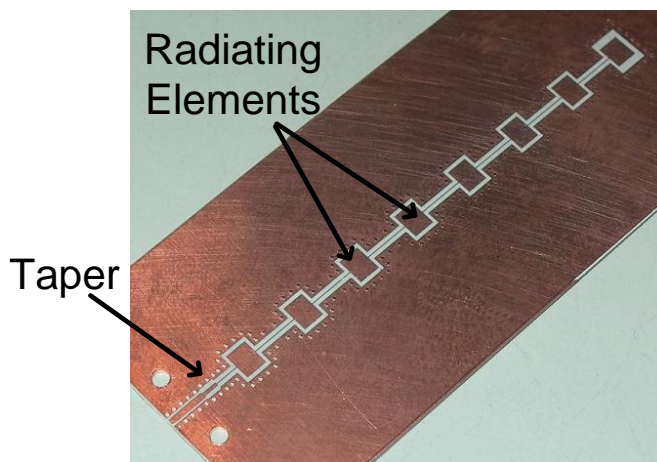
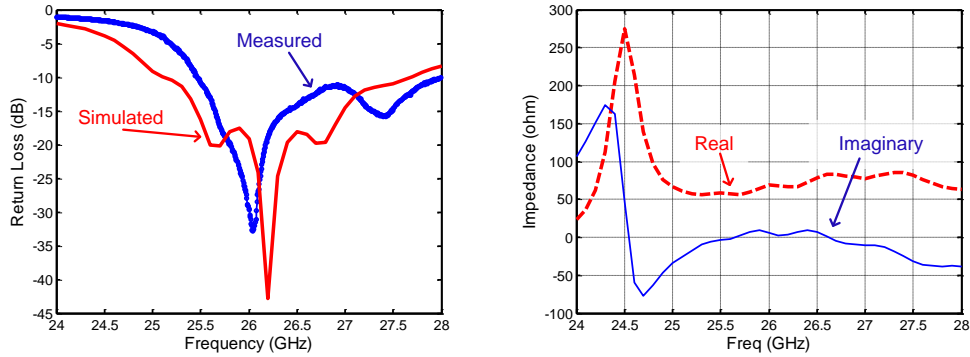


Figure 3.10: Photograph of 8X1 GCPW linear series array as designed and fabricated.

used to connect the elements in the linear series arrays with the 50Ω feed network lines. The linear series arrays are additionally simulated in HFSS. Allowing for fabrication tolerances, the nominal simulated design along with scaled versions ($\pm 3\%$) are fabricated and tested. The $+3\%$ case produced the best results in terms of matching and bandwidths. This discrepancy between the simulation and design can be attributed to the effects of the double rows of vias that are used to ground the CPW in the fabricated structure. These were not considered in the full wave simulation.

The return loss obtained by both simulation and measurement is shown in Figure 3.11(a) and is less than 10dB over the band of interest. The slight discrepancy between the measured and simulated values is attributed to the inter-element



(a) Simulated and measured return loss for the 8X1 linear series array with associated transition. (b) Simulated input impedance for the 8X1 linear series array with associated transition.

Figure 3.11: Return loss and input impedance for the 8X1 GCPW linear series array as designed and fabricated.

line lengths connecting the radiating elements in the series array, as previously discussed, and the high sensitivity of the response to these lengths. The simulated input impedance is shown in Figure 3.11(b); it is observed that the series combination of the parallel circuits does yield approximately 50Ω at the input to the series array. The simulated and measured gain pattern for the 8X1 series array over the band of interest is displayed in Figure 3.12. The gain is fairly consistent at high, low and mid-band. An overall beam squint of approximately 11° is noted in the elevation plane at the center frequency of 26GHz. This is the result of the traveling wave associated with the series fed geometry. Ultimately, this beam squint is desirable at this stage in the design as it allows for the RCS of the array to be distinguished from that of the flat metal ground plane.

The linear array simulation is repeated in MATLAB with the antenna elements and interconnecting lines modeled in their equivalent microstrip form similar to the sketch presented in Figure 3.13. This numerical model is required to handle the large number of elements present in the final array structure which is computationally too large to be modeled using full wave techniques. The pattern of the individual radiating patch elements developed in Equations 3.7 - 3.10 are combined with an additional

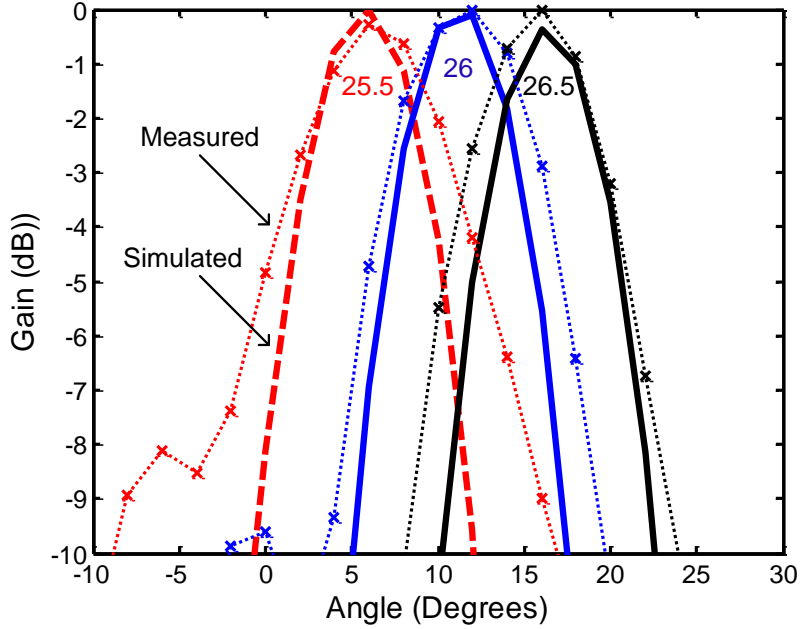


Figure 3.12: Simulated and measured normalized gain pattern for the 8X1 GCPW linear series array with associated transition. The gain patterns are shown for 25.5GHz, 26GHz and 26.5GHz, the low, middle, and high ends of the operating band.

array factor resulting from the combination of the eight individual radiating elements along the y-direction.

$$AF_{y2} = \sum_{n=1}^8 e^{j(n-1)kd \sin \theta \sin \phi} \quad (3.19)$$

This numerical simulation of the gain pattern for the 8X1 linear array is compared to that obtained from full wave analysis in Figure 3.14. The intra-element spacing for the linear array is slightly increased in the numerical model to obtain good agreement between the two forms of simulation. This slight discrepancy is believed to be the result of discontinuities between the feed line and the radiating elements that are not accounted for in the numerical model.

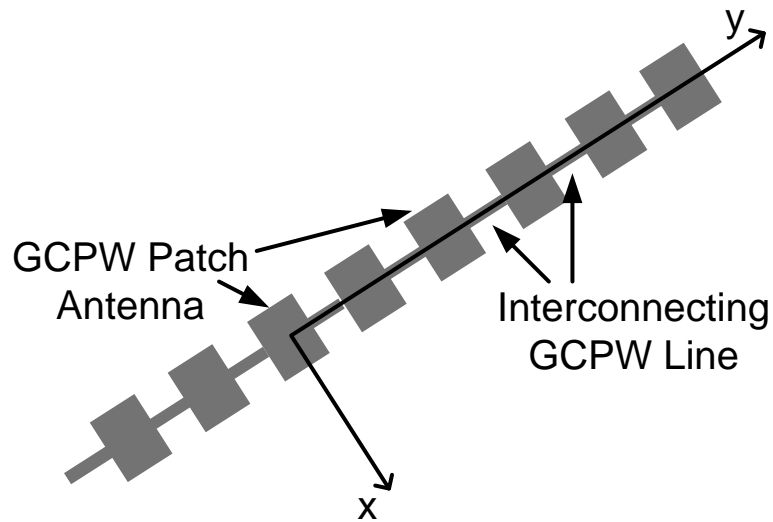


Figure 3.13: Geometry of an eight element linear array of microstrip patch antennas used for the numerical gain pattern calculation.

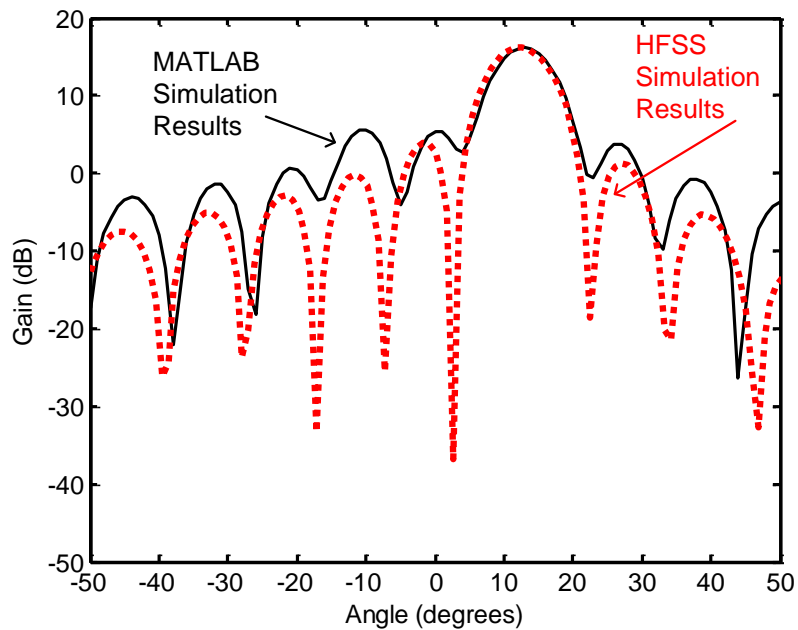


Figure 3.14: Comparison of HFSS and MATLAB simulated gain patterns for an 8X1 linear series array at 26GHz. Good agreement is shown between the two forms of simulation.

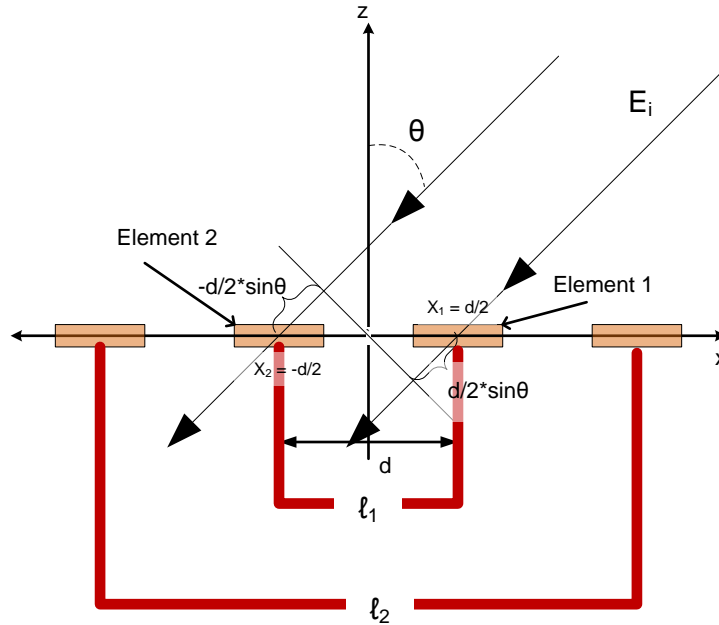


Figure 3.15: Geometry for the calculation of RCS from a Van Atta Array. Geometry of two element pairs is shown but extension to more element pairs is straightforward.

3.4 Passive Retro-Reflective Array Design

The numerical model for the linear series arrays is then extended to form the entire 8x8 Van Atta array pattern. The linear 8X1 series array is treated as a single element and, using its previously defined radiation pattern, the re-radiated field from the full 8X8 modified Van Atta array can be determined numerically. For the linear array situated in the x-z plane as depicted in Figure 3.15, a single pair of these linear series array radiators, identified as Element 1 and Element 2, illuminated by an incident electric field is first considered. These antennas, in the Van Atta configuration, are linked by a transmission line of length l_1 from feed point to feed point. The re-radiated field is modeled as the radiation of the identical array excited by the incident signal with the additional consideration of the phase delay induced by the interconnecting transmission line linking the element pairs [14], [36]. The result from this single pair is then extended to form the entire eight element array response.

The incident field on Element 1 at a position $x_1 = \frac{d}{2}$ is defined as:

$$\bar{E}_i = E_o e^{-j\hat{k}\cdot\hat{r}} = E_o e^{-jk_o r_1 \sin \theta_i} \quad (3.20)$$

When multiplied by the element pattern, $A(\theta_i, \phi_i)$, this gives rise to the total received pattern of :

$$\text{Receive Pattern} = A(\theta_i, \phi_i) e^{-jk_o r_1 \sin \theta_i} \quad (3.21)$$

Upon inception, the signal travels through the transmission line interconnecting each element pair, which induces a delay equivalent to:

$$\text{Delay Through Transmission Line} = e^{j\beta\ell} \quad (3.22)$$

The signal is then retransmitted from the alternate linear array pair, Element 2, at position $x_1 = \frac{-d}{2}$ with :

$$\text{Transmit Pattern} = A(\theta_t, \phi_t) e^{jk_o r_2 \sin \theta_t} \quad (3.23)$$

Hence, the total reradiated field is specified as the combination of the incident waveform, the receive pattern, the time delay through the line, and the transmit pattern. The combination of Equations 3.20 - 3.23 results in the total retransmitted pattern of the linear array pair:

$$\text{Retransmitted Pattern} = A(\theta_i, \phi_i) e^{-jk_o r_1 \sin \theta_i} e^{j\beta\ell} A(\theta_t, \phi_t) e^{jk_o r_2 \sin \theta_t} \quad (3.24)$$

where θ_i and ϕ_i define the angle of incidence and θ_t and ϕ_t define the angle of re-radiation.

To extend this result to the entire array, the patterns of the additional array pairs

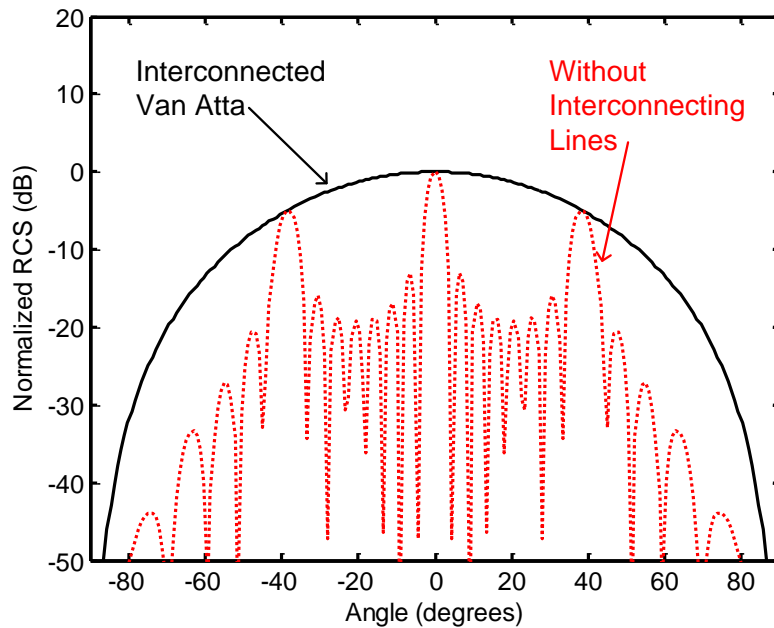


Figure 3.16: MATLAB simulation of the normalized horizontal plane RCS pattern for 8X8 element passive retro-reflective array compared to the identical array without the feed network.

are combined in phase. The patterns for the additional element pairs are formed in the same manner, taking into account the position of the array element pairs with respect to the array center along with the additional lengths of the feed network transmission lines required.

From the ideal simulation, the effect of the properly phased feed network lines on the operation of the Van Atta array in the horizontal plane in Figure 3.16 is observed for a backscatter configuration ($\theta_i = \theta_t, \phi_i = \phi_t$). It is apparent that the presence of the feed network creates a very broad retro-reflectivity in the horizontal plane. This is also compared to the array without the interconnecting feed lines. This direct backscatter response is very narrow.

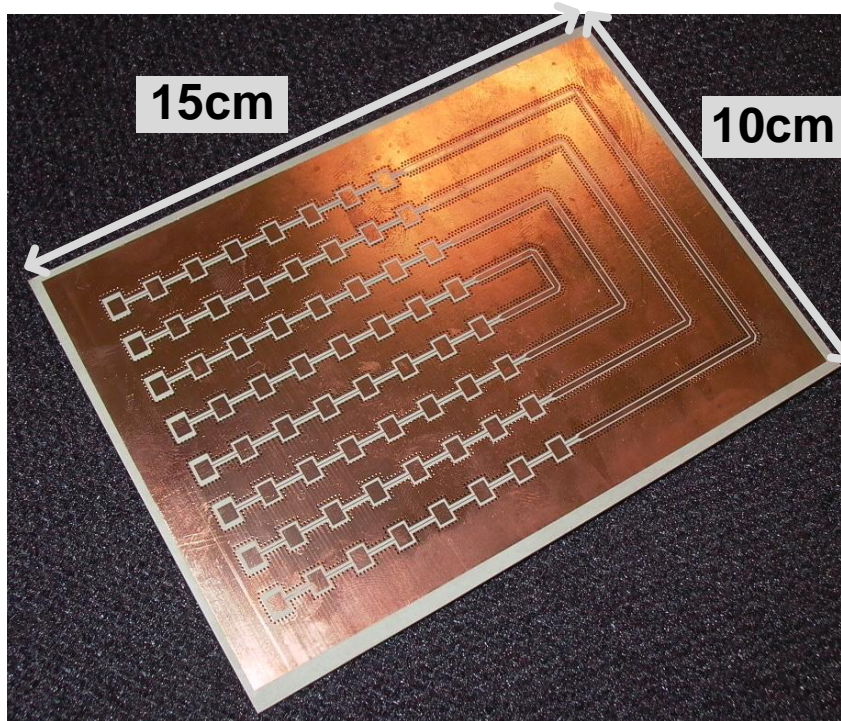


Figure 3.17: Photograph of the fabricated passive 8X8 retro-reflective array.

3.5 Passive Retro-Reflective Array Measurements

The entire 8X8 Van Atta retro-reflector is fabricated by integrating the appropriate length feed lines with the 8X1 GCPW linear series arrays. The resulting structure is pictured in Figure 3.17. This design is entirely passive and the RCS magnitude and the RCS response as a function of angular incidence are used to quantify the overall array performance.

The antenna is measured at a distance of 14 meters in the University of Michigan anechoic chamber using a radar fashioned from a network analyzer, two horn antennas, and an amplifier. The return signal is collected at various azimuth and elevation angles. The method of substitution is used to determine the total RCS of the Van Atta retro-reflector.

For this method, the received power is collected for a target with a known RCS, such as a metallic sphere. For identical measurement configurations, the ratio of the

received power from the unknown target (P_r^u) to that of the calibration target (P_r^c) is equivalent to the ratio of cross sectional areas.

$$\sigma_u = \frac{P_r^u}{P_r^c} \sigma_c \quad (3.25)$$

As the exact, theoretical RCS for a metallic sphere is a known quantity, comparing this value to that which is measured in the laboratory environment accounts for system losses and variations. Their contributions to the measurement can be accounted for thus allowing for the absolute determination of the backscattered RCS of the retro-reflective array.

As depicted in Figure 3.18, a relatively high horizontal-plane RCS response is observed for the fabricated array. This RCS pattern is obtained using gated time domain measurements over the band of interest. The measured RCS pattern for an identically sized flat metallic plate is included for comparison. The lack of dependence on azimuthal angle of the RCS demonstrates the retro-reflective capabilities of the fabricated array. The absolute RCS of the passive retro-reflector is consistent with the predicted value of Equation 1.7 of 0dBm. This predicted value includes the gain of the individual radiating elements and the losses of the GCPW feed network transmission lines. The slight rippling present in this response is attributed to the impedance mismatch between the lines connecting the linear series arrays and the 50Ω feed network lines. Overall, a broad retro-reflective response is noted in the horizontal plane for $\pm 30^\circ$.

3.6 Conclusions

This chapter introduces a high-RCS alternative to the traditional passive Van Atta retro-reflector array topology for operation on metallic surfaces. GCPW linear series arrays are introduced into the traditional passive Van Atta architecture to increase the

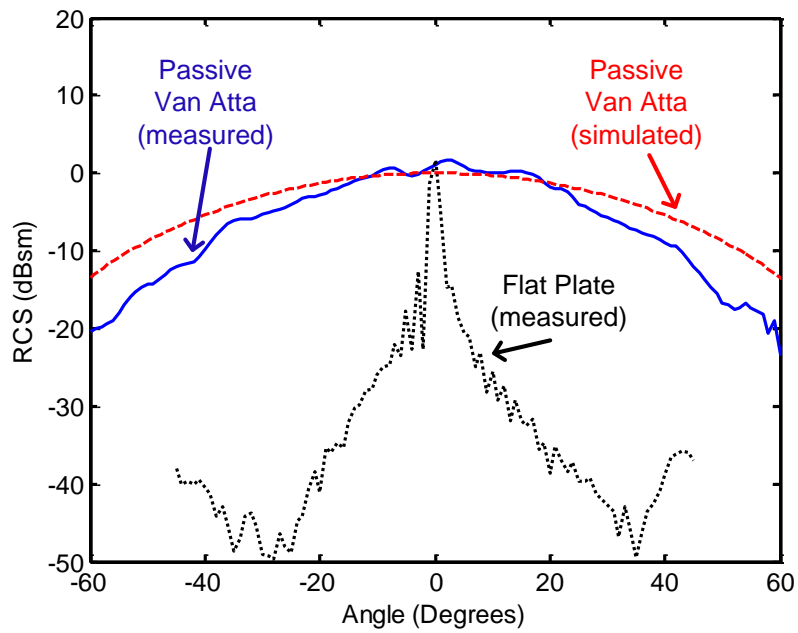


Figure 3.18: Horizontal plane RCS pattern measurement for the passive high-RCS retro-reflective array compared to that of a normalized identically sized flat plate. Both measurements are limited over the band of operation. The ideal MATLAB simulation of the 8X8 retro-reflective array is included for comparison.

gain by a factor of the square of the number of elements and maintain the bandwidth. The design methodology is detailed along with the development of a numerical model to predict the overall retro-reflector behavior. Good agreement is shown between simulated and measured performance and a broad horizontal plane RCS is obtained for a $\pm 30^\circ$ range of incidence angles. This structure achieves approximately 0dBm from a 10cm X 15cm footprint.

CHAPTER IV

Active High-RCS Retro-reflector Architecture

4.1 Introduction

For highly cluttered environments, range gating alone is insufficient for target identification. While the performance of the high RCS retro-reflective array structure presented in Chapter III is undisturbed by the presence of metallic surfaces, the large clutter backscatter contributed by the large metallic structures presented in the application scenario would certainly hinder the identification of any reasonably sized retro-reflective array. For such highly cluttered environments, modulation may be introduced into the passive retro-reflective array. This provides an aide to further distinguish the array from the clutter while also providing a means for unique identification. In this chapter, modulation is introduced into the passive retro-reflective array architecture introduced in Chapter III through the integration of active switching components into the feed network transmission lines. The design and operation of this active retro-reflective array are subsequently discussed and improvement in overall system performance is confirmed.

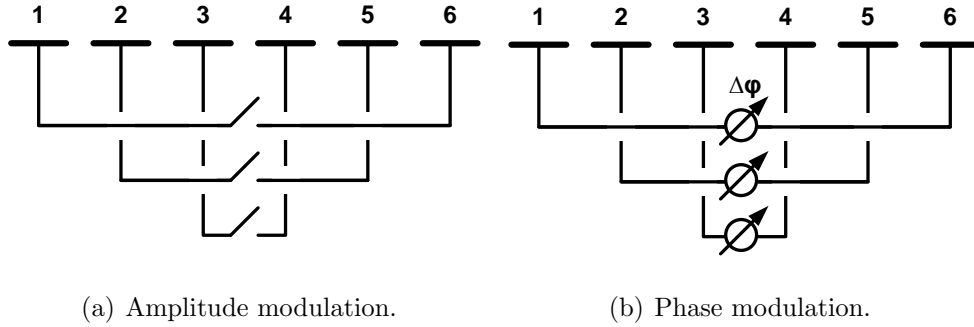


Figure 4.1: Potential modulation schemes for the active high-RCS retro-reflective array.

4.2 Introduction to RCS Modulation

RCS modulation is essential in complex environments as it helps to distinguish the target of interest from background clutter and various targets from one another. Additionally, this modulation provides an avenue for the relay of information from the target to its interrogating device. Figure 4.1 illustrates two general modulation schemes well suited for integration with a planar retro-reflective array. For amplitude modulation, illustrated in Figure 4.1(a), a switch is placed within the line connecting each antenna pair. This switch guides the signal to either a matched load or to its corresponding transmit antenna [37]. From an overall array standpoint, the retro-reflected signal is turned either on or off, effectively modulating the backscattered RCS. For phase modulation, illustrated in Figure 4.1(b), a phase shifter is placed in the path of the feed network transmission lines. When in the on position, the phase shifter adds a prescribed phase shift between the received and transmitted signal. By turning the phase shifter on and off, the overall antenna RCS is effectively turned on or off when interrogated from a stationary observation point.

As previously discussed in Section 3.2, the GCPW topology employed in the design of the feed network lines provides an ease of integration for these active components into the overall array structure. The proximity of the ground plane in the GCPW topology allows both series and shunt elements to be mounted into the circuit without

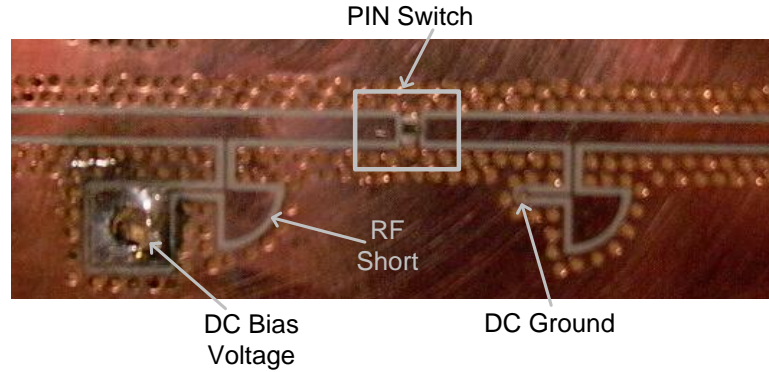


Figure 4.2: Photograph of the PIN diode switch as integrated into a retro-reflective array feed network line and its associated bias circuitry.

the need for additional vias.

4.3 Design and Implementation of Active Modulation

For this active retro-reflector design, amplitude modulation is chosen and switches are integrated into the feed network transmission lines. The switching elements used in this design are MaCOM MA4SW110 PIN diode switches. A total of four switches are required to effectively modulate the entire 8X8 element array. An example switch and bias network are pictured in Figure 4.2. Each switch requires about 20mA of current at 1V of bias voltage. The switches operate up to 26.5GHz, the upper edge of the desired band of the array. The bias of these switching elements is controlled in parallel, allowing simultaneous control of all four switches and their associated losses contribute to $\sim 3\text{dB}$ reduction in RCS for the overall retro-reflective array.

The placement of these switches within the feed network lines is also an important design consideration effecting the overall operation of the retro-reflective array. Ideally, short circuits should be observed at the array input terminals when the switches are biased in the off position. This minimizes the RCS of the individual radiating elements allowing for a maximum on-to-off RCS ratio [38].

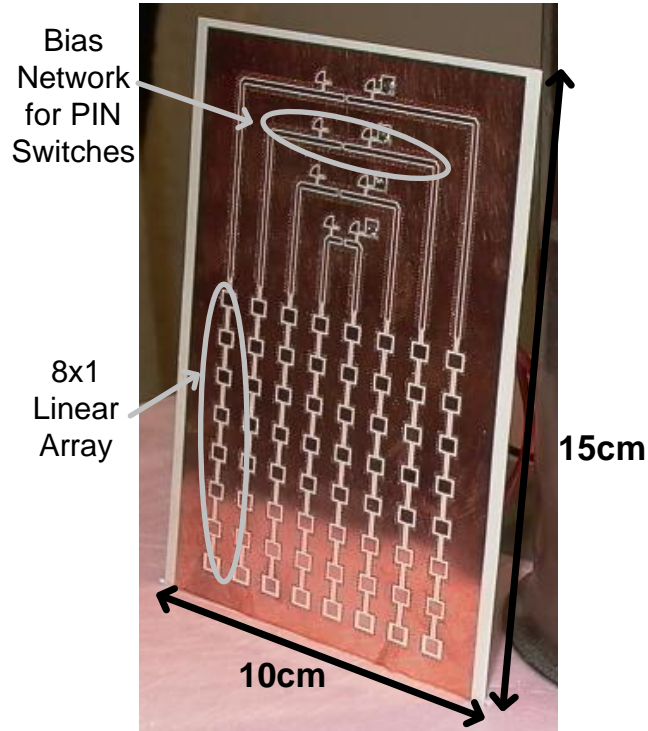


Figure 4.3: Photograph of fabricated 8X8 active retro-reflective array.

4.4 Active Retro-Reflective Array Measurements

The active 8X8 retro-reflective structure is designed and fabricated using the passive retro-reflective array structure described in Chapter III with the addition of four PIN diode switches and their associated bias networks into the array feed network transmission lines. A photograph of the overall 8X8 array, with switches and bias circuitry, is shown in Figure 4.3.

The RCS of this active retro-reflective array is measured in the anechoic chamber in a manner identical to that of the passive array using a network analyzer based radar system. The switches are simultaneously biased in either the on or off position. RCS variation with angle in both the on and off states is used to quantify array performance. As seen in Figure 4.4, a relatively high RCS response is observed in the on state; its lack of dependence on azimuth angle demonstrates the retro-reflective capability of the active retro-reflective array. The RCS in the on state is nearly

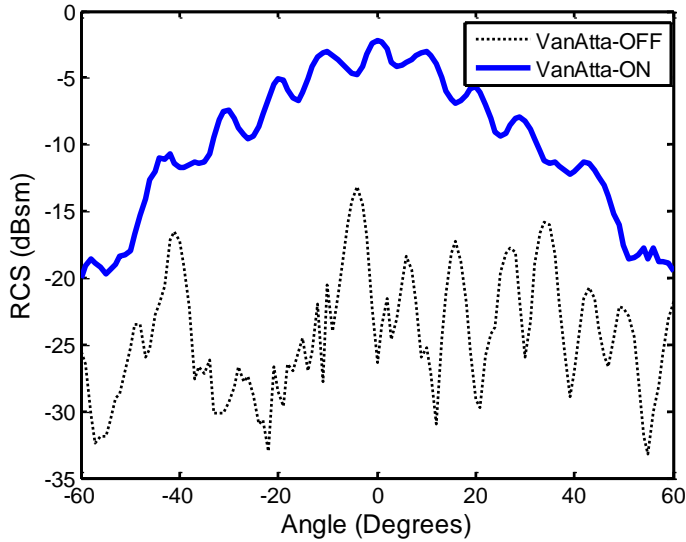


Figure 4.4: RCS pattern of the active retro-reflective array with switches and battery pack. The RCS performance is compared for both the on and off states of the switching elements.

identical to that of the entirely passive array in Figure 3.18, save the additional loss contributed by the switch elements and bias networks. This is compared to the identical measurement repeated with the switches in the off position. A significant increase in RCS is noted from the on position compared to the off.

While slight rippling is observed in the passive array of Section 3.5, significant rippling is noted for this active retro-reflective array. This is again attributed to reflections caused by discontinuities along the feed network line, but increases in magnitude for this active counterpart due to the additional discontinuities introduced by the presence of the switches and their associated bias circuitry.

Additionally, it is noted that the placement of the switches in the off state led to periodic peaks in the RCS response. Signals reflected from the short-circuited switching elements propagate back to the series antenna elements in phase for specific angular positions. Further testing using copper tape to change the location of the short circuits in the lines resolved this issue. This analysis determined that staggering the location of the active modulating components is optimal.

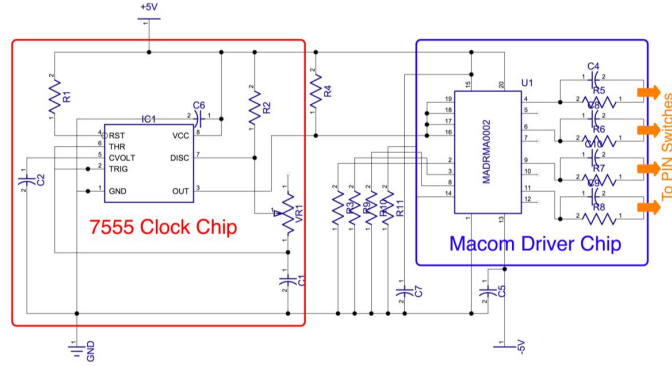


Figure 4.5: Circuit diagram of the bias network implemented for stand alone operation of the active high-RCS retro-reflective array tag.

4.5 Active Retro-reflective Array Performance in a High Clutter Environment

The performance of this tag is then confirmed in a high clutter environment outside of the anechoic chamber. To achieve portability for a stand alone tag, a driver circuit is required to provide power and control the current and bias voltage delivered to the switches. The driver circuit diagram and photograph of associated board layout are shown in Figure 4.5 and Figure 4.6. A MaCOM driver chip (MADRMA0002) and 7555 clock chip at a frequency of approximately 1.5Hz are used in initial testing. For later versions of this tag, the on/off sequence is determined by a more complex m-sequence pseudo-noise (PN) code generator circuit. The m-sequence is a code that is set to uniquely identify each individual retro-reflective array tag.

To mimic a large quantity of clutter, an assortment of indoor objects and a number of trihedral corner reflectors are placed at various ranges with respect to the radar, but still in close proximity to the active retro-reflective tag as shown in Figure 4.7. The network analyzer-based radar system is set up in the same manner as the chamber measurement, with two horn antennas and appropriate amplification. The tag is placed atop a pedestal next to a metal cabinet.

The active retro-reflective array is measured in this high clutter environment and

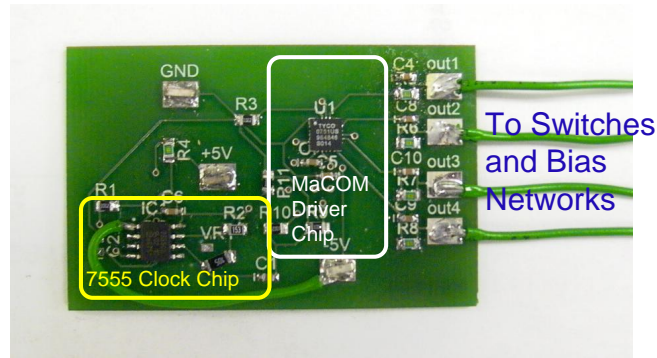


Figure 4.6: Photograph of the driver circuit board layout of Figure 4.5 as fabricated for portable operation.

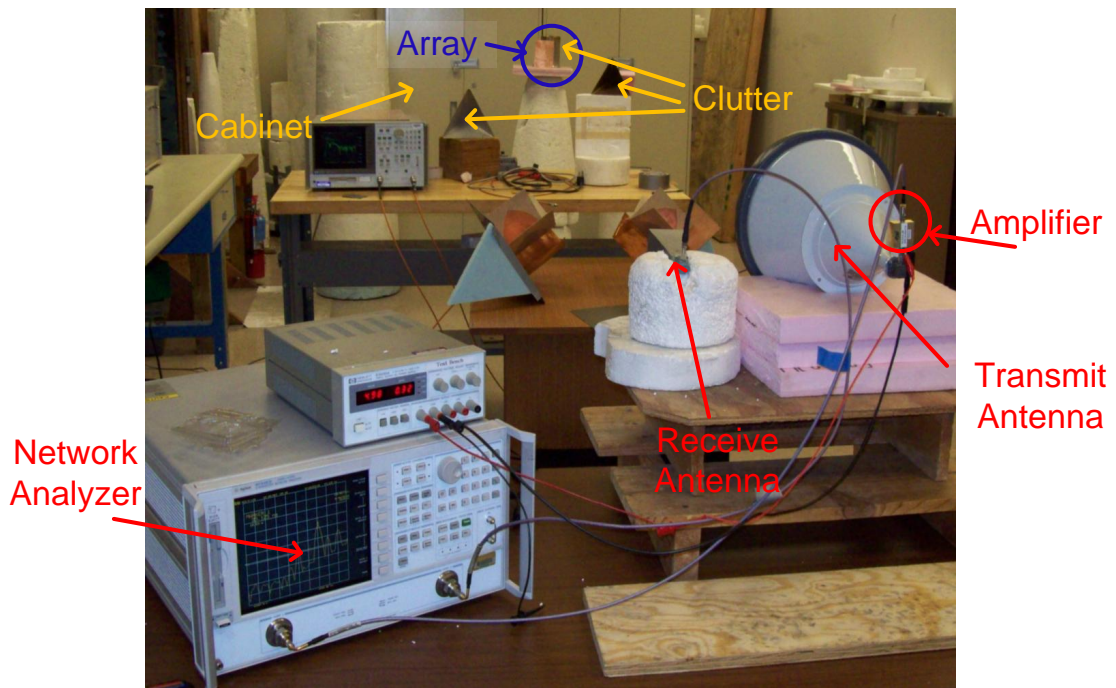
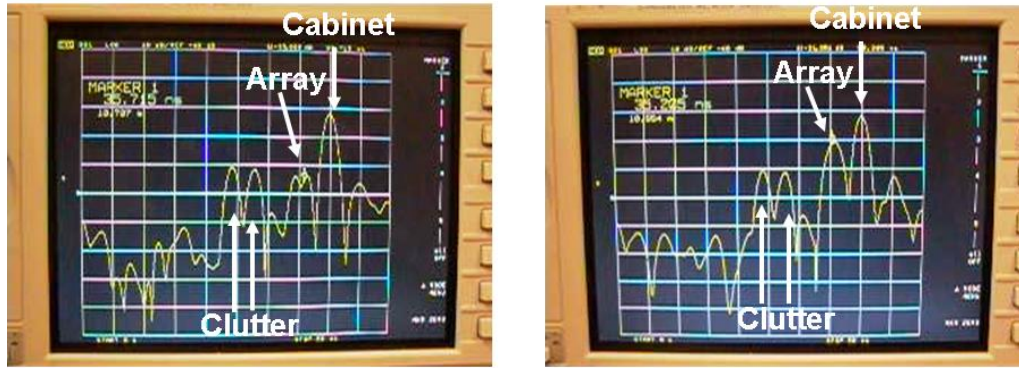


Figure 4.7: Photograph of the high clutter measurement setup for the active retro-reflective tag. An assortment of trihedral corner reflectors are placed near the tag to determine its ability to distinguish itself from other targets not of interest.



(a) Off State.

(b) On State.

Figure 4.8: Monostatic return signal of the active retro-reflective tag in the high clutter environment pictured in Figure 4.7. The on and off performance is compared.

the results are shown in Figure 4.8. The additional clutter contributed by the environment is noted on the network analyzer screen along with the target of interest. An 8dB variation is observed comparing the RCS when the array is on compared to the off state. Additionally, the subtraction of two successive measurements could be performed to cancel out all time-stationary clutter as will be demonstrated in later sections of this chapter.

4.6 Active Tag and Radar System Measurements

To achieve an overall detection system, this active retro-reflective array tag is integrated with a 26GHz Ultra-wideband Rangefinder Radar developed by McEwan Technologies [39]. This radar, pictured in Figure 4.9, is very low cost, small in size, and has a quoted range resolution of less than 1mm. It has a PRF of 5MHz and a modified sweep rate of 8.33Hz with an output power of +3dBm. More relevant parameters are listed in Figure 4.10 and detailed information regarding the operation of this radar can be found in [39].

A six inch dielectric lens is added to the radar as shown in Figure 4.11(a) and Figure 4.11(b). This lens is manufactured by Quinstar [40]; the focal length of the lens

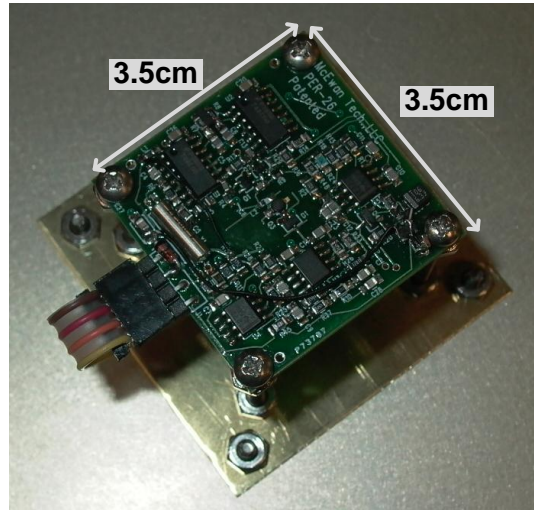
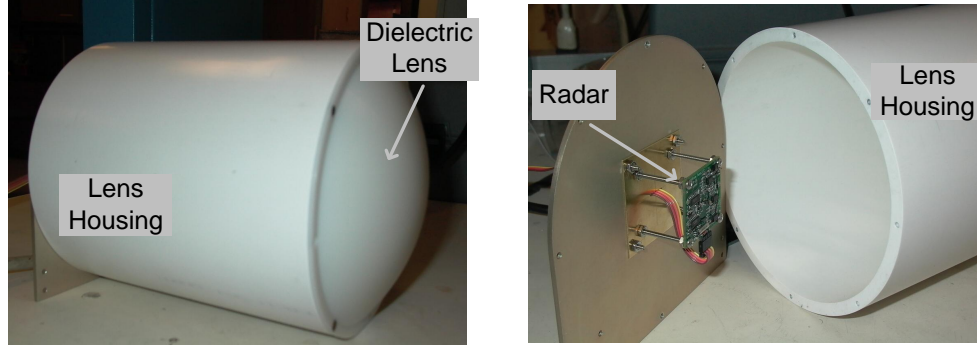


Figure 4.9: Photograph of the 26-GHz Ultra-Wideband Rangefinder Radar.

Relevant Radar Parameters

Parameter	Value
Range	0.5 to 10 meters
Range Resolution	<1mm
Range Linearity	<1% of full scale
Range Stability	<0.1m over -55 to 65°C
RF Center Frequency	26±0.25GHz
Peak RF Output	+3dBm
RF Pulse Width	800ps
PRF	4MHz
RF Duty Cycle	0.32%
Video Output	>±1.5Vpk, 29kHz carrier, +2V offset
Beamwidth	8° @ -3dB, 36° @ -20dB
Power	4.75 to 5.25 Vdc, 17mA @5V
PCB Size	1.5" by 1.5"

Figure 4.10: Relevant parameters for McEwan 26GHz Rangefinder.



(a) Photograph of the dielectric lens. (b) Photograph of radar mounted in the dielectric lens.

Figure 4.11: Dielectric lens and radar system used for the system validation measurements.

is nearly equal to its diameter ($\frac{f}{d} \approx 1$) and it is constructed of low dielectric material. This modification increases the accuracy of determining the angular direction of the tag location along with the overall gain of the radar.

The active high-RCS retro-reflective array shown in Figure 4.3, driver circuit pictured in Figure 4.6, and the radar-lens reader of Figure 4.11 are tested together. The retro-reflective array is placed atop a pedestal a distance of 4m from the radar. A photograph of the test set-up is shown in Figure 4.12. The radar's video output capabilities allow for tracking of the array performance on the screen of an oscilloscope using an interface cable. From comparison of the still screen shots in Figure 4.13, the modulated return signal from the active retro-reflective array is easily observed.

4.7 Pulse-to-Pulse Subtraction for Enhanced Target Distinction

The stand alone active retro-reflective tag assembly is pictured in Figure 4.14. This includes a case specifically designed to house the active retro-reflective array, driver circuit and batteries. It additionally provides structural support. A detailed rear view of this retro-reflective tag is pictured in Figure 4.15. In this photograph, the

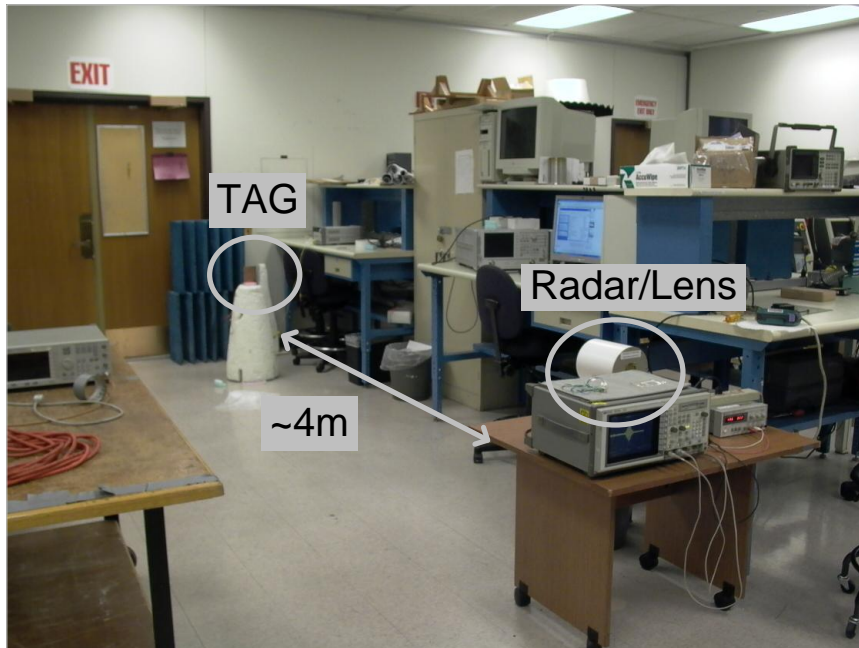
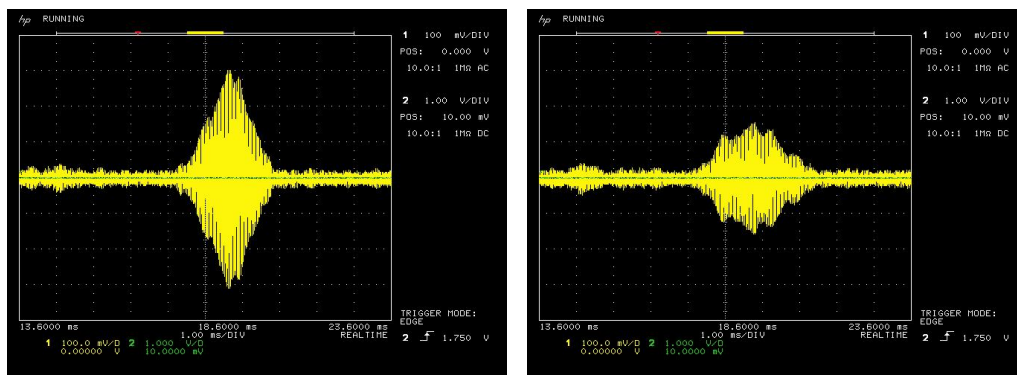


Figure 4.12: Photograph of the complete system test set-up.



(a) Retro-reflective tag on.

(b) Retro-reflective tag off.

Figure 4.13: The video output signal collected by the radar comparing the on and off states of the active retro-reflective tag.

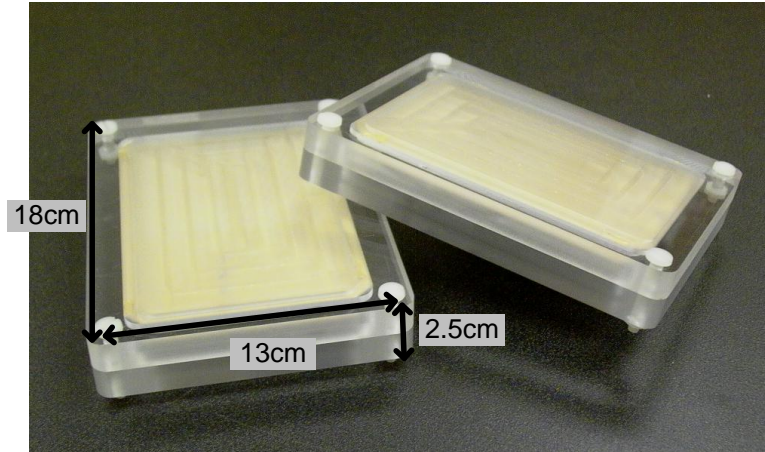


Figure 4.14: Photograph of two active retro-reflective arrays in associated cases.

case is open, revealing the batteries and driver circuit used to operate the switching elements of active retro-reflective array.

The response of this active target is collected in the laboratory environment using a specially designed LabView program. The radar is used to interrogate the scene, and subsequent pulses are subtracted from one another. Figure 4.16(a) shows the acquired response of the radar and the on/off modulation of the active retro-reflective array tag is noted over the time sample. The frequency of this modulation is set by the driver circuit and specific to each retro-reflective array. In Figure 4.16(a), backscatter response of clutter can be observed both before and after the modulating tag of interest. Figure 4.16(b) shows the results after the implementation of pulse-to-pulse subtraction. The response of all time stationary clutter is removed from the scene and distinction of the active retro-reflective array is improved.

4.8 Conclusions

This chapter demonstrates a new method for the detection and tracking of metallic objects at 26GHz. Modulation is introduced into the passive high-RCS retro-reflective array presented in Chapter III to provide the active tag with its unique identification sequence in the form of a clock frequency. The performance of the switching elements

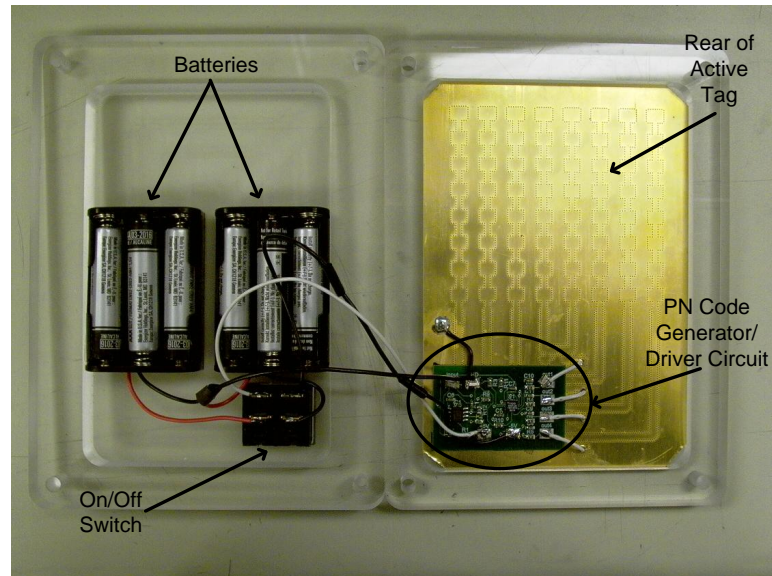
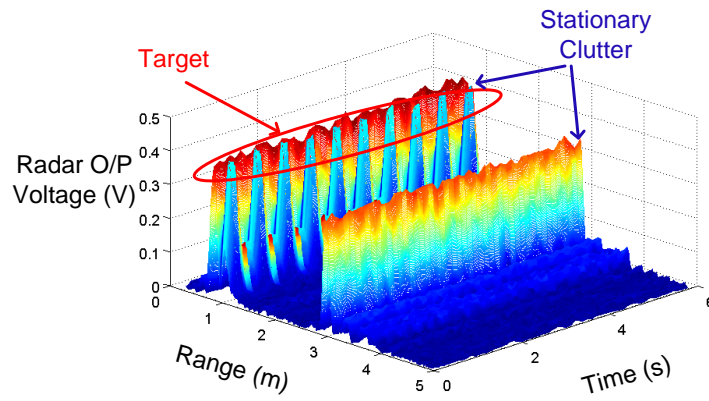


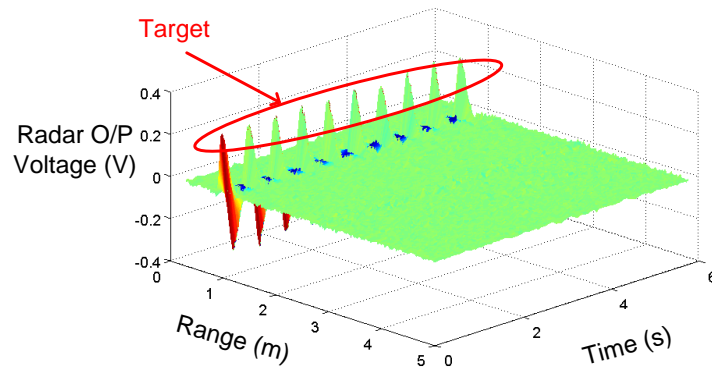
Figure 4.15: A detailed rear view of active retro-reflective array in associated case.

is confirmed by the RCS pattern comparison of the active tag in both its on and off states. An 8dB variation between the on and off performance of the array is demonstrated. Additionally, the performance of the active array is demonstrated in a high clutter environment and the modulation shown to distinguish the response of the tag from that of the surrounding clutter. This modulation is additionally used in conjunction with pulse-to-pulse subtraction and shown to further enhance distinction by removing the response of all time-stationary clutter.

The design and implementation of the active circuit is detailed and the performance of the overall system is demonstrated using a very low cost and low featured radar. The operation of the active tag is validated and overall detection system, including background subtraction, is confirmed via a mock application scenario constructed in the laboratory setting.



(a) Before Subtraction.



(b) After Subtraction.

Figure 4.16: Performance of active retro-reflective tag before and after pulse-to-pulse subtraction.

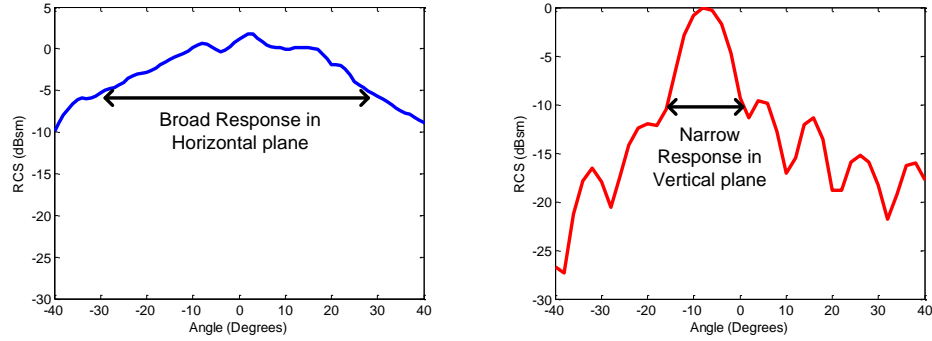
CHAPTER V

Techniques for Vertical Plane Beam Broadening

5.1 Introduction

An increase in the RCS of a target provides greater ease of target distinction. For this reason, maximization of the RCS of the retro-reflective structure is highly desirable and the subsequent driving force in most retro-reflector design decisions. To achieve this higher RCS from a planar retro-reflector configuration generally requires an increase in the number of radiating elements. This increase in the number of array elements comes either at the cost of decreased bandwidth or a narrow beam in elevation as previously discussed in Section 3.5. While a narrow elevation beam may be useful in some applications, namely those requiring a secure line of communication, its drawback includes a difficulty in achieving precise alignment between the retro-reflective tag and its associated interrogating device.

For the passive retro-reflective array presented in Chapter III, a squint is introduced into the pattern of the linear series array elements. This allows for the separation of the retro-reflective response from that of the flat plate produced by the ground plane. The RCS pattern measurements of this standard passive retro-reflective array are again illustrated in Figure 5.1. This structure exhibits a broad retro-reflective response in the horizontal plane as observed in Figure 5.1(a). Inspection of the vertical plane response of this structure, shown in Figure 5.1(b), reveals a



(a) The broad horizontal plane pattern of the passive retro-reflective array of Chapter III. (b) The narrow vertical plane pattern of the passive retro-reflective array of Chapter III.

Figure 5.1: Comparison of the vertical and horizontal plane RCS patterns of the passive retro-reflective array configuration presented in Chapter III.

narrow range of operational angles in this plane. Additionally, this narrow range of operation exhibits an offset from boresight equivalent to the squint of the linear series arrays. The design presented in this chapter seeks to achieve a broad one-dimensional retro-reflective response for a large range of angles in the vertical plane. To accomplish this, the proposed approach exploits the off boresight squint of the linear series arrays to broaden the range of operation in the vertical plane.

This chapter begins by presenting the alternating-feed configuration. This novel feed architecture addresses the narrow vertical plane beam of the standard retro-reflective array while additionally reducing its size. This architecture does not require modification of the existing linear series feed array element design and is shown to achieve beam broadening at the unintended expense of a non-uniform RCS in the horizontal plane. To address the shortcomings associated with this non-uniform response, a novel closed-loop feed architecture is subsequently introduced. This architecture requires a new design for both the radiating elements and the feed network. This closed-loop architecture accomplishes overall beam broadening in the vertical plane while maintaining a smooth retro-reflective RCS response in the horizontal plane. Details of the design including simulation and measurements for both the al-

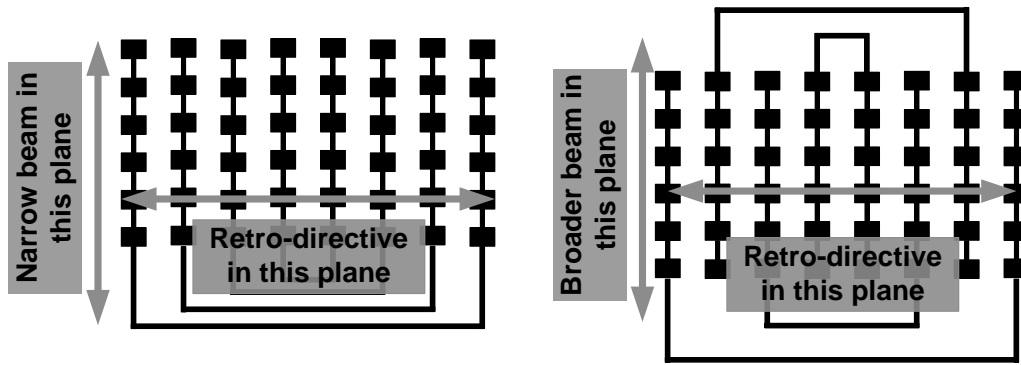
ternating and closed-loop feed architectures are presented. Overall array performance enhancements are discussed for these novel beam broadening architectures and this chapter concludes with a quantification performance enhancements.

5.2 Alternating-Feed Retro-reflective Array

5.2.1 Alternating-Feed Retro-reflective Array Introduction

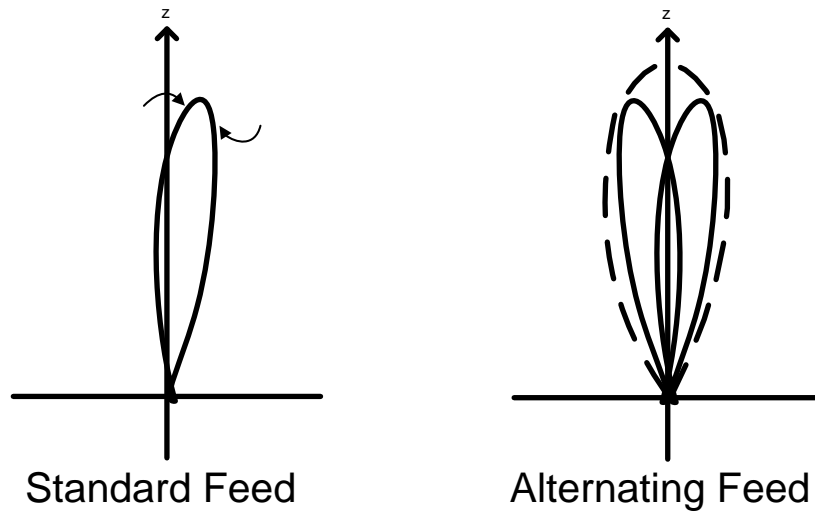
In a standard retro-reflective array, the radiating elements are connected as shown in Figure 5.2(a), with all the constituent linear series arrays oriented in the same direction. The result is a narrow beam in elevation, as illustrated in Figure 5.3(a), which can additionally be squinted to a desired angle through careful design of the linear series arrays. In applications where a broadened beam directed at broadside is ultimately desirable, the series arrays may be alternatively oriented as shown in Figure 5.2(b). In this arrangement, the feed of each array pair alternates from the top and the bottom. The pairs of linear array elements fed from the top exhibit a squint in one direction off broadside, while the linear array pairs fed from the bottom are squinted in the opposite direction. Figure 5.3(b) illustrates these two oppositely squinted beams along with the resulting combination, which produces a broadened beam at boresight. While initially it may appear the phase relationships between the flipped and un-flipped arrays would cancel at boresight, the vector of the incident E-field also flips following the direction of the feed of the antenna pairs. This results in in-phase addition for the combined beam, and likewise, overall beam broadening.

An additional benefit to this alternating-feed configuration is a reduction in the overall line lengths required for the feed network which leads to a decrease in the overall footprint of the array. The result of this new design is overall beam broadening in the vertical plane thus improving retro-reflective array performance over a broader range of elevation angles.



(a) The standard Van Atta interconnection for linear series-feed radiating elements. (b) The alternating-feed connection for linear series-feed radiating elements.

Figure 5.2: Comparison of standard and alternating-feed interconnection schemes for linear series-feed radiating elements. The alternating feed design will provide a wider vertical plane beam directed at broadside.



(a) The standard interconnection of radiating elements produces a narrow vertical plane beam. (b) The vertical beam produced by alternating the feed positions of linear series array pairs will enhance the overall beam at broadside.

Figure 5.3: Comparison of vertical plane beams produced by the standard and alternating feed interconnection schemes for linear series-feed radiating elements. The combination of the oppositely flipped linear array element pairs will provide a wider beam at broadside.

5.2.2 Alternating-Feed Retro-reflective Array Simulation

An initial analysis is performed in MATLAB to better understand the behavior of this alternating feed retro-reflective array and quantify the maximum level of beam broadening that can be attained by this configuration. For the numerical simulation, the single patch antenna element is modeled in a manner identical to that of a microstrip patch antenna, as two radiating slots separated by a distance equivalent to the length of the patch. These individual radiating patches are then combined with the array factor resulting from the linear combination of the radiating elements. This produces a numerical model for the entire linear array structure. More detail regarding this linear array model can be found in Section 3.3. The total number of elements in this linear array is reduced from eight to six to provide better control of the magnitude of the squint of overall structure.

Two separate models are required for the linear series array that are determined by the location of the feed. The beam produced by each linear series array is oriented either upward or downward with respect to the array center but always directed away from its feed position. The numerical model is verified by comparison with its full wave counterpart as shown in Figure 5.4. The inter-element spacing of the numerical model is adjusted slightly to achieve good agreement between both forms of simulation. The slightly higher sidelobe levels noted in the full wave pattern are most likely due to discontinuities from the junction of the feed lines with the patch elements along with slightly imperfect line lengths. Additionally, the reduced number of elements for this linear array produces a broader beam in horizontal plane of this structure when compared to the eight element linear arrays of Section 3.3.

The numerical formulation of the pattern for the upward and downward oriented linear series arrays can then be extended to form the gain pattern for the entire 6X8 alternating feed retro-reflective array structure. To accomplish this, each linear array is situated in the x-z plane but treated as a single element as depicted in Figure 5.5.

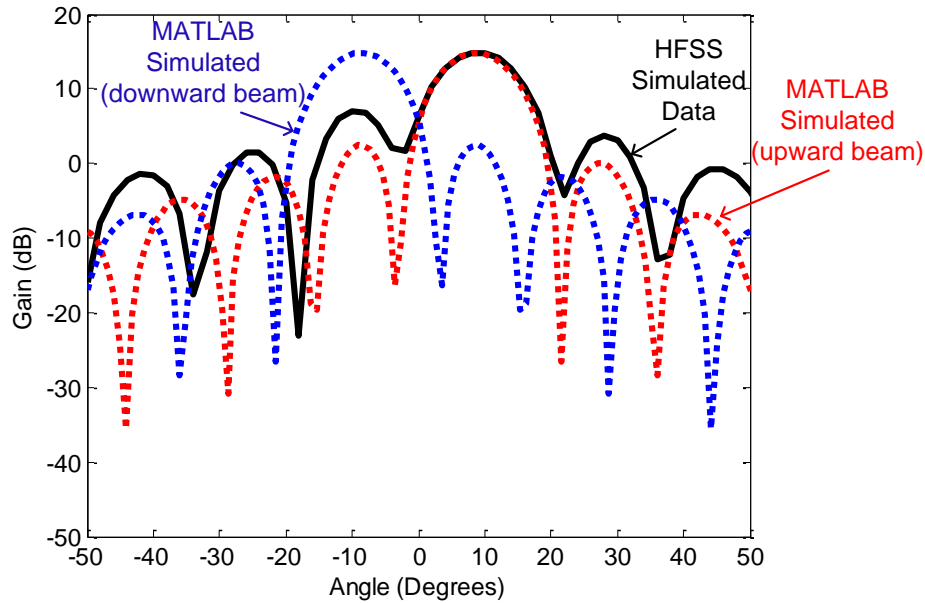


Figure 5.4: Numerically simulated gain pattern for both upward and downward feed orientations of linear series arrays compared with the full wave simulation for an upward oriented linear series array. Good agreement is noted.

The orientation (upward and downward) of each pair is alternated. Each pair is numerically interconnected with transmission lines exhibiting appropriate phase delays to mimic the wavelength multiples required for a retro-reflective architecture. Equations 3.20 - 3.24 are modified to include the appropriate upward and downward orientations of the linear array patterns.

From this ideal simulation, the performance of this retro-reflective array can be studied for a backscatter configuration ($\theta_i = \theta_t, \phi_i = \phi_t$). The appropriately phased feed network creates a very broad retro-reflectivity in the horizontal plane as observed in the broad RCS pattern in Figure 5.6. This is also compared to the response of a 9cm X 8cm flat plate whose horizontal plane RCS pattern is very narrow. It can also be noted that alternating the squint orientation of the linear series array elements in the vertical plane did not affect the overall retro-reflectivity in the alternate plane.

The squint of the linear series array elements is varied in the numerical simulation to determine the optimal degree of squint that would produce maximum beam

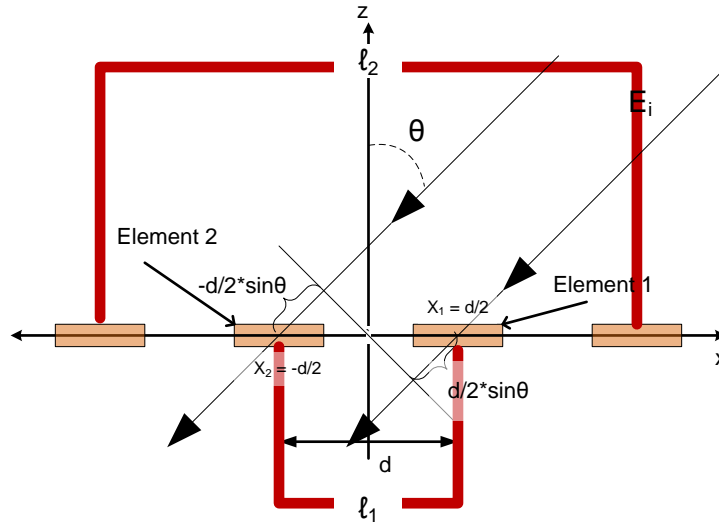


Figure 5.5: Geometry for the numerical RCS calculation for an alternating-feed retro-reflective array. The interconnection scheme of four total linear series array elements is illustrated.

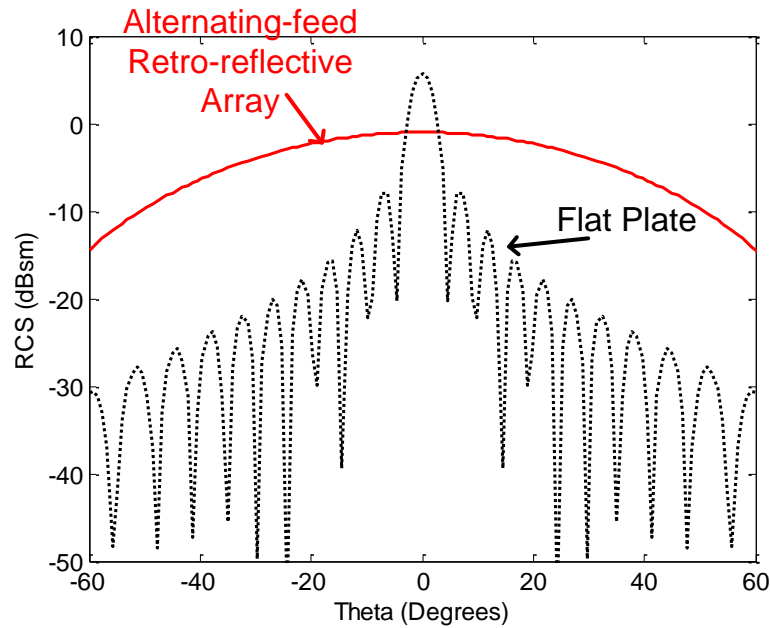


Figure 5.6: MATLAB simulation comparing the horizontal plane RCS for 6X8 element alternating-feed retro-reflective array to that of a 9cm X 8cm flat plate.

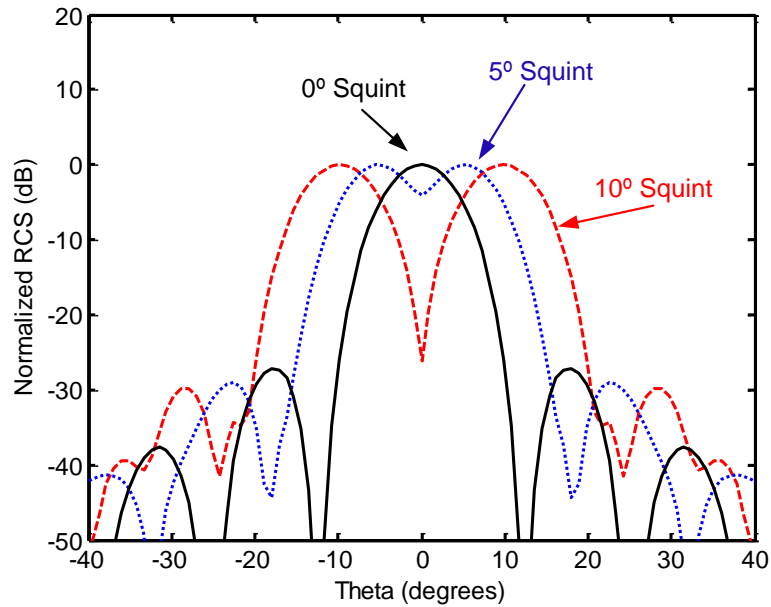


Figure 5.7: MATLAB simulation comparing values for the vertical plane squint of the linear series array elements and their effect on the alternating-feed retro-reflective array performance. An optimal value for overall beam broadening is obtained.

broadening in the vertical plane without causing the beam to separate into two independent beams. Figure 5.7 shows the results for 0° , 5° , and 10° of squint. Overall beam broadening is observed by comparing the beamwidths at 0° squint to the overall beamwidth for the case of 5° squint. For the case of the 5° squint, a much larger combined beamwidth is observed. For 10° of squint, the overall beam has separated into two independent beams.

5.2.3 GCPW Linear Series Array Design and Measurements

A six-element linear series array is designed and fabricated with a predetermined squint of 6° . Multiple design iterations are fabricated to account for imperfections arising from the etching process. A photograph of a single, fabricated, 6X1 linear series array is shown in Figure 5.8. The final element in the array differs from the previous elements due to varying load conditions.

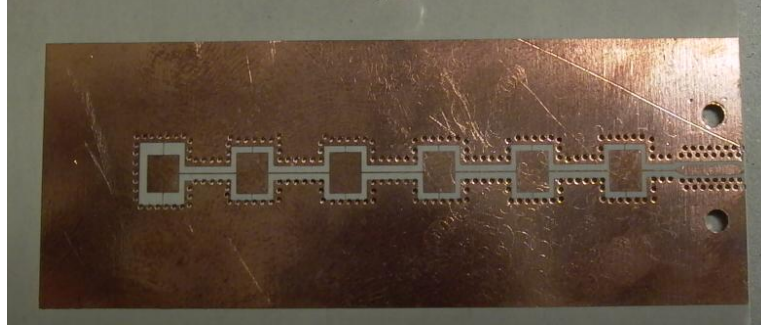
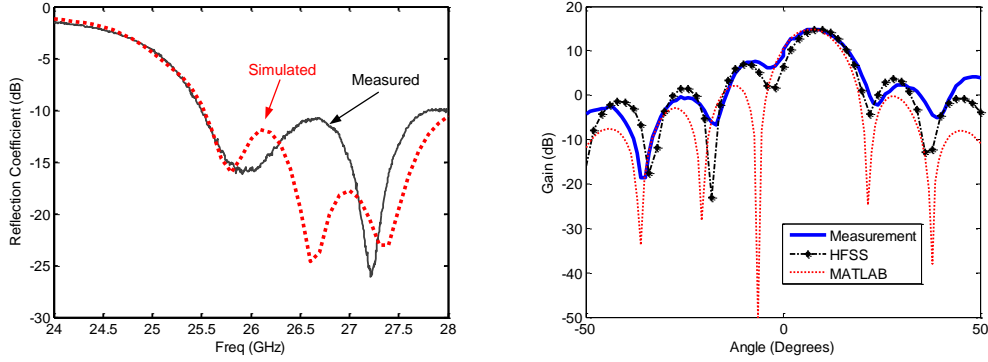


Figure 5.8: Photograph of a fabricated 6X1 linear array element for the alternating-feed retro-reflective array.

This fabricated linear array is measured in the laboratory environment and its performance compared to that predicted by simulation. Inspection of Figure 5.9(a) reveals that the reflection coefficient of the fabricated structure is consistent with that predicted by the full wave simulation. Additionally, the gain pattern of this linear series-fed array, displayed in Figure 5.9(b), shows good agreement to that predicted by both MATLAB and HFSS. The increased sidelobe levels can again be attributed to the discontinuities between the feed lines and the patch elements and the additional contribution of the metallized via holes that surround the transmission lines and patch elements. The double row of metallic via holes is not included in the full wave simulation to reduce the computational complexity.

5.2.4 Alternating-Feed Retro-reflective Array Design and Measurements

The fabrication of the entire 6X8 alternating-feed retro-reflective array requires the integration of the feed network transmission lines with the 6X1 linear series array elements. The design conditions to achieve retro-reflectivity for the feed network are consistent with those discussed in Section 3.2, i.e., provide identical phase delay relative to one another. The bend geometry is kept consistent among lines in order to eliminate this variable from the design process. Straight segments are altered to achieve identical phase delay among the four feed network lines to within a multiple



(a) Reflection coefficient of the fabricated 6X1 linear series array element compared with HFSS simulation. (b) Gain pattern of the fabricated 6X1 linear series array element compared to that predicted by both MATLAB and HFSS simulations.

Figure 5.9: Reflection coefficient and gain measurements for the 6X1 linear series array pictured in Figure 5.8.

of a wavelength.

The resulting alternating feed structure is pictured in Figure 5.10. Double rows of metallic via holes are again used to maintain good ground connection for the GCPW. This design is entirely passive and measurement of the RCS magnitude and the RCS response versus angle is used to quantify the overall array performance.

The fabricated alternating-feed retro-reflective array is measured in the anechoic chamber using the network analyzer based radar system discussed in Section 3.5. The monostatic return signal is collected at various angles and the method of substitution is employed to determine the total RCS of this retro-reflective array. Figure 5.11 presents the overall vertical plane response of the structure and is compared to that of the standard Van Atta array. A broadened beam is observed when compared to that of the standard array. The squint of the individual linear series arrays in the alternating-feed array is more severe than the calculated optimal value. Subsequently, two separate beams are noted instead of the desired broad and unified vertical plane beam. The peak at boresight noted in the vertical plane beam of the alternating-feed array response is due to the RCS of the ground plane. The ground plane exhibits

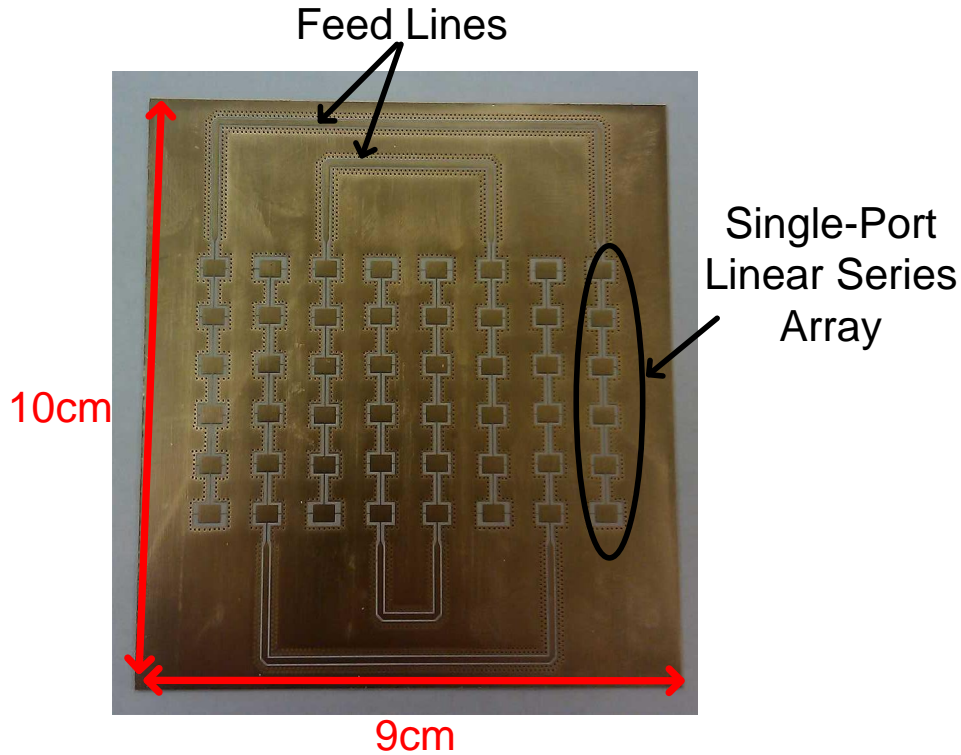


Figure 5.10: Photograph of a fabricated 6X8 alternating-feed retro-reflective array.

a narrow beam very similar to that of a flat plate and is highly dependent on the orientation of the array during measurement.

Figure 5.12 shows the horizontal plane RCS pattern measurement of this structure for two elevation angles, $\pm 4^\circ$, compared to the horizontal plane response of the standard passive Van Atta array. For the alternating-feed configuration, this horizontal plane response remains consistent over this 8° range of elevation angles. The position of the major nulls is attributed to the direct backscatter from the linear arrays which are out of phase with the retro-reflective response. For the tilted array, the elements that are spaced 1.6λ apart create a Bragg backscatter at approximately 18° from boresight. This strong backscatter can destructively interfere with the retro-reflective response and create a null in the horizontal plane RCS pattern observed in Figure 5.12. Anomalies such as these are undesirable for the proposed application scenario and thus limit the effectiveness of the alternating feed architecture.

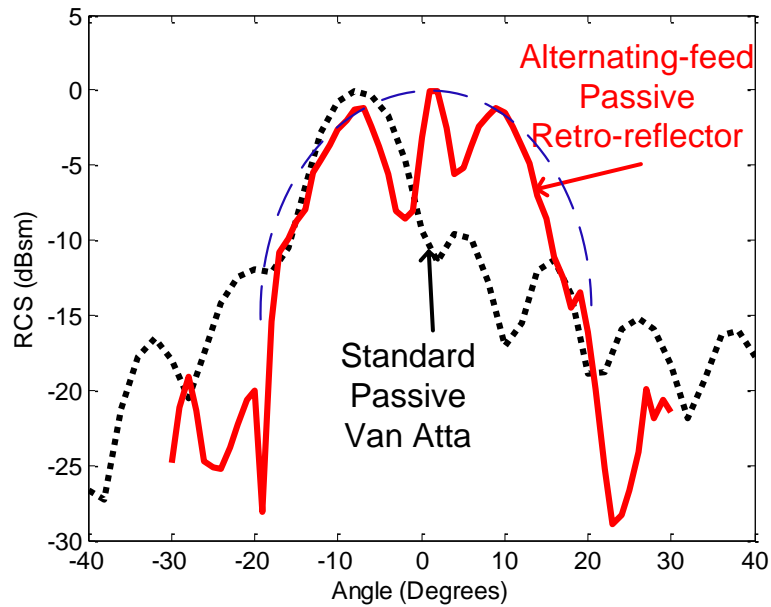


Figure 5.11: Vertical plane RCS pattern measurement comparing the standard and alternating-feed passive retro-reflective array.

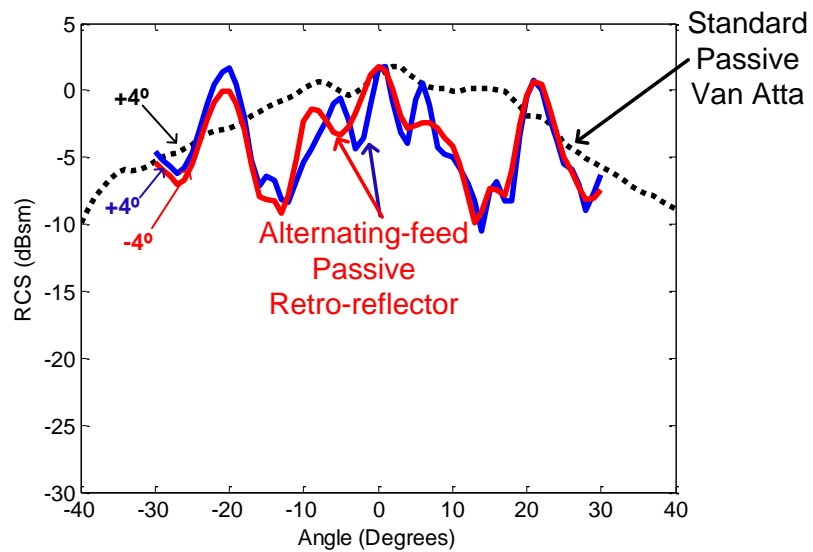
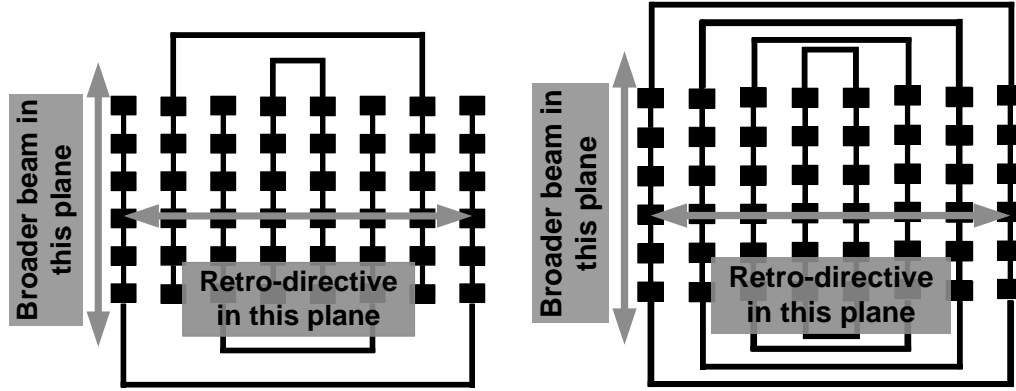


Figure 5.12: Horizontal plane RCS pattern measurement comparing standard and alternating-feed retro-reflective array. The response from the alternating-feed configuration remains consistent for a wide range of elevation angles.



(a) The alternating-feed interconnection scheme for linear series-feed radiating elements. (b) The closed-loop interconnection scheme for linear series-feed radiating elements.

Figure 5.13: Comparison of alternating and closed-loop feed network topologies for linear series-fed radiating elements. The closed-loop feed design will eliminate the sidelobes for the horizontal plane retro-reflective response.

5.3 Closed-Loop Feed Retro-reflective Array

5.3.1 Closed-Loop Feed Retro-reflective Array Introduction

As mentioned in Section 5.2.4, when the elements in an array are spaced at distances greater than one wavelength, the retro-reflective response is distorted. For applications desiring a broad and uniform horizontal plane RCS response in addition to broad vertical plane coverage, the alternating-feed architecture shown in Figure 5.13(a) cannot be used.

To remedy these shortcomings, a closed-loop feed network for the array elements is developed. In this configuration, all linear series array elements are fed from both the top and the bottom of the array as shown in Figure 5.13(b). The inter-element spacing of the linear array elements remains less than one wavelength thus eliminating the grating lobe. The operation of this array is similar to the alternating-feed, with the exception that in this closed-loop feed configuration, symmetry is maintained.

To achieve the feed configuration of Figure 5.13(b), the design of the retro-reflector elements themselves requires alteration. The load condition for the linear series array

is modified as a consequence of presence of the additional feed network lines. This closed-loop feed configuration also places an additional constraint on the feed network. The standard Van Atta condition still applies, i.e. the difference between the feed line lengths should be equal to multiples of a wavelength. Additionally, however, it is necessary to constrain the total path length around one loop of the array to also be a multiple of a wavelength. This is to ensure that radiation resulting from any residual energy after multiple loop traversals will add constructively to the overall RCS response.

5.3.2 Dual-Fed GCPW Linear Series Array Design and Measurements

To accomplish a dual (top and bottom) feeding arrangement for the linear series-feed array elements requires the development of a new linear series array. The target value for the squint that was established in Section 5.2.2 is maintained.

A photograph of the dual-fed linear series array is pictured in Figure 5.14 and its measured gain pattern is presented in Figure 5.15. To obtain accurate measurement values for the squint, much care is taken in the alignment of the linear arrays with respect to the alternate antenna. The far-field pattern of the array is acquired by feeding the lower port of each linear series array with the feed of the upper port terminated in a 50Ω load. This measurement is then repeated for the upper port with proper termination of the lower port. By examination of the intersection of the two curves, accurate determination of the squint of the individual linear series arrays is obtained.

5.3.3 Closed-Loop Feed Retro-reflective Array Measurements

Upon successful design of the dual-feed linear arrays, an entire passive closed-loop feed retro-reflective structure is fabricated as shown in Figure 5.16. This structure is the result of the integration of the dual feed linear series arrays with appropriate

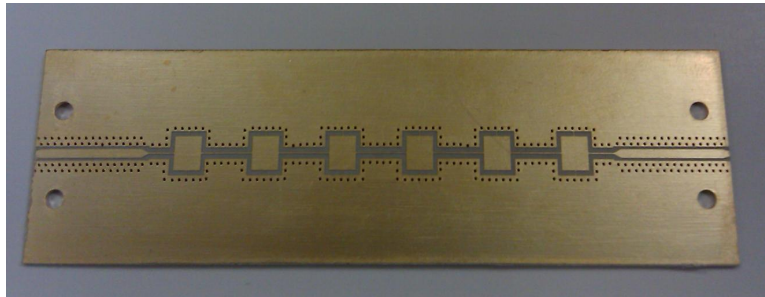


Figure 5.14: Photograph of the dual-feed linear series array element for the closed-loop feed retro-reflective array.

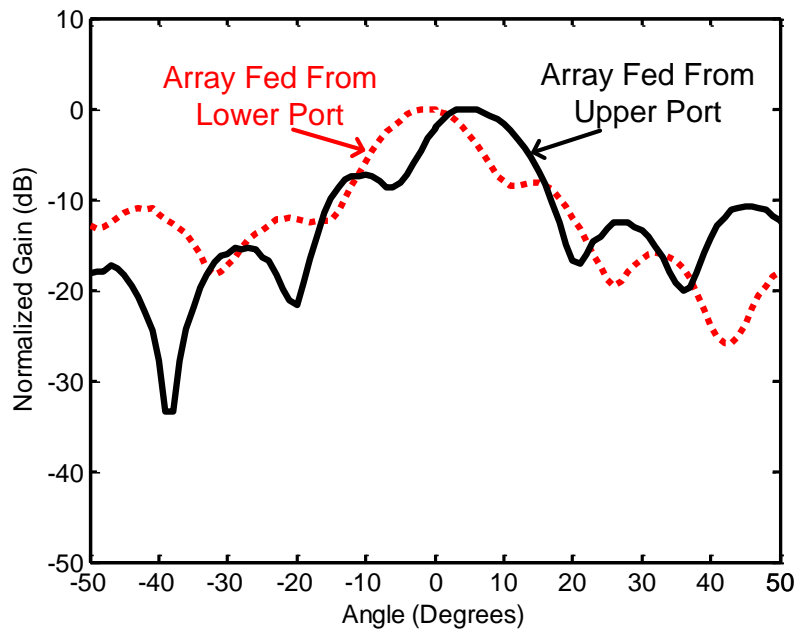


Figure 5.15: Gain pattern measurement of the dual-feed linear series array pictured in Figure 5.14.

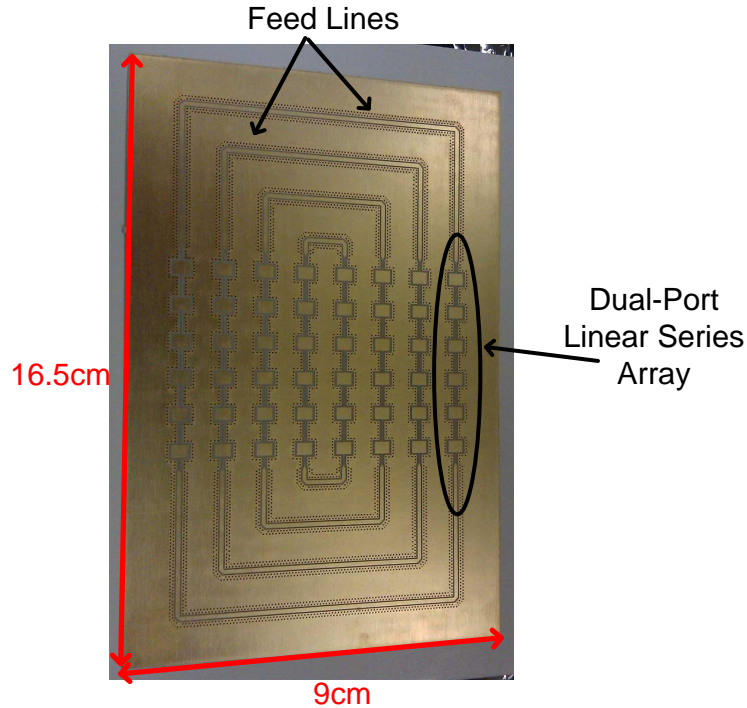


Figure 5.16: Photograph of the fabricated closed-loop feed retro-reflective array.

length feed lines for retro-reflective operation. The design of these feed network line lengths is modified by the new phase conditions associated with this architecture.

The retro-reflective array is again measured in the University of Michigan anechoic chamber using the network analyzer based radar system previously discussed. The return signal is collected at various azimuth and elevation angles and the method of substitution is used to determine the total RCS of this closed-loop feed retro-reflector configuration.

The vertical plane RCS pattern is shown in Figure 5.17 and compared to that obtained from the standard Van Atta array and the alternating-feed configuration. The vertical plane RCS pattern reveals a 300% broadened range of operational angles in this plane when compared to the standard Van Atta arrangement. The horizontal plane pattern, shown in Figure 5.18, is also compared to both the standard Van Atta configuration and the alternating-feed array. The high sidelobe levels that are the result of the Bragg modes of the alternating-feed array are no longer present in this

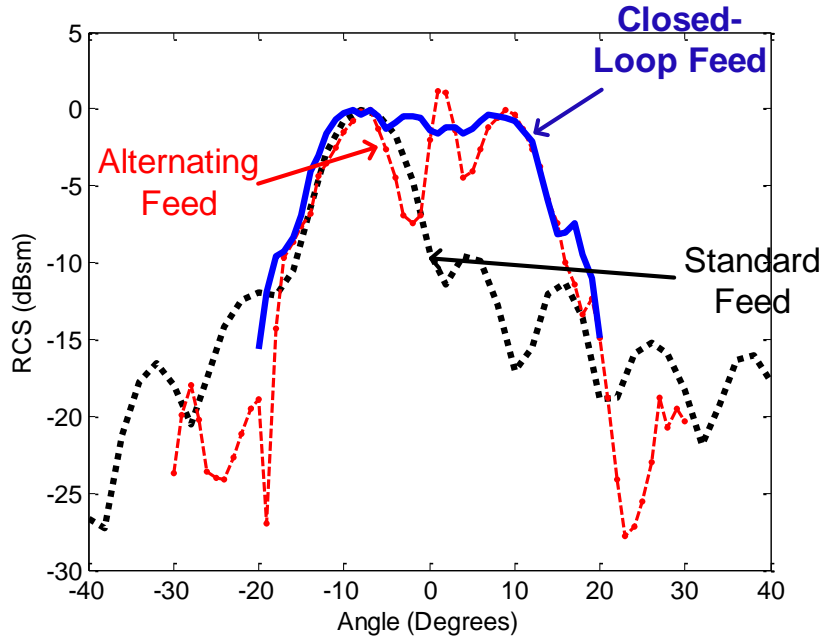


Figure 5.17: Normalized vertical plane RCS pattern measurement of the closed-loop feed retro-reflective array shown in Figure 5.16 compared to the standard and alternating feed configurations.

closed-loop feed configuration. The RCS response is broad as would be expected from a Van Atta retro-reflective array, limited by only the directivity of the radiating elements and the interconnecting feed network line lengths.

5.4 Conclusions

This chapter presents the design and fabrication of an entirely new breed of retro-reflective array feed architectures. These novel feed configurations utilize the phenomena of beam squint to broaden the incident elevation angle response of a high RCS retro-reflective array. Initially, the alternating-feed configuration is presented to broaden the elevation plane beam while reducing the size of the retro-reflective array. Operation of this structure along with vertical plane beam broadening is verified, but anomalies present in the horizontal plane pattern are undesirable for the intended application. As a solution, the closed-loop feed is developed. For this architecture,

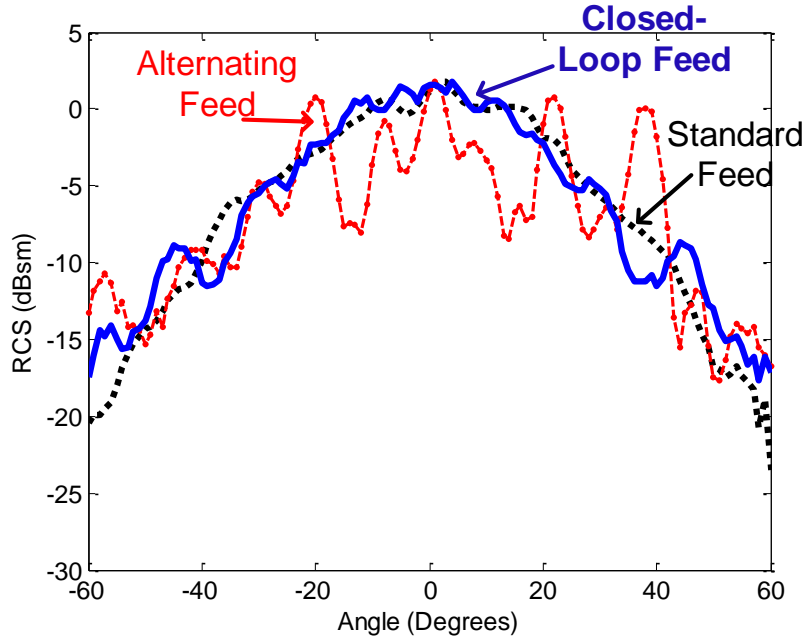


Figure 5.18: Normalized horizontal plane RCS pattern measurement of the closed-loop feed retro-reflective array shown in Figure 5.16 compared to the standard and alternating feed configurations.

the linear series array elements are fed from both the top and bottom of the array. The desired size reduction is no longer present for this array configuration but the performance of the overall array is enhanced by broadening the vertical plane beam without affecting the horizontal plane performance. The theory of operation of both these architectures is established and a model is developed to predict the behavior of the overall array. Measurements are collected for both architectures and compared with those obtained from the Passive High-RCS Van Atta array presented in Chapter III. The vertical plane beamwidths for these configurations are increased by $\sim 16^\circ$ which is a 300% improvement over the standard Van Atta configuration.

CHAPTER VI

Cross-polarized Retro-reflector Architecture

As previously mentioned, target distinction for retro-reflective arrays becomes problematic due to the presence of strong clutter backscatter contained in the scene. A final design concept to aid in the standoff detection and tracking of large metallic objects in a warehouse setting is presented in this chapter. While traditional methods to achieve enhanced detection generally involve an increase in gain of the target. The aim of this retro-reflector design is to minimize response of the clutter. A reduced size of the tag is achieved in this retro-reflector design by utilizing polarization properties to maintain or even enhance detection by maximizing the ratio of the target signal to that of the clutter. To accomplish this, a unique series fed dual polarized GCPW patch antenna is designed and implemented with minimal cross-coupling among elements. This compact array provides a requisite RCS while maintaining the desired retro-reflectivity. This method for enhanced detection is implemented at 26GHz allowing for a small footprint for both the retro-reflector and associated interrogating device. Design details and measurement results for this cross-polarized retro-reflective tag are presented.

6.1 Introduction

The majority of the methods to improve performance of planar retro-reflective arrays focus on RCS enhancement or a unique distinguishing modulation. An increase in the number of elements for the retro-reflector results in increased gain but at the expense of a larger footprint, complicated feed topologies and bandwidth reduction due to the increasing line lengths between elements. As presented in the Chapter III, large linear series arrays can be used to increase the number of elements without complication of the feed architecture, but this results in a drastically reduced beam in elevation. As presented in Chapter V, this elevation beam can be broadened by modifying the feed geometry of the linear arrays, but the large size of this array itself will remain an undesired consequence of this method of enhanced detection.

A broadened elevation beam can also be accomplished by employing two-dimensional Van Atta architecture but, as previously mentioned, its implementation restricts the number of elements that can be used. Large RCS cannot be achieved with this limited number of radiating elements and the number of elements cannot be increased without sacrificing bandwidth. Likewise, a two-dimensional retro-reflective structure is not well suited to enhance retro-reflective array performance for the application of interest.

Instead of increasing the number of array elements, the overall gain of the retro-reflective array can be increased by integrating amplifiers into the reflector delay paths. This comes at the cost of higher power consumption and increased complexity resulting from the incorporation of circulators to allow for two-way amplification. At 26GHz, surface-mount circulator devices exhibit significant loss and low isolation. The maximum amplifier gain that can be used in such a structure is limited by the isolation of these circulator devices, subsequently limiting the gain enhancement that can be achieved with this configuration. The combination of the circulator loss and limited amplification leads to negligible performance enhancement from such an

arrangement.

Enhanced detection of retro-reflective arrays can also be achieved by reducing the RCS of the clutter. Utilizing the polarization properties of the target array itself and the clutter, one can achieve enhanced detection without necessarily increasing the RCS of the retro-reflector. In general, depending on the polarizations of the retro-reflective antenna array elements and their associated interconnection scheme, the scattering matrix of the array structure can be varied. If the polarization response of the array differs, or be made almost orthogonal, from that of the clutter, upon comparison, this results in increased detectability of the target of interest.

Polarization refers to the temporal behavior of the E-field vector at a fixed point in space. A co-polarized (co-pol) response refers to a scenario where transmit and receive polarizations are identical where cross-polarized (cross-pol) refers to transmission and reception in orthogonal polarization planes. In general, most naturally occurring targets at high frequencies have a far stronger co-polarized response with minimal cross-polarized component. Cross-polarized return signals at high frequencies are generally the result of multiple scattering instances, generally an even number of bounces, and tend not to be the dominant form of backscatter. With the knowledge of these polarization properties of the scene of interest, the return contribution of the clutter will be minimized in a configuration where the desired signal is the cross-polarized component. This, in turn, leads to improved retro-reflective array performance.

Additionally, the patch elements in a cross-polarized configuration inherently provide the requisite isolation for the integration of amplifiers. For such a structure, circulators are no longer required and the amplifier integration issues previously noted are eliminated. Therefore, an even greater level of gain can be achieved by an identical or even reduced footprint.

In this chapter, the concept of dual-polarization is extended to a relatively large

retro-reflective array at a high frequency. The unique polarization properties of a dual polarized retro-reflective tag at 26GHz are first introduced and the details of the design and development of such an array are discussed. This structure is designed, simulated and fabricated in its passive form and its operation is confirmed. Additionally, a novel design concept that accomplishes both a unique tag identification sequence and enhanced detectability is introduced and implemented through the integration of amplifiers into the reflector delay paths. The development of this active counterpart is detailed and this chapter concludes with system validation measurements.

6.2 Polarization Synthesis for Enhanced Target Detection

Knowledge of the scattering matrix of a target allows for the calculation of its associated RCS for any set of transmit and receive polarization combinations. A polarization signature provides a graphical illustration relating the RCS of a specific target to the polarization of the incident and scattered fields. It is a plot of the backscattered power as a function of the orientation and ellipticity angle of the incident wave. As previously stated, at the frequency of interest, naturally occurring objects exhibit a dominantly co-polarized RCS response. At 26GHz, the wavelength is approximately 11.5mm and the radii of curvature for most objects in a man made setting are large with respect to this wavelength. Subsequently, they exhibit a negligible cross-polarized contribution. For manmade structures that do exhibit sharp edges as observed in building interior features, their orientation is generally along a Cartesian coordinate system and aligned with the principle polarization planes of the radar. This orientation will not contribute to the cross-polarized return signal. Likewise, the scattering mechanism from the additional clutter contained in the scene

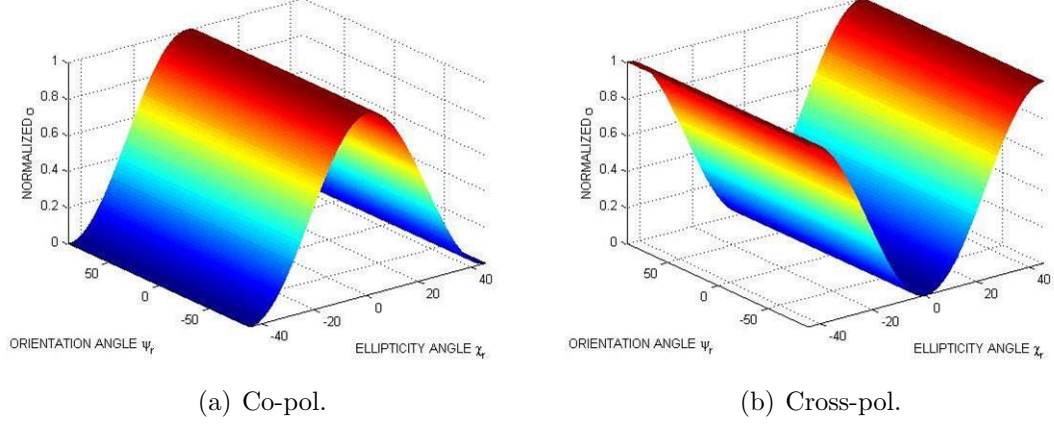


Figure 6.1: Polarization synthesis for naturally occurring targets.

is predominantly single bounce and their associated scattering matrix is similar to:

$$\bar{S} = \begin{pmatrix} S_{vv} & S_{vh} \\ S_{hv} & S_{hh} \end{pmatrix} \approx \begin{pmatrix} 1 & 0 \\ 0 & 1 \end{pmatrix} \quad (6.1)$$

For targets of this nature, the polarization response is very well defined and similar to that of a sphere as shown in Figure 6.1. The cross-polarized backscatter response to linear polarizations for such a target is minimized. That is, for transmission and reception in orthogonal polarizations, i.e., transmit horizontal polarization (H-pol) and receive vertical polarization (V-pol) and vice versa, the associated scattering matrix component is minimized. For enhanced detection, a retro-reflective tag is proposed exhibiting a scattering matrix similar to:

$$\bar{S} = \begin{pmatrix} S_{vv} & S_{vh} \\ S_{hv} & S_{hh} \end{pmatrix} \approx \begin{pmatrix} 0 & 1 \\ 1 & 0 \end{pmatrix} \quad (6.2)$$

The cross-polarized backscatter response for this target is maximized. The polarization signature for this general cross-polarized scattering matrix is depicted in Figure 6.2. Peaks are observed in the polarization synthesis response where nulls were present in Figure 6.1. The location of these peaks and nulls correspond to transmit

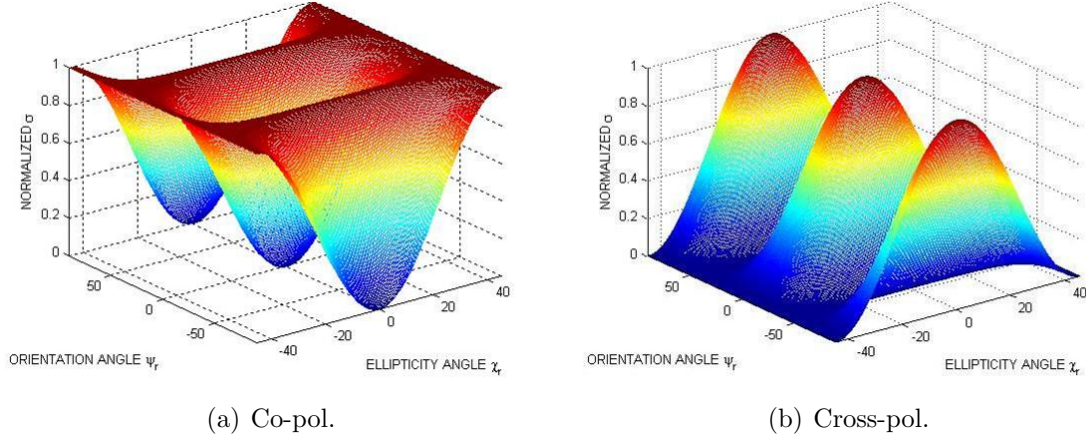


Figure 6.2: Polarization synthesis for proposed passive cross-polarized retro-reflective array.

and receive polarization combinations that maximize the ratio of target to clutter. An infinite number of transmit and receive polarization combinations exist, and further analysis can be performed for specific target and clutter scenarios to optimize this ratio. The result is enhanced target detection for a small retro-reflective array without the need for external amplification.

Additionally, reciprocity dictates that interchanging the incident and scattering directions and polarizations yields an identical response from a passive target. Specifically, the scattering matrices of all objects in the scene are symmetric ($S_{hv} = S_{vh}$) in the backscatter alignment notation [41]. Based on this principle, the integration of non-reciprocal active components, such as amplifiers, into the retro-reflective tag structure could further enhance distinction. The resulting active structure would exhibit a scattering matrix that does not adhere to reciprocity and is similar to:

$$\bar{S} = \begin{pmatrix} S_{vv} & S_{vh} \\ S_{hv} & S_{hh} \end{pmatrix} \approx \begin{pmatrix} 0 & 1 \\ 0 & 0 \end{pmatrix} \quad (6.3)$$

The operation of this structure is identical to the passive case, but the integration of the active elements completely eliminates one cross-polarization combination. By

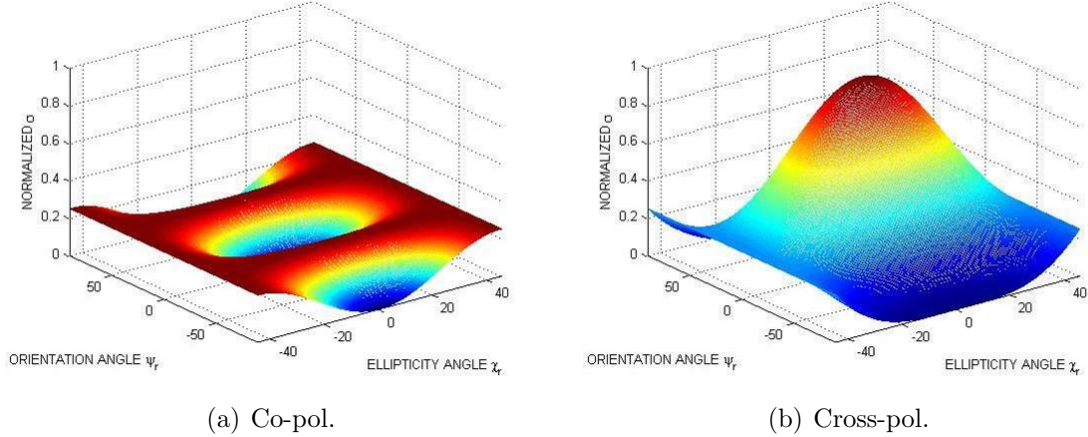


Figure 6.3: Polarization synthesis for proposed cross-polarized active retro-reflective array.

using a radar with polarization agility for the tag reader, the responses from two successive pulses of alternate orthogonal polarization combinations, HV and VH, can be subtracted from one another. This will eliminate all reciprocal clutter contained in the scene. Operation of such a system requires no a priori knowledge of properties of the scene, merely that the environment is passive in nature.

Figure 6.3 illustrates the polarization signature for this non-reciprocal retro-reflective array. This can be compared to the signatures in Figure 6.1 and Figure 6.2, noting the shift of peaks and nulls for the various targets at identical transmit and receive polarization combinations.

Additionally, the invariance of the tag response upon rotation with respect to the principle polarization directions should be noted. From a practical point of view, it is important that the detection be robust to small variations of the tag orientation with respect to the radar polarization coordinates. Figure 6.4 shows the orientation of the tag coordinates (V' , H') with respect to that of the radar (V , H) after rotation by an angle ψ .

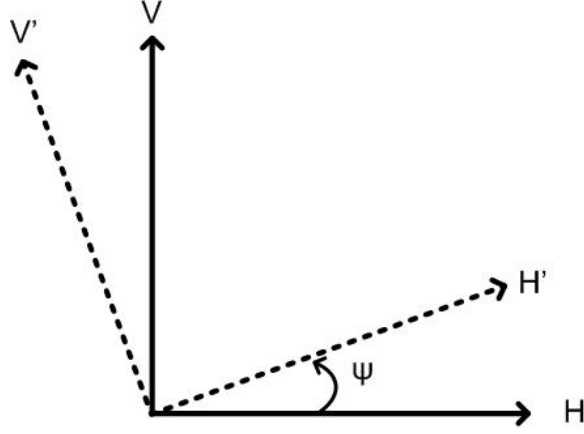


Figure 6.4: Coordinate system denoting initial (unprimed) and rotated (primed) orientation of the retro-reflective array tag.

For a general scattering matrix, upon rotation:

$$\bar{S} = \bar{T} S' \bar{T}^{-1} = \begin{bmatrix} \cos\psi & \sin\psi \\ -\sin\psi & \cos\psi \end{bmatrix} \begin{bmatrix} A & B \\ C & D \end{bmatrix} \begin{bmatrix} \cos\psi & -\sin\psi \\ \sin\psi & \cos\psi \end{bmatrix} \quad (6.4)$$

This results in a general rotated scattering matrix of:

$$\bar{S} = \begin{bmatrix} X_x(A X_x + C X_y) + \dots & -X_y(A X_x + C X_y) + \dots \\ X_y(B X_x + D X_y) & X_x(B X_x + D X_y) \\ -X_x(A X_y - C X_x) - \dots & X_y(A X_y - C X_x) - \dots \\ X_y(B X_y - D X_x) & X_x(B X_y - D X_x) \end{bmatrix} \quad (6.5)$$

where:

$$X_x = \cos\psi \quad (6.6)$$

$$X_y = \sin\psi \quad (6.7)$$

Investigation of the difference in the cross-polarized components of this rotated

scattering matrix, namely $S_{HV} - S_{VH}$ results in:

$$\begin{aligned}
S_{HV} - S_{VH} &= -X_y(AX_x + CX_y) + X_x(BX_x + DX_y) \\
&\quad + X_x(AX_y - CX_x) + X_y(BX_y - DX_x) \\
&= B - C
\end{aligned} \tag{6.8}$$

independent of orientation angle.

For a reciprocal target, $B = C$, and the difference in the cross-polarized scattering matrix components obviously vanishes.

Therefore, even upon rotation, the reciprocal nature of the clutter will still adhere to reciprocity and $S_{HV} - S_{VH} = 0$. This is not the case for a nonreciprocal target where $B \neq C$. In this case, such as the active cross-polarized tag that will be discussed later in this chapter, $S_{HV} - S_{VH}$ will not vanish. Hence if this response, which is independent of tag orientation, is used as a detection parameter, the clutter will be entirely removed.

6.3 Passive Cross-Polarized Retro-reflective Array

6.3.1 Design Overview

The traditional Van Atta retro-reflector concept can be modified to provide cross-polarized response by substituting the co-polarized elements in Figure 1.6 with cross-polarized elements as illustrated in Figure 6.5. These dual polarized elements are interconnected depending on their absolute distance from the array center with lines of equivalent phase length, much like a standard Van Atta array. The exception for this structure is that each polarization port of the antenna element is connected to the orthogonal polarization port of its partner antenna. Hence, the polarization of the reradiated response will be orthogonal to the received signal. Additionally, the

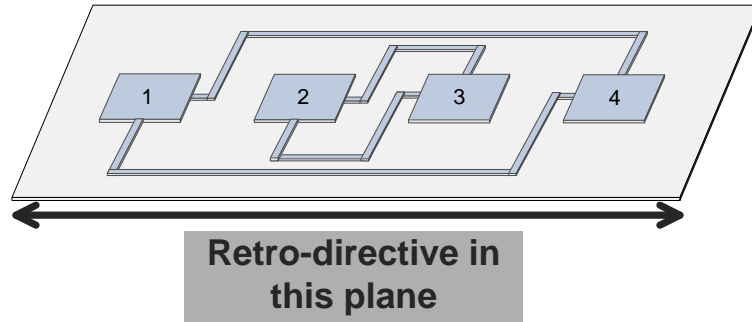


Figure 6.5: Dual-polarized radiating elements are integrated into the traditional Van Atta architecture of Figure 1.6 to yield a cross-polarized retro-reflective array.

phase relationships must be maintained for this structure on transmit and receive for all polarization combinations. This places restrictions on the layout of the antenna elements and feed network.

Operation of the array is identical to that illustrated in Figure 1.6, but for this structure, the signal incident on the array can be of two orthogonal polarizations. For each polarization, the incident signal is collected by the array, propagates through the feed network lines of appropriate phase delay, and is retransmitted in the alternate polarization. This arrangement maximizes the cross-polarized response of the target. Retro-reflective operation is achieved in the horizontal plane of this structure as indicated in Figure 6.5.

To achieve the requisite gain from this structure, the individual radiating elements are linearly combined in series as illustrated in Figure 6.6. This unique cross-polarized structure inherently minimizes the feed network length by reducing losses through radiation and dissipation. Using these constituent arrays also uses the minimum number of active components, thus increasing the RCS of the overall structure by reducing their associated losses.

The details of the design of the radiating elements and overall passive cross-polarized array structure will be detailed in the following sections.

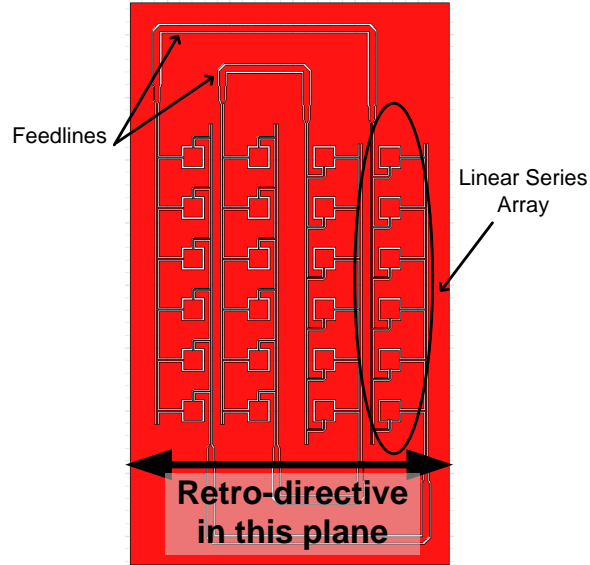


Figure 6.6: Appropriate length feed lines are integrated with dual-polarized linear series array elements to increase the RCS of a cross-polarized retro-reflective array.

6.3.2 Passive Cross-polarized Retro-reflective Array Design and Simulation

For this cross-polarized design, the choice of radiating element is especially important to the overall operation of this retro-reflective structure. It ultimately determines the performance in terms of angular coverage through directivity, the polarization response and the collective RCS. To achieve the requisite bandwidths while minimizing losses, GCPW patch elements are used in the design of the dual-polarized planar retro-reflective array. These individual coplanar patch elements consist of a patch antenna closely surrounded by a ground plane and fed with a GCPW line, as illustrated in Figure 6.7 [34]. While these elements are similar in geometric configuration to a loop slot antenna, they behave entirely like a microstrip patch antenna whose well defined properties are utilized for the design of the dual-polarized GCPW patch antenna.

The general microstrip patch is designed to operate in two orthogonal modes, TM₁₀ and TM₀₁. For a square patch element, these modes are degenerate and

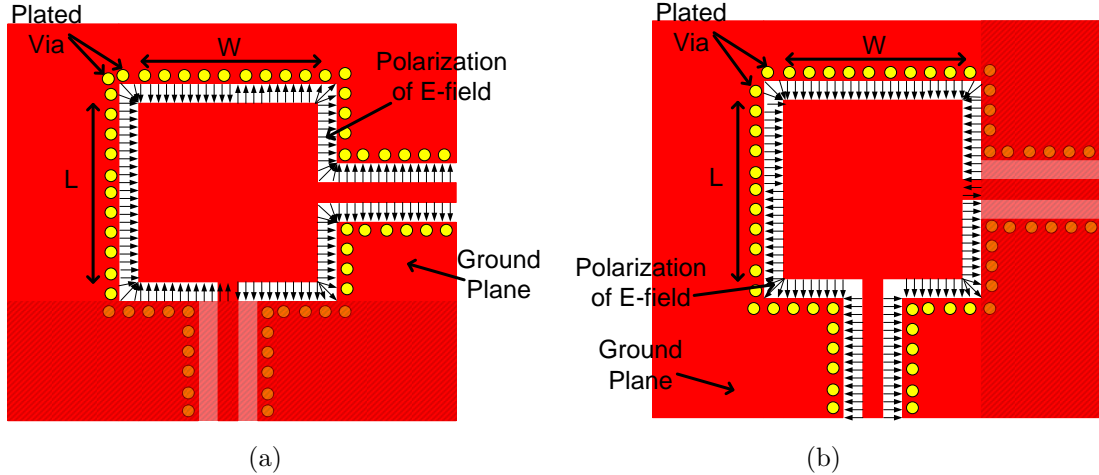


Figure 6.7: Field distributions for a dual-polarized GCPW patch antenna for two orthogonal polarizations.

resonate at an identical frequency. Isolation between two orthogonal polarization modes ensures little interference between transmitted and received signals. While corner fed square patches do exhibit isolation in excess of 10dB greater than their edge fed counterparts [42], both impedance matching and feed network routing becomes more troublesome for a large planar structure in this configuration. For this reason, two port square GCPW patch antennas are used as the radiating elements for this design. Feeding the patches at the centers of the orthogonal sides provides minimum intra-port coupling [43]. Figure 6.7 illustrates the polarization of the E-field for each orthogonal polarization for the dual-polarized GCPW patch antenna.

For the development of the dual polarized linear series array, a single element is first designed using patch design principles and then verified using fullwave electromagnetic field simulation tools (HFSS). The substrate employed for this design is 20mil thick Rogers Corporation RT/duroid 6002. In order to achieve 50Ω input impedance for this six-element linear series array, the input impedance of each resonator is designed to be $Z = 300 + j0\Omega$ at 26GHz.

The individual radiating elements are designed to achieve the requisite 1GHz bandwidth at 26GHz while maintaining isolation between orthogonal ports as shown

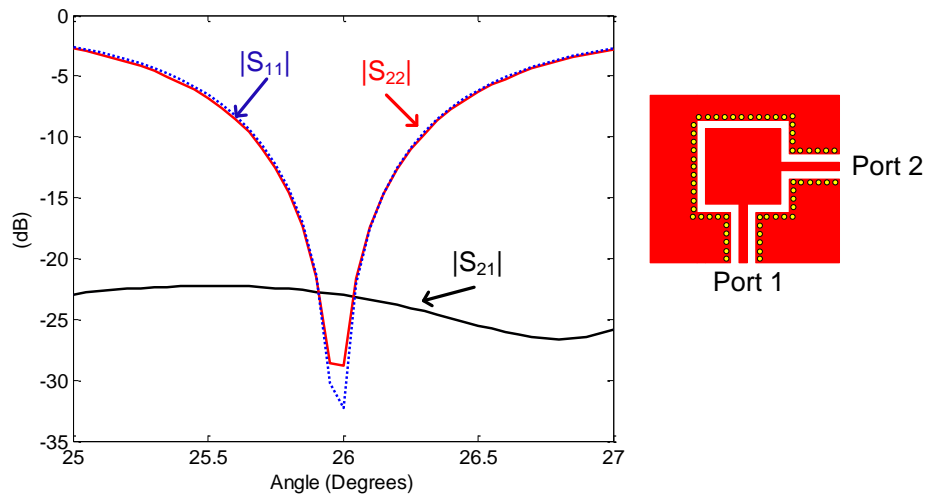
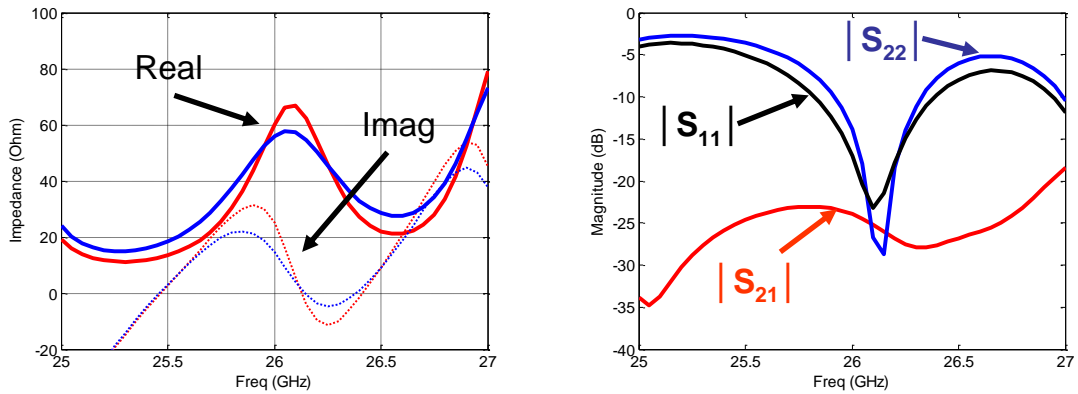


Figure 6.8: Simulated transmission and reflection coefficients for a single GCPW dual-polarized patch antenna element. Isolation values greater than 22dB are obtained over the frequency band of interest.

in Figure 6.8.

These dual-polarized radiating elements are then combined into a six element linear series array with interconnecting line lengths chosen to provide the appropriate phase delay for uniform phase excitation along the linear array. To help facilitate this proper phase excitation, a quarter-wavelength short circuited stub is added to the terminal end of the feed line for each polarization. This linear array structure is simulated in Ansoft HFSS and its simulated input impedance and reflection and transmission coefficients are displayed in Figure 6.9. Isolation is maintained between the two orthogonal feeds and the reflection coefficient reveals operation for the entire band of interest (25.5-26.5GHz) and is nearly identical among the two orthogonal feeds. The gain of the six element dual polarized linear series array is displayed in Figure 6.10 for the center frequency and at the edges of the band of operation. For this structure a 5° squint is noted at the low and high ends of the operational band. This is the result of frequency dependence of the propagation delay for the internal feeding geometry and, while not desirable, it is important that it remains constant among orthogonal polarizations for proper retro-reflector operation.



(a) Simulated input impedance for the 6x1 dual-polarized linear series array (b) Simulated transmission and reflection coefficients for the 6x1 dual-polarized linear series array

Figure 6.9: Simulated input impedance, transmission and reflection coefficients for the six element dual-polarized linear series array.

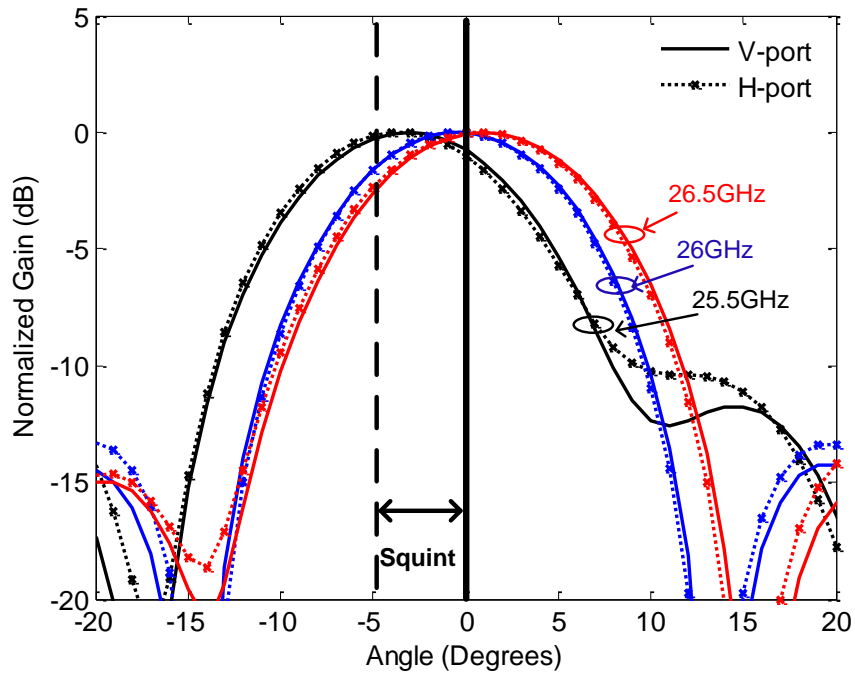


Figure 6.10: Simulated normalized gain pattern for the 6x1 dual-polarized linear series array.

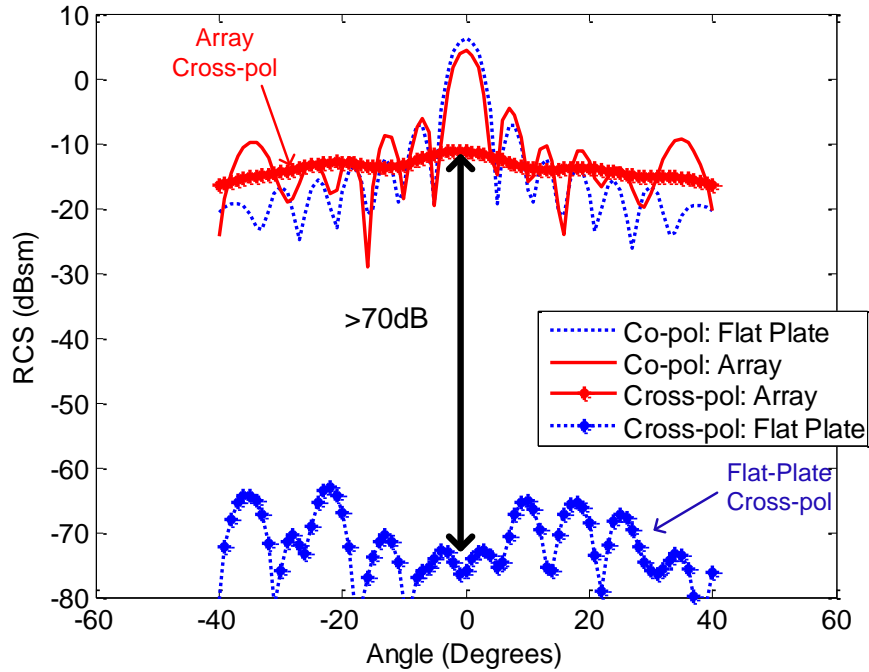


Figure 6.11: Simulated monostatic RCS for the 4X6 element cross-polarized retro-reflective array pictured in Figure 6.6 compared to that of an identically sized flat plate.

The appropriate length feed network lines are then integrated with these dual-polarized six-element linear series arrays to form the entire cross-polarized retro-reflective array as pictured in Figure 6.6. The full wave monostatic RCS response is simulated using HFSS and compared to that of an identically sized flat metallic plate. The results are shown in Figure 6.11. The co-polarized response generated by this structure is very similar to that of an identically sized flat plate, as the array was not designed to operate in this polarization configuration. The cross-polarized response generated by this structure far exceeds that of the identically sized flat plate. Additionally, a broad RCS response is observed in the horizontal plane of this structure, demonstrating the retro-reflective capabilities of this cross-polarized retro-reflective array structure. The cross-polarized response generated by this structure exceeds that of the identically sized flat plate by approximately 70dB.

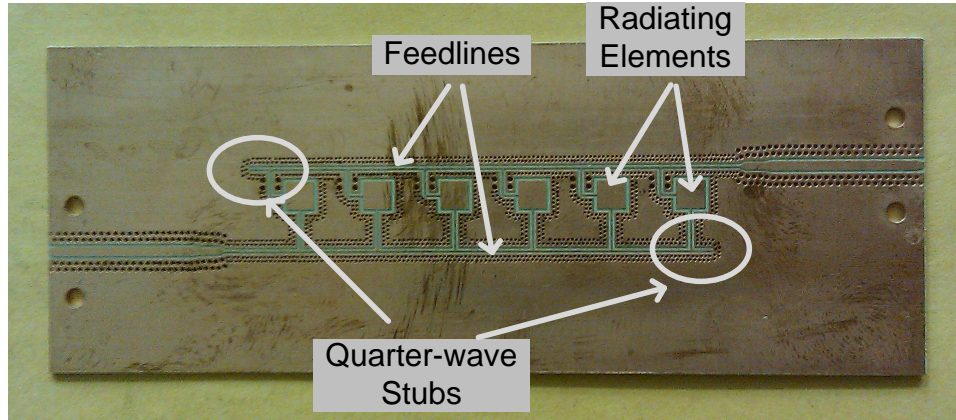
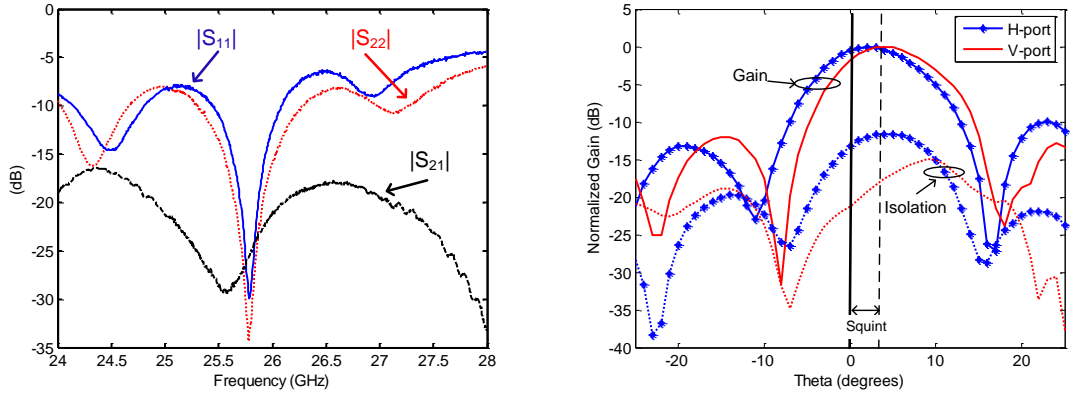


Figure 6.12: Photograph of the fabricated six-element dual-polarized linear series array.

6.3.3 Passive Cross-polarized Retro-reflective Array Measurements

The S-parameters of the fabricated cross-polarized linear arrays, pictured in Figure 6.12, are measured in the laboratory using a network analyzer. Inspection of Figure 6.13(a) reveals the reflection coefficient is maintained between the two orthogonal ports along with acceptable levels of isolation. The far-field gain pattern of the linear array is collected at the University of Michigan anechoic chamber by feeding each port of the linear array in its associated plane and collecting the far-field pattern in the identical plane, with the orthogonal array port terminated in a 50Ω load. To measure the isolation in the far-field, the pattern is collected with the polarization of the receiving antenna orthogonal to that of the linear series array. Figure 6.13(b) demonstrates isolation in excess of 15dB between the two orthogonal ports of this linear series array. Additionally, a 5° squint is observed among the two orthogonal polarization ports of the linear series array. This variation from the predicted squint value of 2° can be attributed to the presence of the vias and, while this squint is not ideal, it is only functionally important that it remain consistent among the polarization ports of the linear array.

Appropriate length feed network lines are combined with these dual-polarized linear series arrays to form the entire fabricated array pictured in Figure 6.14. The



(a) Measured S-parameters for the 6X1 linear cross polarized array shown in Figure 6.12. (b) Measured gain pattern of the dual-polarized linear series array shown in Figure 6.12.

Figure 6.13: Measured S-parameters and gain for the six-element dual polarized linear series array.

far-field monostatic RCS response of this structure is collected in the laboratory setting using the network analyzer based radar system. A 2 inch metallic sphere is again used as the calibration target and a signal to noise ratio in excess of 20dB was observed in the measurement. The measured RCS patterns are displayed in Figure 6.15 and compared to the measurement of an identically sized flat plate. The lack of dependence on azimuthal angle for the cross-polarized retro-reflective array response for this fabricated structure demonstrates its retro-reflective capabilities. The cross-polarized return is approximately 25dB greater than that of the flat plate. For this measurement, the cross polarized response of the flat plate is at the noise floor of the measurement system. Additionally, only 30dB of isolation is noted in the measurement system itself, accounting for the peak in the cross-pol response of the flat plate near boresight.

6.3.4 Passive Cross-polarized Retro-reflective Array Performance in High-Clutter Environment

This passive cross-polarized retro-reflective array is measured in a highly cluttered natural environment. An assortment of targets are placed in the vicinity of the pas-

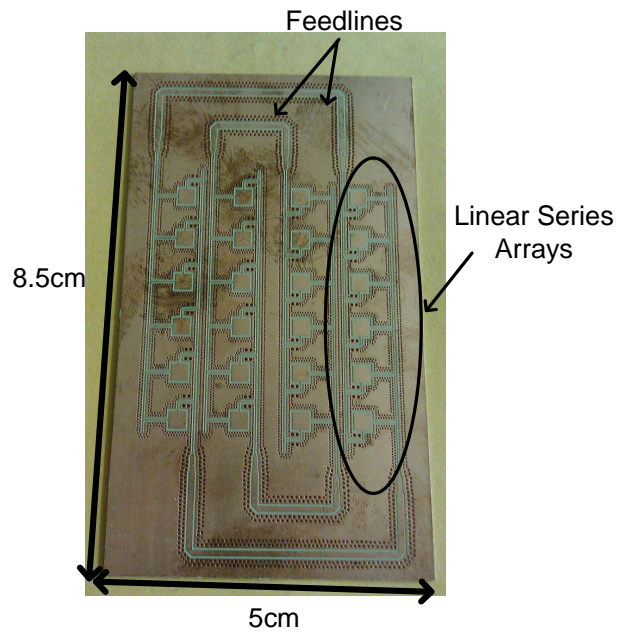


Figure 6.14: Photograph of fabricated cross-polarized retro-reflective array.

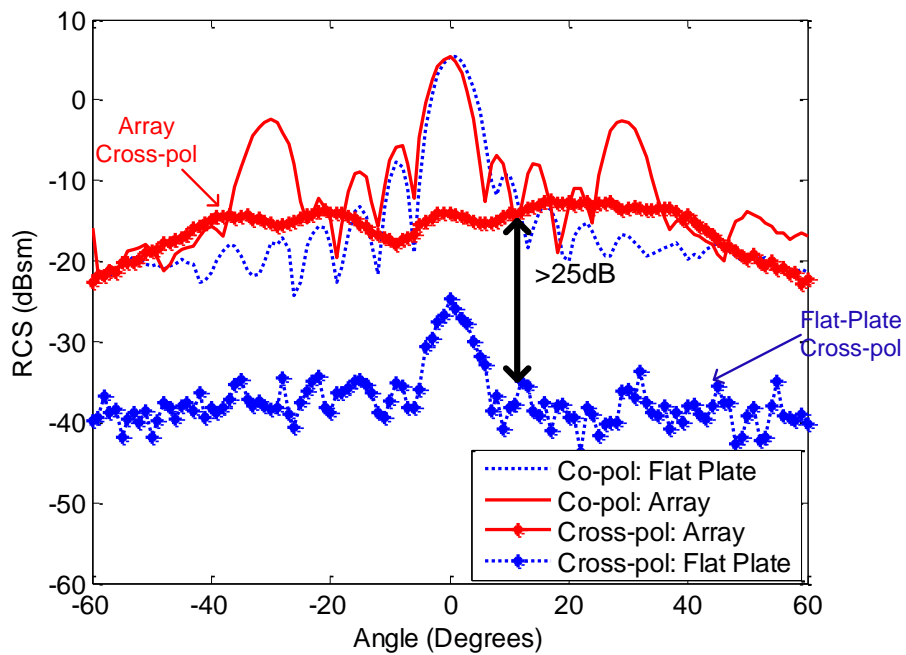


Figure 6.15: Measured monostatic RCS pattern from cross-polarized retro-reflective array shown in Figure 6.14 compared to that of an identically sized flat plate.

sive retro-reflective tag including a moderately sized metallic cylinder to mimic the large metallic cylinder presented in the potential application scenario. This clutter arrangement is pictured in Figure 6.16. The co-polarized and cross-polarized return signals are collected with and without the passive cross-polarized retro-reflective tag using a network analyzer based radar system. These results are compared in Figure 6.17. The overall clutter contribution is reduced when the radar is in the cross-pol arrangement as seen by comparing the absolute levels of Figure 6.17(a) and Figure 6.17(b). This validates the previous discussion presented in Section 6.1 regarding the polarization dependence of clutter RCS. The presence of the retro-reflective tag has little impact on the overall return signal for the co-polarized response as observed in Figure 6.17(a). This is in contrast to the cross-polarized arrangement, pictured in Figure 6.17(b), where a large increase in RCS is noted when the passive cross-polarized retro-reflective array is included in the scene. Additionally, the passive cross-polarized retro-reflective tag is observed to be a dominant contributor to cross-polarized backscatter.

6.4 Active Cross-polarized Retro-reflective Array

6.4.1 Modulation Overview

Amplitude modulation is implemented in this cross-polarized retro-reflective array through the integration of active elements in the reflector delay paths as depicted in Figure 6.18. This allows for each tag to be coded with a unique identification sequence that allows the radar to uniquely identify the tag under interrogation in addition to the knowledge of its location. The use of amplifiers as the active elements in this array architecture provides the additional benefit of creating a completely unique and non-reciprocal polarization signature by eliminating one cross-polarization combination. In conjunction with a radar that is polarization agile, pulse to pulse

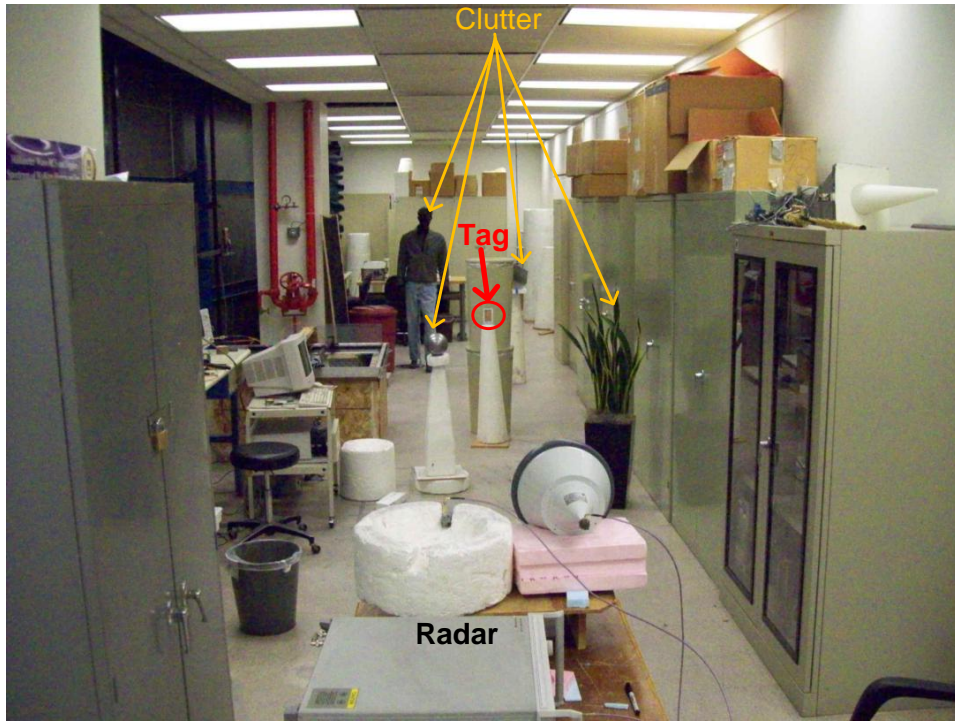


Figure 6.16: Photograph of the passive cross-polarized retro-reflective array in a highly cluttered environment.

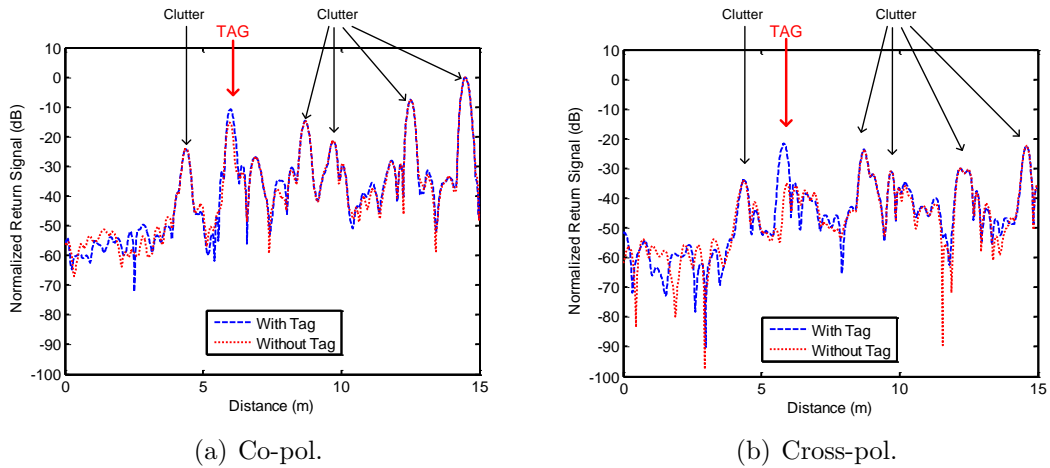


Figure 6.17: Comparison of the co-polarized and cross-polarized return signals from a highly cluttered environment pictured in Figure 6.16. The presence of the passive cross-polarized retro-reflective tag is noted in the cross-polarized arrangement.

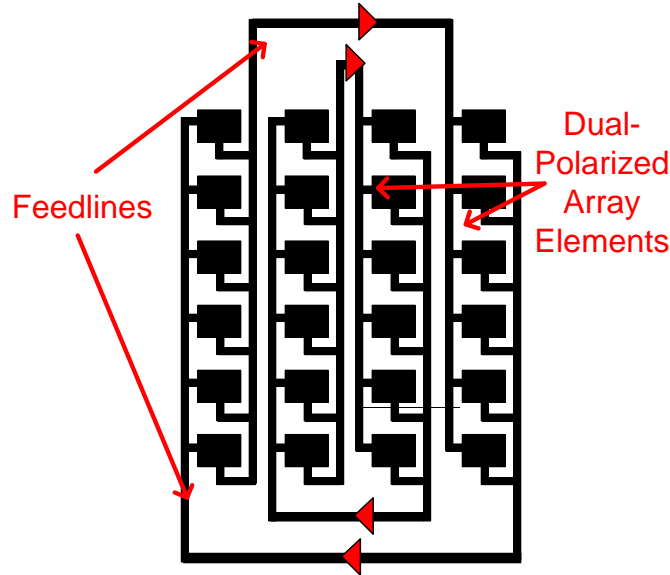


Figure 6.18: Sketch illustrating the integration of active components into the dual-polarized retro-reflective array. This will completely eliminate one polarization combination.

subtraction is implemented as discussed in Section 4.7, with the modification that pulses of orthogonal polarization combinations are subtracted from one another for this cross-polarized arrangement. This not only removes the contributions of all time-stationary clutter, but completely eliminates all non-reciprocal clutter contributions from the scene due to the reciprocal nature of passive targets.

6.4.2 Active Cross-polarized Retro-reflector Design and Measurements

Silicon Radar’s LNA 024 03 amplifier is chosen as the non-reciprocal component for integration into the passive cross-polarized retro-reflective array of Figure 6.18. This LNA exhibits adequate performance characteristics in the desired band of operation with both low power consumption and high gain. More information regarding its operation can be found in [44]. A photograph of an example feed network line with the amplifier and associated bias is pictured in Figure 6.19.

The amplifier draws 5mA of current with 2.5V of applied voltage. While on chip the gain is reported at 15dB, in practice, with the losses associated with the bias

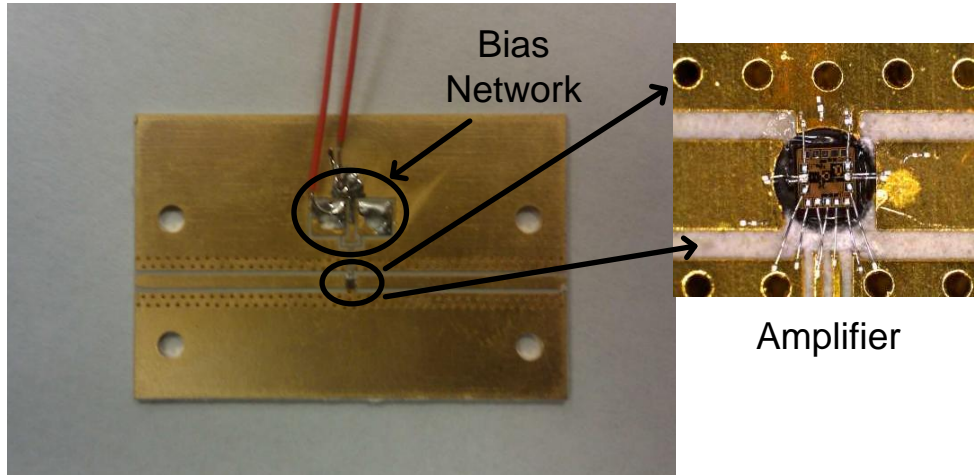


Figure 6.19: Photograph of feed network line with amplifier and requisite DC supply.

and circuit integration, the realizable gain of each amplifier is closer to 6dB for this preliminary design.

The feed network design is adjusted to allow for the integration of the amplifier circuits for the development of the active cross-polarized retro-reflective array as pictured in Figure 6.20. To achieve optimal gain from this device at this high frequency of operation, the connection of the amplifier to the circuit board was an imperative design consideration. To minimize losses, each amplifier is placed inside a specially drilled hole in the retro-reflective array feed line. This allows the minimization of the length of the wire bond lines. Additionally, two wire bonds are used to connect the amplifier to the signal line to facilitate a strong connection. The amplifiers are controlled in series and biased in either the on or off position. RCS variation with angle along with the change in RCS from on to off states is used to quantify the performance of this active array.

The RCS pattern of this active retro-reflective array is again collected in the University of Michigan anechoic chamber and the response is displayed in Figure 6.21. A relatively high RCS is observed in the on state and it shows a general lack of dependence on azimuthal angle typical of a retro-reflective array. The peaks and nulls in this response can be attributed to reflections arising from the amplifiers and their

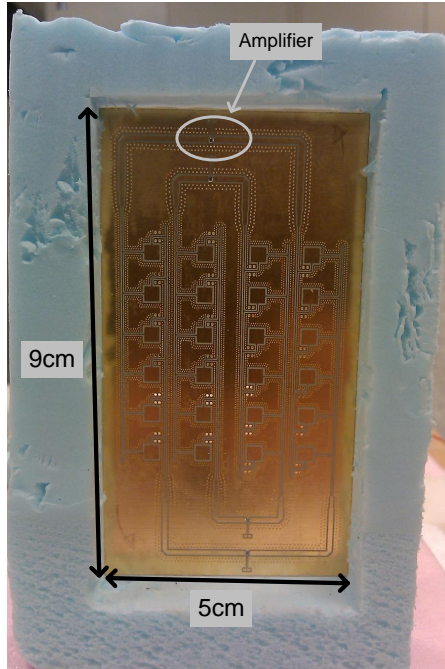


Figure 6.20: Photograph of active cross-polarized retro-reflective array with amplifiers and bias.

associated bias circuitry along with imperfections in the laboratory test setup. For this configuration, the power is delivered to the active array using an external power supply which interfered with the stability of the measurement. This is additionally compared to the passive array and the gain of approximately 6dB can be observed. Additionally, the RCS pattern of this active cross-polarized retro-reflective array is collected with the amplifiers in their off states and a variation in excess of 8dB is noted when compared to the on performance of the array.

6.4.3 Active Tag and Radar System Measurements

This active cross-polarized retro-reflective is then tested in a more naturally occurring environment as pictured in Figure 6.22. This highly cluttered scene includes two metallic cylinders to mimic the intended environment for this retro-reflective array.

The gated time domain response of the active cross-polarized retro-reflective array is collected in both its on and off states using a polarization-agile network analyzer-

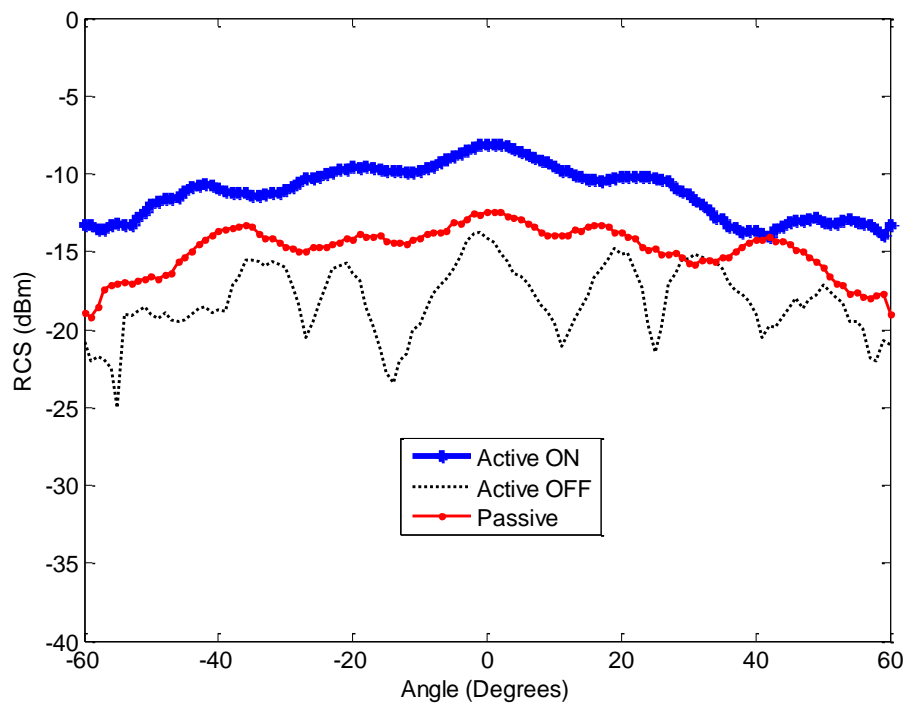


Figure 6.21: RCS pattern of the active cross-polarized retro-reflective array comparing on and off states and the passive cross-polarized retro-reflective array.

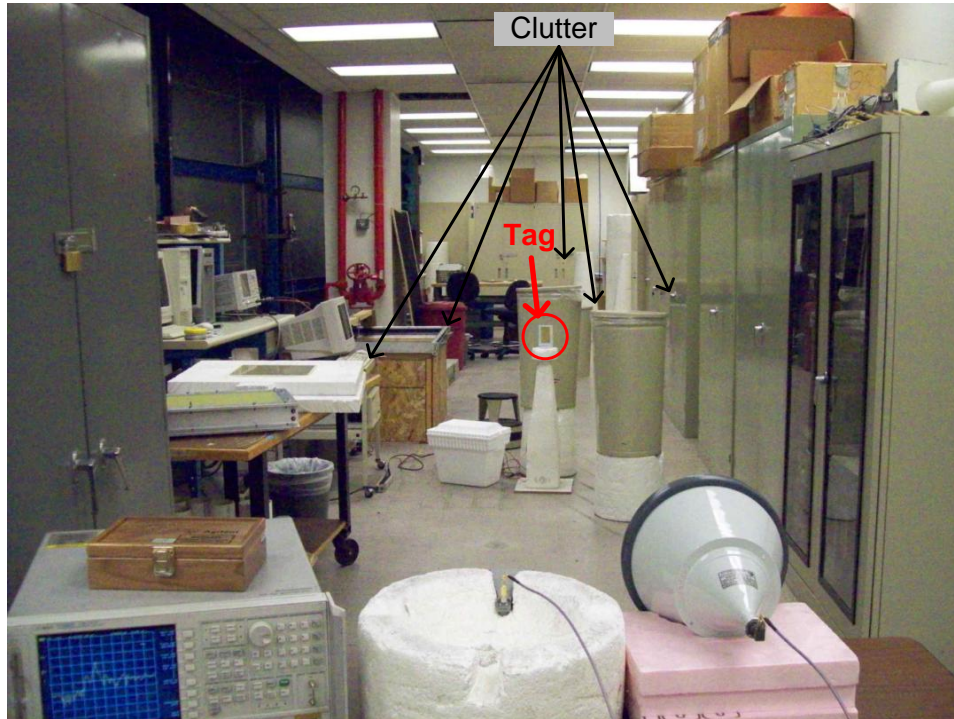
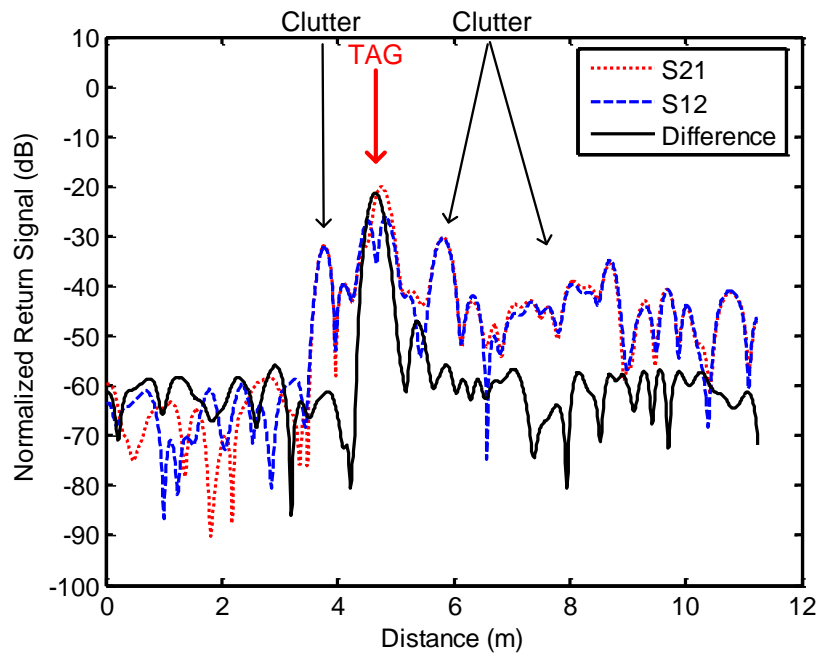


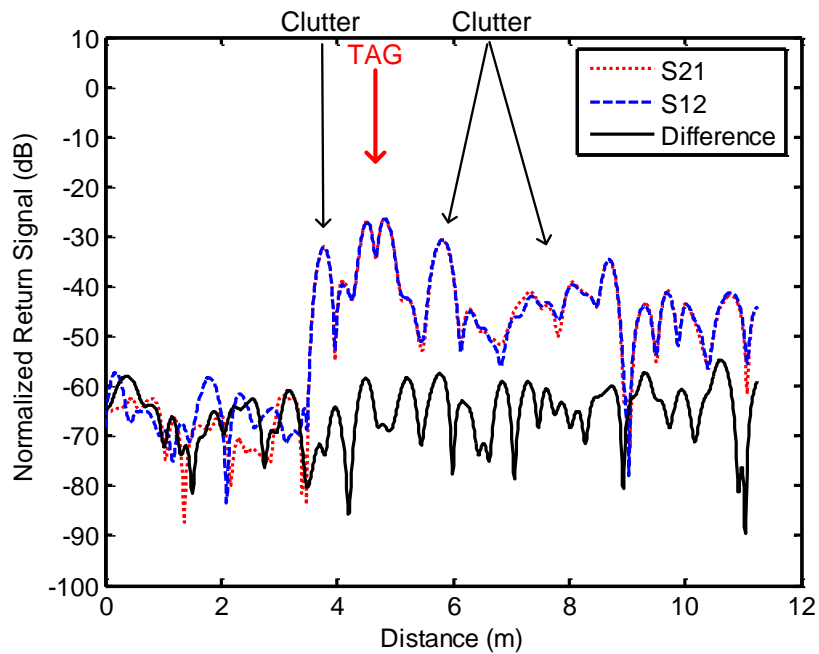
Figure 6.22: Photograph of the active cross-polarized retro-reflective array in a highly cluttered environment.

based radar system. The response is collected for VH and HV (S_{12} and S_{21} respectively) along with the difference between these two values ($S_{12}-S_{21}$) and are compared in Figure 6.23. Proper intra-port calibration is required for the network analyzer to eliminate the inherent variations among the measurement system itself. Examination of Figure 6.23 reveals that the subtraction of these two quantities eliminates all extraneous non-reciprocal clutter contributions from the scene leaving only the response of the retro-reflective tag. Additionally, the RCS variation between the on and off states noted for this active tag will be utilized for the eventual modulation of the retro-reflected signal.

For completeness, this measurement is also conducted with the transmitting and receiving antennas arranged in a co-polarized configuration. The time domain response over the band of interest is collected for both the retro-reflective array in the on and off states and compared in Figure 6.24. Subtraction of S_{12} and S_{21} no



(a) Array on.



(b) Array off.

Figure 6.23: Cross-polarized return from the active retro-reflective array in both on and off states measured in the highly cluttered laboratory scene shown in Figure 6.22. The subtraction of S12 and S21 reveals the reciprocal nature of the cluttered environment.

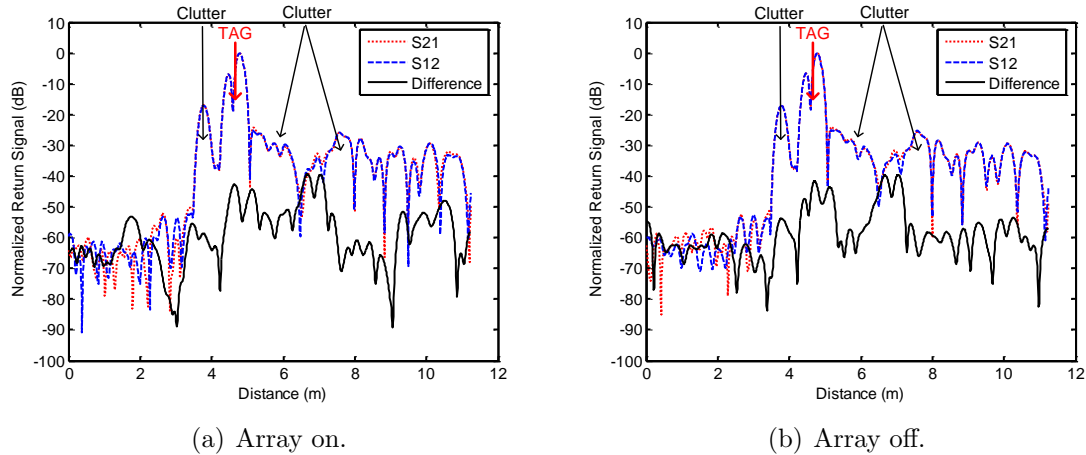


Figure 6.24: Co-polarized return from the active retro-reflective array in both on and off states measured in the highly cluttered laboratory scene shown in Figure 6.22. The subtraction of S12 and S21 reveals nothing meaningful.

longer yields a meaningful difference signal. Additionally, a larger overall RCS is observed for the clutter in this co-polarized arrangement by comparing absolute levels of Figure 6.24 to that of Figure 6.23.

6.4.4 Background Subtraction for Enhanced Target Distinction

To test the validity of this method for enhanced detection, the measurement is repeated in a more naturally occurring environment. A mock radar is positioned on a turntable and a 180° scan of the laboratory environment is conducted. Dual orthogonal polarization combinations are collected simultaneously from the radar for both the co-polarized and cross-polarized arrangement of transmitting and receiving antennas. The orthogonality of the radar antennas is carefully controlled. For a co-polarized arrangement, a target with a known and invariant co-pol response, such as a sphere, is placed in the scene. The polarization of one of the antenna arrays is then rotated to maximize the response of this target. This confirms a co-pol arrangement and the measurement is subsequently conducted. Alternatively, to achieve a cross-pol arrangement for the radar antennas, the response of this target is carefully minimized.

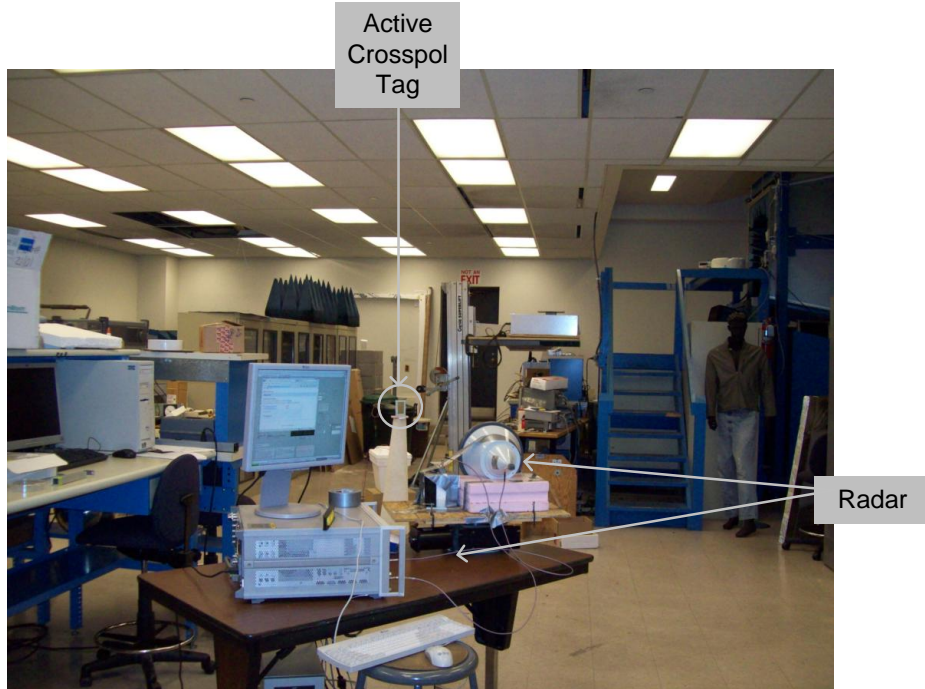


Figure 6.25: Photograph of the radar and active cross-polarized tag in highly cluttered laboratory scene.

Figure 6.25 is a photograph of the scene. The radar and active tag are positioned as indicated in the photograph and a scan is taken from -90° to $+90^\circ$. Various sources of naturally occurring clutter exist in the scene including a large array of file cabinets, near boresight, and a computer and lab bench around -90° .

Figure 6.26 compares the co-polarized return signal to that of the cross-polarized return signal. The overall cross-polarized contribution of the clutter is 17dB less than the co-pol response. This is additionally indicated by the much brighter spots of the co-pol response when compared to the cross-pol response of Figure 6.26(b).

The subtraction of S_{21} and S_{12} is also compared for this cluttered scene for both the co-polarized and cross-polarized arrangement of the transmitting and receiving arrays in Figure 6.27. The strong response of the active cross-polarized retro-reflective array is noted in the cross-polarized arrangement in Figure 6.27(b).

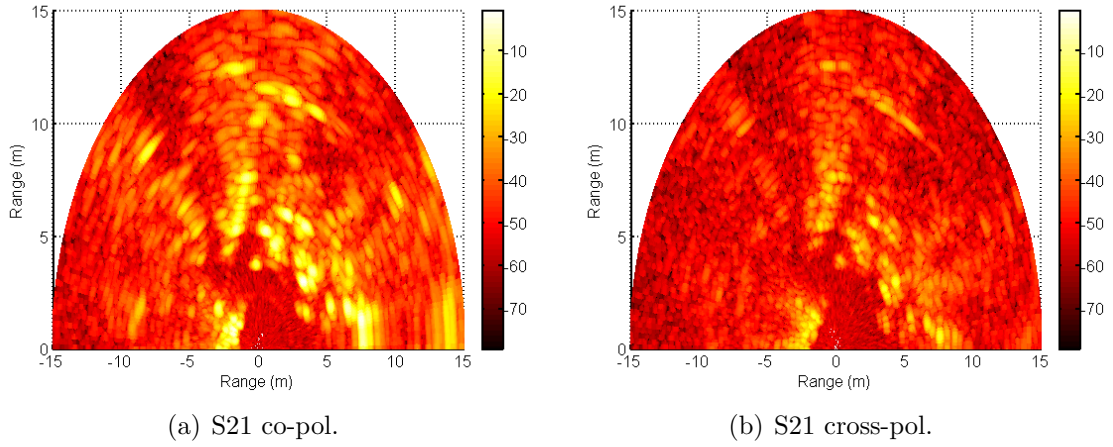


Figure 6.26: Scanned co-polarized and cross-polarized S21 measurements of the active retro-reflective array in a highly cluttered laboratory scene shown in Figure 6.25.

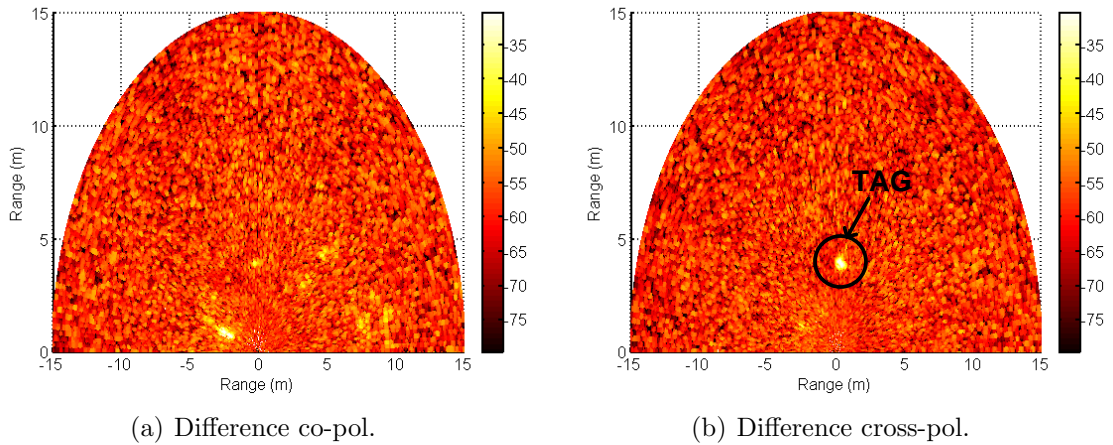


Figure 6.27: Scanned difference measurement for the co-polarized and cross-polarized arrangement of transmitting and receiving antennas of the active retro-reflective array in a highly cluttered laboratory scene shown in Figure 6.25.

6.5 Conclusions

This chapter describes the development of a unique cross-polarized architecture that both improves the performance and reduces the size of the retro-reflective array by exploiting polarization properties. The theory of operation is introduced along with the design of a dual-polarized linear series array. Operation of a novel high-RCS cross-polarized retro-reflective tag comprised of four 6X1 element dual-polarized GCPW patch arrays for operation at 26GHz is demonstrated. This passive array is able to achieve approximately -8dB of cross-pol RCS from a 8.5cm X 5cm structure. Additionally, in the cross-polarized configuration the response of the clutter is reduced by 20dB and detectability is maintained in this structure with a 70% reduction in the footprint of the array.

Amplifiers are integrated into the feed lines of this array without the need for circulators or other hybrid microwave components and shown to provide this tag with a unique non-reciprocal polarization signature. The overall system is verified in conjunction with a radar exhibiting polarization agility resulting in greater clutter rejection. The improved detection capabilities of this small retro-reflective tag in highly cluttered environments is thereby demonstrated.

CHAPTER VII

Conclusions and Future Work

7.1 Conclusions

In summary, this thesis presented novel architectures to enhance the discrimination of targets on metallic surfaces in highly cluttered environments. Chapter III begins with an introduction to a high-RCS alternative to the traditional passive Van Atta retro-reflector array topology for operation on metallic surfaces that uses GCPW linear series arrays to increase the gain and maintain the bandwidth. This structure additionally achieves a high RCS from a small planar structure. The design methodology is detailed along with the development of a numerical model to predict the overall retro-reflector behavior. Good agreement is shown between simulated and measured performance and a broad horizontal plane RCS is obtained for $\pm 30^\circ$ range of incidence angles and this structure is shown to achieve 0dBm from a 10cm X 15cm footprint.

Active modulation is added to this passive array in Chapter IV for the development of a new method for the detection and tracking of metallic objects at 26GHz. PIN diode switching elements in conjunction with a specially designed driver circuit provide each retro-reflective tag with its unique identification in the form of a clock frequency. The performance of the switching elements are confirmed by the RCS pattern comparison of the active tag in both its on and off states. Additionally, the

performance of the active array is demonstrated in a high clutter environment and the modulation shown to distinguish the response of the tag from that of the surrounding clutter.

This modulation is additionally used in conjunction with pulse-to-pulse subtraction and shown to further enhance distinction by removing the response of all time-stationary clutter. The operation of the active tag is validated along with the overall detection system, including background subtraction, using a mock application scenario constructed in the laboratory setting.

To improve the performance of the retro-reflective tag by broadening the elevation plane beam and reducing its overall size, the alternating-feed retro-reflector array is subsequently introduced in Chapter V. This novel architecture feeds the linear series arrays from both sides of the array, using the beam squint to broaden the incident elevation angle response. Operation of this structure along with vertical plane beam broadening is verified, but anomalies present in the horizontal plane pattern are undesirable for the intended application.

As a solution, the closed-loop feed architecture is introduced in the later section of Chapter V. For this architecture, the linear series array elements are simultaneously fed from both the top and bottom of the array. The performance of the overall array is enhanced by broadening the vertical plane beam without affecting the horizontal plane performance but the desired size reduction is no longer present for this array configuration. Measurements are collected for both beam broadening architectures and compared with those obtained from the Passive High-RCS Van Atta array presented in Chapter III and show a 300% broadening of the vertical plane beamwidths for these configurations corresponding to an increase of approximately 16° .

The cross-polarized architecture, introduced in Chapter VI, finally accomplishes this desired size reduction without sacrificing performance. This architecture uses polarization properties, namely the lower cross-polarized RCS of clutter at 26GHz,

to improve the performance and distinction of the tag without requiring a larger footprint. For this architecture, a linear series array is designed to operate in two orthogonal polarizations and the feed network implemented so that the signal is re-transmitted in the orthogonal polarization compared to the incident signal. This passive cross-polarized retro-reflective array is able to achieve approximately -15dB of cross-pol RCS from a 8.5cm X 5cm footprint. This polarization configuration additionally reduces the response of the clutter by 20dB.

Additionally, active non-reciprocal components in the form of amplifiers are integrated into the feed lines of this array and demonstrated to provide a unique non-reciprocal polarization signature. By subtracting two orthogonally polarized pulses, clutter rejection in excess of 50dB is achieved and overall system performance enhancements noted with a 70% reduction in size for the array. The overall system is verified and improved detection capabilities of this small retro-reflective tag in highly cluttered environments is demonstrated.

7.2 Future Work

While the future work of this thesis project involves the integration of tag and radar system, most notably for the active cross-polarized array, the future directions of the technologies enabled by the contributions of this thesis are vast. The main focus of the future work involves improved array performance and increased RCS.

7.2.1 Meta-material Line Integration

Negative refractive index materials are those who exhibit simultaneously negative permittivity and permeability [45]. These materials are also termed left-handed media (LHM) as the wave vector, k , forms a left handed triplet with the E and H -field vectors instead of the right handed triplet that is formed in conventional media. Waves propagating in these materials exhibit a reversed Doppler shift and refraction. This

property creates much interest in a wide variety of applications. Additionally, and more pertinent to the current application, these materials can be used for guiding structures as positive phase is gained in a LHM as they propagate away from the source [46].

By applying a LHM material in conjunction with the transmission lines already designed, the frequency dependence of the phase propagation of the transmission lines could be eliminated. This would thereby reduce or removing the variation of squint with respect to frequency for the linear series arrays and for the interconnecting feed network lines. This would alleviate the bandwidth limitations placed by the interconnecting feed network lines henceforth limit the overall size of the array in the horizontal plane. This could additionally allow for more freedom in the routing of these feed network lines.

To achieve this configuration, a meta-material is designed such that it exhibits the dual electromagnetic properties of the existing transmission line. In this configuration, the matching performance of the structure would be maintained, and only the unwanted phase propagation component altered. This structure is designed on the sub-wavelength scale and integrated into the existing feed lines as illustrated in Figure 7.1. The resulting structure would exhibit phase stability over its designed bandwidth.

The implementation of such a structure is straightforward when using a GCPW architecture as it does not require any additional vias. For the application of interest, the dual meta-material to the transmission lines of interest could be constructed using series capacitor and shunt inductor elements. A sketch illustrating the implementation in the host transmission line is illustrated in Figure 7.2.

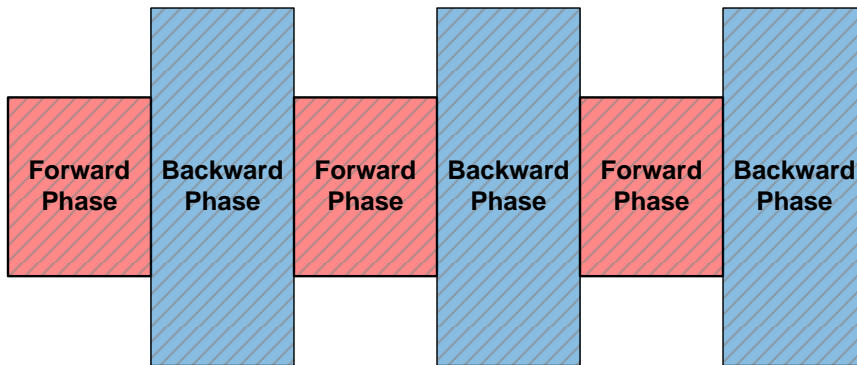


Figure 7.1: Alternating the standard transmission line with its dual removes the frequency dependence of the propagation delay of the wave along the transmission line.

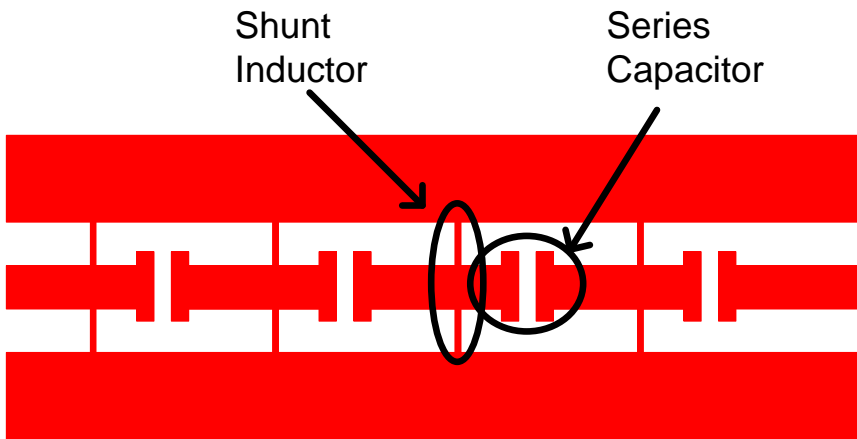


Figure 7.2: Alternating the standard transmission line with its dual removes the frequency dependence of the propagation delay of the wave along the transmission line.

7.2.2 Decrease Power Consumption

The active elements required for modulation of the array for both clutter distinction and unique identification all suffer from the drawback of consumption of power. Ideally, the minimization of this quantity is optimal. While for some RFID architectures, the active tags can collect the majority of their requisite power from the interrogating signal, this is a highly unlikely option considering the range of operation for this current application. Alternatively, the use of a 'wake up circuit' could be explored.

For the operation of this 'wake up circuit', the interrogating signal from the radar would be of sufficient power to trigger a wake-up process. The active elements in the array would be in the off positions until such time as the trigger is received, when modulation would begin. This architecture would save power as the arrays would no longer be required to operate continuously and likewise extend the life of their power source.

7.2.3 Alternate Retro-reflector Topologies

Additionally, advancements could be made regarding the two-dimensional Van Atta topology. This two-dimensional architecture would allow for the array to achieve retro-reflectivity in both the horizontal and vertical planes, which would prove useful for many applications. This requires the development of novel feed architectures potentially utilizing multi-layer board topologies. This would alleviate many of the drawbacks of this topology, including the increased line lengths and routing difficulties, previously discussed.

7.2.4 Alternative Substrate Materials

Decreasing the associated loss in the tag enhances performance by increasing the overall RCS of the structure. The aforementioned designs all suffer from high losses

due to the nature of metal at the frequency of operation. The use of alternative materials could be explored to mitigate these associated losses.

Additionally, the use of alternative materials in the design and manufacture of such retro-reflective arrays may prove enabling to a wide variety of future applications. For example, if the tags could be printed onto a thin adhesive surface, like a sticker, they would be able to conform to a wide variety of surface topologies in a very unobtrusive manner.

7.2.5 Advanced Applications

Perhaps the most interesting area of future work for these retro-reflective arrays lies in finding their most desirable applications. The designs presented in this thesis are highly adaptable with regard to size and frequency of operation. RCS coding techniques could be further developed to provide classification for an even larger number of targets. The low cost and robust nature of these arrays could further enable identification and tracking for a large number of alternative application scenarios.

BIBLIOGRAPHY

BIBLIOGRAPHY

- [1] Filko B.J. Greene, N.R. Animal-eyeball vs. road-sign retroreflectors. *Ophthalmic and Physiological Optics*, 30(1):76–84, 2010. cited By (since 1996) 0.
- [2] Robert B. Nilsen and Xai Jing Lu. Retroreflection technology. volume 5616, pages 47 – 60, London, United kingdom, 2004. Beam polarization;Counter reflection;Crime fighting;Retroreflection;.
- [3] C. Pon. Retrodirective array using the heterodyne technique. *Antennas and Propagation, IEEE Transactions on*, 12(2):176 – 180, Mar 1964.
- [4] Chee Binn Soo Buchanan N. Fusco, V. Analysis and characterization of pll-based retrodirective array. *Microwave Theory and Techniques, IEEE Transactions on*, 53(2):730 –738, Feb. 2005.
- [5] E. Sharp and M. Diab. Van atta reflector array. *Antennas and Propagation, IRE Transactions on*, 8(4):436–438, July 1960.
- [6] Shi Xiao-Wei Guo Yu-Chun Chen, Lei. Retrodirective array technology. *Progress In Electromagnetics Research B*, 5:153–167, 2008.
- [7] Wen-Jen Tseng, Shyh-Bong Chung, and Kai Chang. A planar van atta array reflector with retrodirectivity in both e-plane and h-plane. *Antennas and Propagation, IEEE Transactions on*, 48(2):173–175, Feb 2000.
- [8] M. I. Skolnik. *Radar handbook*. McGraw-Hill, New York, NY, 2nd edition, 1970.
- [9] L.C. Van Atta. Electromagnetic Reflector. U.S. Patent 2,908,002, Oct. 6 1963.
- [10] J. Appel-Hansen. A van atta reflector consisting of half-wave dipoles. *Antennas and Propagation, IEEE Transactions on*, 14(6):694–700, Nov 1966.
- [11] E. Gruenberg and C. Johnson. Satellite communications relay system using a retrodirective space antenna. *Antennas and Propagation, IEEE Transactions on*, 12(2):215–223, Mar 1964.
- [12] M. Fujita. Development of a retrodirective parc for alos/palsar calibration. *Geoscience and Remote Sensing, IEEE Transactions on*, 41(10):2177–2186, Oct. 2003.

- [13] Yu-Jiun Ren and Kai Chang. A broadband van Atta retrodirective array for ka-band applications. In *Antennas and Propagation Society International Symposium, 2007 IEEE*, pages 1441–1444, June 2007.
- [14] Shyh-Jong Chung and Kai Chang. A retrodirective microstrip antenna array. *Antennas and Propagation, IEEE Transactions on*, 46(12):1802–1809, Dec 1998.
- [15] Tzung-Jir Hong and Shyh-Jong Chung. 24 GHz active retrodirective antenna array. *Electronics Letters*, 35(21):1785–1786, Oct 1999.
- [16] M.G. Christodoulou and D.P. Chrissoulidis. 2d van Atta retrodirective array using dual polarized two-port square microstrip patches. In *Antennas and Propagation, 2001. Eleventh International Conference on (IEE Conf. Publ. No. 480)*, volume 2, pages 814–816 vol.2, 2001.
- [17] The Nan Chang and Jut-Shuan Wu. Retro-directive array using two-port dual polarized elements. *Microwave and Optical Technology Letters*, 50(2):450 – 3, 2008/02/. two-port dual polarized element; linear polarized retro-directive array; circular polarized retro-directive array;.
- [18] Time variant scenarios. <http://www.awe-communications.com>. Accessed on 5/27/10.
- [19] L. Sakkila, A. Rivenq, F. Boukour, C. Tatkeu, Y. El Hillali, and J.-M. Rouvaen. Collision avoidance radar system using uwb waveforms signature for road applications. In *Intelligent Transport Systems Telecommunications, (ITST), 2009 9th International Conference on*, pages 223 –226, oct. 2009.
- [20] Darpa grand challenge. http://www.darpa.mil/grandchallenge05/grandchallengephotos/awardphotos/DSC_5090.jpg. Accessed on 11/17/10.
- [21] Jr. Wood, W.D. An open-cavity RCS enhancement device for airborne applications. In *Antennas and Propagation Society International Symposium, 1998. IEEE*, volume 4, pages 2190 –2193 vol.4, June 1998.
- [22] Remotely piloted vehicle. http://www.ccot-lifesupport.org/remotely_piloted_vehicle.htm. Accessed on 11/17/10.
- [23] Predator UAV. http://www.links999.net/robotics/robots/robots_introduction.html. Accessed on 11/17/10.
- [24] K. Sarabandi, L.E. Pierce, M.C. Dobson, F.T. Ulaby, J.M. Stiles, T.C. Chiu, R. De Roo, R. Hartikka, A. Zambetti, and A. Freeman. Polarimetric calibration of SIR-C using point and distributed targets. *Geoscience and Remote Sensing, IEEE Transactions on*, 33(4):858 –866, July 1995.
- [25] H. Stockman. Communication by means of reflected power. *Proceedings of the IRE*, 36(10):1196 – 1204, oct. 1948.

- [26] R. Bansal. Coming soon to a wal-mart near you. *Antennas and Propagation Magazine, IEEE*, 45(6):105 – 106, dec. 2003.
- [27] R.J. Mailloux. Antenna array architecture. *Proceedings of the IEEE*, 80(1):163 –172, jan 1992.
- [28] P.S. Hall and C.M. Hall. Coplanar corporate feed effects in microstrip patch array design. *Microwaves, Antennas and Propagation, IEE Proceedings H*, 135(3):180 – 186, jun 1988.
- [29] Rogers Corporation. Rt/duroid6002 high frequency laminates. <http://www.rogerscorp.com/documents/609/acm/RT-duroid-6002-laminate-data-sheet.aspx>.
- [30] David M. Pozar. *Microwave Engineering. 2nd ed.* Wiley, New York, USA, 1997 1998.
- [31] T.-S. Horng, S.-C. Wu, H.-Y. Yang, and N.G. Alexopoulos. A generalized method for distinguishing between radiation and surface-wave losses in microstrip discontinuities. *Microwave Theory and Techniques, IEEE Transactions on*, 38(12):1800 –1807, dec 1990.
- [32] N. Dib and A. Omar. Analysis of grounded coplanar waveguide fed patches and waveguides. In *Antennas and Propagation Society International Symposium, 1997. IEEE., 1997 Digest*, volume 4, pages 2530 –2533 vol.4, July 1997.
- [33] T. Metzler. Microstrip series arrays. *Antennas and Propagation, IEEE Transactions on*, 29(1):174–178, Jan 1981.
- [34] K. Li, C.H. Cheng, T. Matsui, and M. Izutsu. Coplanar patch antennas: principle, simulation and experiment. In *Antennas and Propagation Society International Symposium, 2001. IEEE*, volume 3, pages 402–405 vol.3, 2001.
- [35] C. A. Balanis. *Antenna theory: analysis and design*. J. Wiley, New York, NY, 2nd edition, 1982.
- [36] A.Yu. Butrym, O.V. Kazanskiy, and N.N. Kolchigin. Van Atta’s array consist of tapered slot antennas for wideband pulse signals. In *Antenna Theory and Techniques, 2005. 5th International Conference on*, pages 221–223, May 2005.
- [37] Shyh-Jong Chung, Ten-Chi Chou, and Yung-Nein Chin. A novel card-type transponder designed using retrodirective antenna array. In *Microwave Symposium Digest, 2001 IEEE MTT-S International*, volume 2, pages 1123–1126 vol.2, 2001.
- [38] D. Pozar. Radiation and scattering from a microstrip patch on a uniaxial substrate. *Antennas and Propagation, IEEE Transactions on*, 35(6):613–621, Jun 1987.

- [39] McEwan Technologies. *Model PER-26, 26GHz UWB Rangefinder Evaluation Prototype*.
- [40] Quinstar Technology Inc. Qla lens antenna datasheet. http://www.quinstar.com/qla_lens_antennas.html.
- [41] F. T. Ulaby. *Radar Polarimetry for Geoscience Applications*. Artech House, Norwood, MA, 1990.
- [42] Shun-Shi Zhong, Xue-Xia Yang, Shi-Chang Gao, and Jun-Hai Cui. Corner-fed microstrip antenna element and arrays for dual-polarization operation. *Antennas and Propagation, IEEE Transactions on*, 50(10):1473–1480, Oct 2002.
- [43] K.V.S. Rao and P. Bhartia. Studies on input impedance and coupling of a dual polarized two port microstrip antenna. In *Antennas and Propagation Society International Symposium, 1989. AP-S. Digest*, pages 608–611 vol.2, Jun 1989.
- [44] Silicon Radar. Lna 024 03 datasheet. http://www.siliconradar.com/datasheets/Datenblatt_LNA_024_03.pdf.
- [45] V. G. Veselago. The electrodynamics of substances with simultaneously negative values of μ and ϵ . *Sov. Phys. Usp.*, 10:509–514, Oct 1968.
- [46] A. Grbic and G.V. Eleftheriades. A backward-wave antenna based on negative refractive index l-c networks. In *Antennas and Propagation Society International Symposium, 2002. IEEE*, volume 4, pages 340–343 vol.4, 2002.